

POLITECNICO DI TORINO

Master's Degree in BIOMEDICAL ENGINEERING



Master's Degree Thesis

Experimental study of laser application in medical oncology

Development and optimization of a thermal model for liver ablation
and analysis of optical fibre sensors in temperature monitoring

Supervisors

Prof. Guido PERRONE

Prof. Alberto VALLAN

Prof. Gianni COPPA

Candidate

Antonietta SAGGESE

Academic Year 2020/2021

To my father and to my mother,
the lighthouse that will illuminate my nights forever.

Summary

Thanks to advances in cancer prevention, early detection, treatment, and support for those facing the disease, more people than ever before have reason to hope.

Gary Reedy, CEO of American Cancer Society,
in "The Cancer Atlas", 2019.

Laser thermal ablation is one of the most common minimally-invasive tumour ablation techniques, along with RadioFrequency ablation, Microwave ablation, and Cryoablation. It is practised when a traditional surgical treatment of cancer would be too invasive, or when it would be too risky to access some tumour regions, as it often happens for liver cancers.

Laser ablation exploits the heating of the tissue to induce coagulative necrosis of the molecules and destroy the tumoral cells "in-situ". The response of the tissue strongly depends on the temperatures reached during the treatment. These temperatures must be monitored in real-time to have a feedback-based adjustment of the procedure.

Optical sensing fibres are the preferential method for non-invasive temperature monitoring; indeed, as they are non-conductive, it is feasible to handle these fibres under Magnetic Resonance without the risk of experiencing the artifacts that could arise from a high thermal conductivity. In particular, in this work of thesis, Fibre Bragg Gratings (FBGs) have been used as multi-point measurement sensors to detect the temperature in different positions simultaneously. The FBGs working principle is based on the reflection of a single wavelength occurring when an incident light goes across the gratings; this "*Bragg wavelength*" undergoes a shift when a temperature or strain perturbation occurs.

MicronOptics interrogator for optical fibres together with Matlab® computing environment have been used to characterize the sensors and derive temperature measurements during ex-vivo bovine liver ablation. As stated, the shift of the Bragg wavelength can also be induced by a mechanical stress; experiments have therefore been performed on FBGs sensors to evaluate the influence of the strain. In addition to the evaluation of temperature rises during laser ablation through experimental tests, a thermal model has been developed to predict the temperatures

reached by the tissue in order to help and find feed-forward adjustments of the ablation therapy. The model uses the Partial Differential Equation Toolbox in Matlab® to solve the differential equations of heat diffusion matters using the Finite Elements Method. The 2D-geometry of a cylinder section has been modelled, where the delivery probe connected to the laser is considered to be on the rotation axis of the cylinder; boundary conditions have been imposed in compliance with the experimental conditions. The model described above helps with predicting the temperatures in specific nodes of the geometry that can be compared with the measured values in the corresponding geometric positions.

An optimization code has finally been implemented to minimize the error between predicted and measured temperatures and to evaluate the optimal values for both thermal and optical parameters of the tissue such as thermal conductivity, absorption coefficient and scattering coefficient.

Acknowledgements

My sincere thankfulness goes to the supervisors of my thesis, Prof. Guido Perrone, Prof. Gianni Coppa, and Prof. Alberto Vallan for their kind support and helpfulness. Thanks to Aurora for her sweet willingness to help and encourage me in this project and to Alessandra, my thesis mate, for having shared with me this journey.

A heartfelt thanks goes to all my lifelong friends and to the newest but sincere ones for being a constant presence of love and sustain in my life. Thanks to all those who gave me honest affection and positivity.

A special thanks goes to Michela, for being the best friend I could desire and for making me feel at home everywhere. Thank you to Piero, Rita, Gregorio and all the friends in San Gregorio and surroundings for being present in my life.

Sincerely thanks to Roberta, for the constant laugh and for sharing with me the greatest joys and the difficult times during the last years; to Daniela, for her infectious positivity and her "brotherly" love; to Chiara, for being always on my side affectionately and to Benny, for her sweet sense of protection.

I want to thank Edo, as I promised him 5 years ago, for his Physics I notes but not only: for the patience, sweetness and affection he has been giving me for years.

My immense gratitude goes to all my family, for never making me feel alone despite the miles that have separated us and the difficulties of the last years.

Thank you to my grandparents Maria, Ciccio, Antonia and Gregorio for being part of the best memories of my childhood and for their unlimited love. Thanks to aunt Rosa and uncle Antonello for being like "second parents" for me and thanks to uncle Vito and aunt Mariella for the best gift they could give me: my little cousins Antonella and Giusy, the sweetest love in my life.

Thank you to my cousins Maria Adriana and Alessia, the sisters I've never had, for being my safe haven since I was born. A huge thanks to Gregorio, my "odi et amo" brother, for his pure love and his ability to make me laugh even when he makes me terribly angry.

My eternal gratitude and inspiration goes to my mother and to my father, for the uncountable sacrifices made to allow me to pursue my dreams and for their unconditional love. Thank you for having taught me love, courage and strength despite everything, I couldn't have wished for better parents.

Table of Contents

List of Tables	x
List of Figures	XI
Acronyms	XV
1 Introduction	1
2 Minimally invasive thermal ablation treatments	4
2.1 Cryoablation	5
2.2 Radiofrequency Ablation	5
2.3 Microwave Ablation	7
2.4 Laser Ablation	7
3 Laser for Biomedical Applications and Optical Fibres	9
3.1 Introduction to Lasers	9
3.1.1 General Laser Principles	9
3.1.2 Diode Lasers	10
3.2 Introduction to Optical Fibres	12
3.2.1 Bragg Grating Sensors	14
3.2.2 Optical Interrogators	18
3.3 Interaction with tissue	20
3.3.1 Absorption	22
3.3.2 Scattering	23
4 Thermal model	26
4.1 Principles of Finite Element Method	27
4.1.1 FEM in Heat Conduction Problem	27
4.2 Partial Differential Equation Toolbox	29
4.2.1 Heat Distribution in Circular Cylindrical Rod	30
4.3 Thermal Model for Laser Ablation	30

4.3.1	Geometry Description and Properties Definition	30
4.3.2	Results and Conclusions	36
5	Experimental Activities	40
5.1	FBGs Characterization	40
5.1.1	Set-up and Instrumentation	41
5.1.2	Results and Conclusions	45
5.2	Self-Heating Evaluation	51
5.2.1	Set-up and Measurements	51
5.2.2	Results and Conclusions	53
5.3	Ex-vivo experiments on bovine liver	55
5.3.1	Set-up and Measurements	56
5.3.2	Results and Conclusions	61
6	Thermal Model Parameters Optimization	69
6.1	Methods and Implementation	69
6.2	Results and Conclusions	70
7	Conclusions	74
A	Matlab codes	76
A.1	Thermal Model Code	76
A.2	FBGs Characterization Code	78
	Bibliography	86

List of Tables

4.1	Effects of temperature on biological tissues [27].	26
5.1	λ_0 and k_T values for each FBG. Straight.	45
5.2	λ_0 and k_T values for each FBG. HD	46
5.3	Maximum temperature variation during the descending thermal gradient and maximum relative temperature error for each FBG. Straight	50
5.4	Maximum temperature variation during the descending thermal gradient and maximum relative temperature error for each FBG. HD	50
5.5	Organization of the tests performed to evaluate the self-heating effect.	51
5.6	Maximum temperature deviation for the FBGs in air during self-heating evaluation.	54
5.7	Maximum temperature deviation for the FBGs in water during self-heating evaluation	55
5.8	Correspondence between current and power for the laser diode used.	58
5.9	Organization of the ex-vivo liver ablation experiments performed. .	59
5.10	Maximum temperature measured with the arrays during the tests at each power value.	63
6.1	Temperature deviations after the optimization at 0.5 W.	70
6.2	Temperature deviations after the optimization at 1 W.	71
6.3	Temperature deviations after the optimization at 1.5 W. The optimization at 1.5 W is the one that corresponds to the highest temperature deviation: 5.85 °C.	71
6.4	Temperature deviations after the optimization at 2 W.	72
6.5	Values of the parameters optimized.	73

List of Figures

1.1	"Statistics of the expected tumor death in 2021 (USA)." [2]	1
1.2	"Statistics of the incidence of cancers by the type [1]".	2
1.3	"Bar Chart of Region-Specific Incidence Age-Standardized Rates by Sex for Cancers of the Liver in 2018." GLOBOCAN 2018. [4]	3
2.1	An MR imaging-compatible cryoprobe for percutaneous use [5].	5
2.2	(a) Unipolar and (b) bipolar examples of RFA [6].	6
2.3	Algorithm of choice for thermo-ablation of a single nodule [12].	8
3.1	Laser constituent parts.	10
3.2	Illustration of the simplified structure of a laser diode [14].	11
3.3	Illustration of the structure of an optical fibre [15].	12
3.4	Schematic representation of light propagation in optical fibres using a ray picture. When the incident ray angle is smaller than θ_c the ray is reflected back into the core, otherwise it is transmitted into the cladding and it becomes practically negligible after some reflections.	13
3.5	Sketch of multimode fiber and single mode fibre [16].	14
3.6	Representation of the working principle of an FBG. Incident, transmitted and reflected spectra [18].	15
3.7	Representation of the shift of the Bragg wavelength due to thermal (upper figure) or mechanical (lower figure) stresses.	16
3.8	FBG structures and corresponding measured parameters and spectral responses [17].	17
3.9	Tunable laser source interrogator: working principle [20].	19
3.10	Micron Optics HYPERION si155 [21].	20
3.11	Peak detection method steps [22].	21
3.12	Absorption spectrum of water and other substances of interest at different wavelengths [24].	23
3.13	Schematic representation of the differences between Rayleigh and Mie scattering [25].	24

3.14	Graphical view of the deflection angle θ and of the forward direction retained after a single scattering event $\langle \cos\theta \rangle$ [26].	25
4.1	Boundary conditions representation in heat conduction problem [28].	28
4.2	Illustration of the problem geometry obtained using a PDE Toolbox in Matlab.	31
4.3	Representation of the mesh with its zoomed view, obtained using a PDE Toolbox in Matlab.	31
4.4	Representation of the gaussian laser beam on a 2D-surface	32
4.5	Representation of the rectangular laser beam on a 2D-surface	33
4.6	Power density distributions for the gaussian model. 2 W	35
4.7	Power density distributions for the rectangular model. 2 W	35
4.8	Comparison of the results for both gaussian and rectangular model at 0.5 W.	36
4.9	Comparison of the results for both gaussian and rectangular model at 1 W.	37
4.10	Comparison of the results for both gaussian and rectangular model at 1.5 W.	38
4.11	Comparison of the results for both gaussian and rectangular model at 2 W.	39
5.1	Structure of HighDensity-FBGs array and Straight-FBGs array. . .	41
5.2	J-type thermocouple (NI) software interface.	42
5.3	MicronOptics interface for the 20 reflection peaks of the FBGs. Straight.	43
5.4	MicronOptics interface for the 20 reflection peaks of the FBGs. HD.	43
5.5	Setup for FBGs-arrays characterization.	44
5.6	Calibration line: in blue the interpolating line is presented, in magenta the recorded data. Straight array.	46
5.7	Zoom of the calibration line: the point recorded overpass the interpolating line. Straight array.	47
5.8	Calibration line: in blue the interpolating line is presented, in magenta the recorded data. Ultradense array.	47
5.9	Zoom of the calibration line: the point recorded overpass the interpolating line. Ultradense array.	48
5.10	Comparison curve between the Straight-array and the thermocouple temperatures.	49
5.11	Comparison curve between the HighDensity-array and the thermocouple temperatures.	49
5.12	Setup for experimental self-heating evaluation in air.	52
5.13	Illustration of laser device including Lumics laser diode [27]	53

5.14	Illustration of laser device used for the experiments on the liver [31].	56
5.15	Illustration of the screen settings procedure steps to activate the laser used for the ex-vivo experiments on the bovine liver. The pictures in the figure are obtained from the device in Fig. 5.14. . . .	57
5.16	Setup for the ex-vivo bovine liver experiments.	60
5.17	Temperatures reached during the experiments for the array 1. . . .	62
5.18	Temperatures reached during the experiments for the array 2. . . .	63
5.19	Temperatures reached during the experiments for the array 3. . . .	64
5.20	Visible effects of the laser ablation on the bovine liver.	65
5.21	Graphics of the temperatures reached during the experiments in different instants of time by the positions of the FBGs. Array 1. . .	66
5.22	Graphics of the temperatures reached during the experiments in different instants of time by the positions of the FBGs. Array 2. . .	67
5.23	Graphics of the temperatures reached during the experiments in different instants of time by the positions of the FBGs. Array 3. . .	68
6.1	Graphical representation of the comparison between the measured temperatures and the temperatures evaluated with the optimized model. 0.5 W.	70
6.2	Graphical representation of the comparison between the measured temperatures and the temperatures evaluated with the optimized model. 1 W.	71
6.3	Graphical representation of the comparison between the measured temperatures and the temperatures evaluated with the optimized model. 1.5 W.	72
6.4	Graphical representation of the comparison between the measured temperatures and the temperatures evaluated with the optimized model. 2 W.	72

Acronyms

CT

Computed Tomography

CW

Continuous Wave

FBG

Fiber Bragg Grating

FEM

Finite Element Method

HCC

HepatoCellular Carcinoma

HDI

Human Development Index

LM

Liver Metastasis

LTA

Laser Thermal Ablation

MR

Magnetic Resonance

MWA

MicroWave Ablation

PDE

Partial Differential Equation

PW

Pulsed Wave

RFA

RadioFrequency Ablation

SNR

Signal-Noise Ratio

US

Ultrasounds

Chapter 1

Introduction

Over the years, medical innovations have brought significant improvements to the health conditions and life expectancy of people around the world. It is required that these innovations advance as the spread of diseases advances in order to prevent an increase in the mortality rate or, even better, to lower it. Obviously the mortality to diseases is closely related to the HDI (Human Development Index), an index of the development of the various countries that takes into account the life expectancy of the state.

Tumors are among the first 10 causes of death for almost all the countries in the world and the difficulties to treat them are related to many factors, such as the type of tumor, its stage, dimension or activity.

Gastrointestinal cancers, such as those of liver and pancreas, are currently estimated to be among the most common causes of death, despite being not so widespread [1, 2] (Fig. 1.1, 1.2): therefore, a particular effort is still required to improve their surgical and pharmacological treatment.

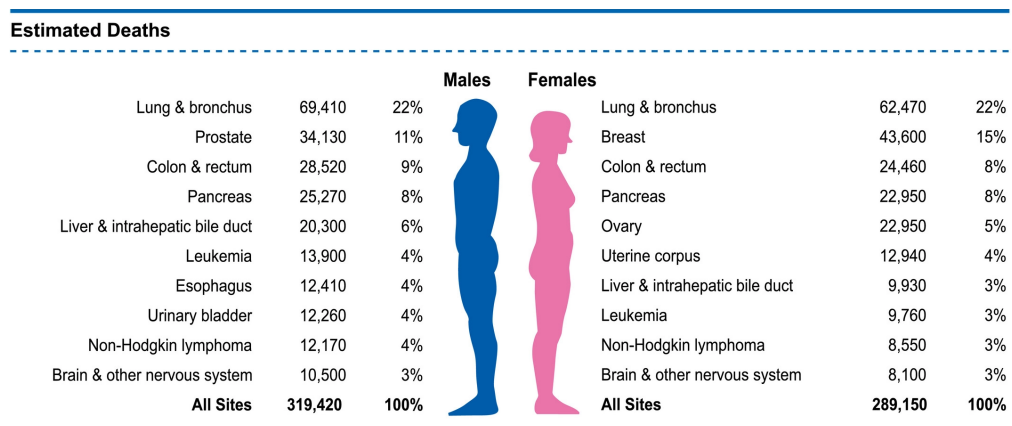


Figure 1.1: "Statistics of the expected tumor death in 2021 (USA)." [2]

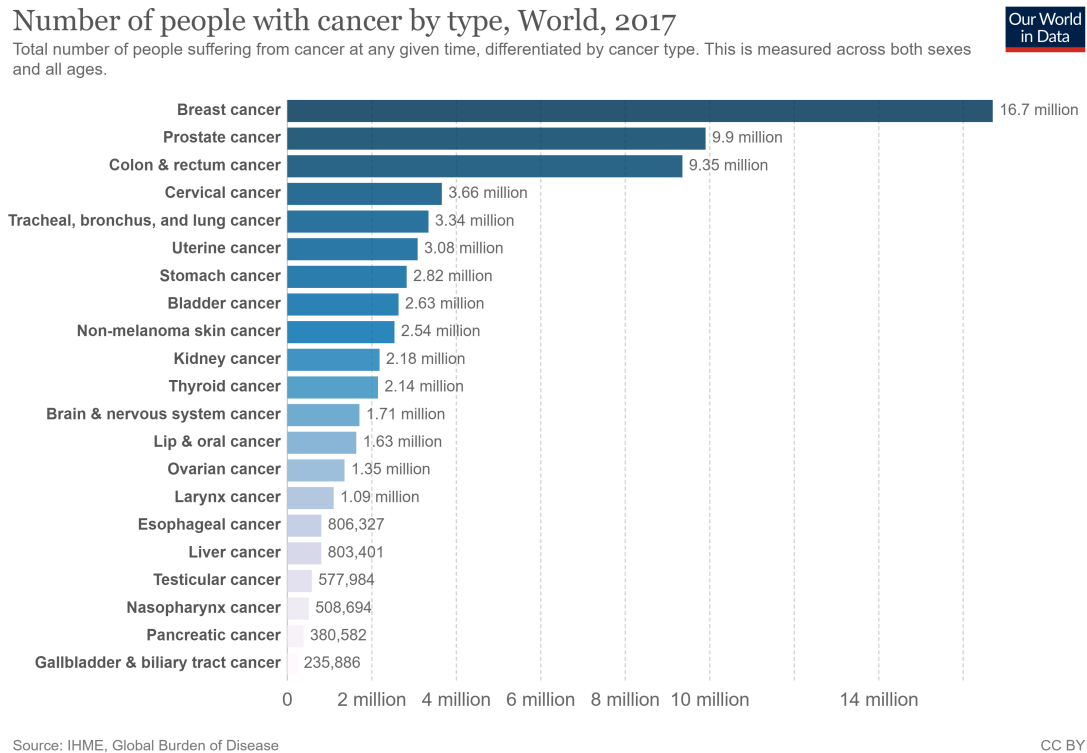


Figure 1.2: "Statistics of the incidence of cancers by the type [1]".

Hepatocellular carcinoma is the most diagnosed primary cancer of the liver and the eighth most frequently encountered type of solid neoplasm in the world. It can be caused by infections from hepatitis B or hepatitis C virus and some of its risk factors are highly dependent from the country HDI (Fig. 1.3). In addition to that it is not uncommon the development of liver metastases from other primary tumors that make the liver a very difficult target for traditional surgery [3].

In this thesis the laser ablation, one of the minimally invasive techniques for cancer treatment, is analysed. Experimental activities have been conducted together with the implementation of a numerical thermal model to simulate the treatment and predict the reached temperatures during the ablation. Optical fibres have been used both as delivery probes and both as temperature sensors, when inscribed with FBGs. Optical interrogators have been used during the tests to register and process data acquired from the sensors, that have been characterised before their usage to obtain the mathematical relationship between the temperatures and the wavelengths. Controlling the temperatures during the treatment is the critical goal of the laser ablation: usually the increasing of temperatures during the treatment leads to a dehydration of the tissues and a consequent growth of the light attenuation; this is a limitation from the therapeutic point of view resulting

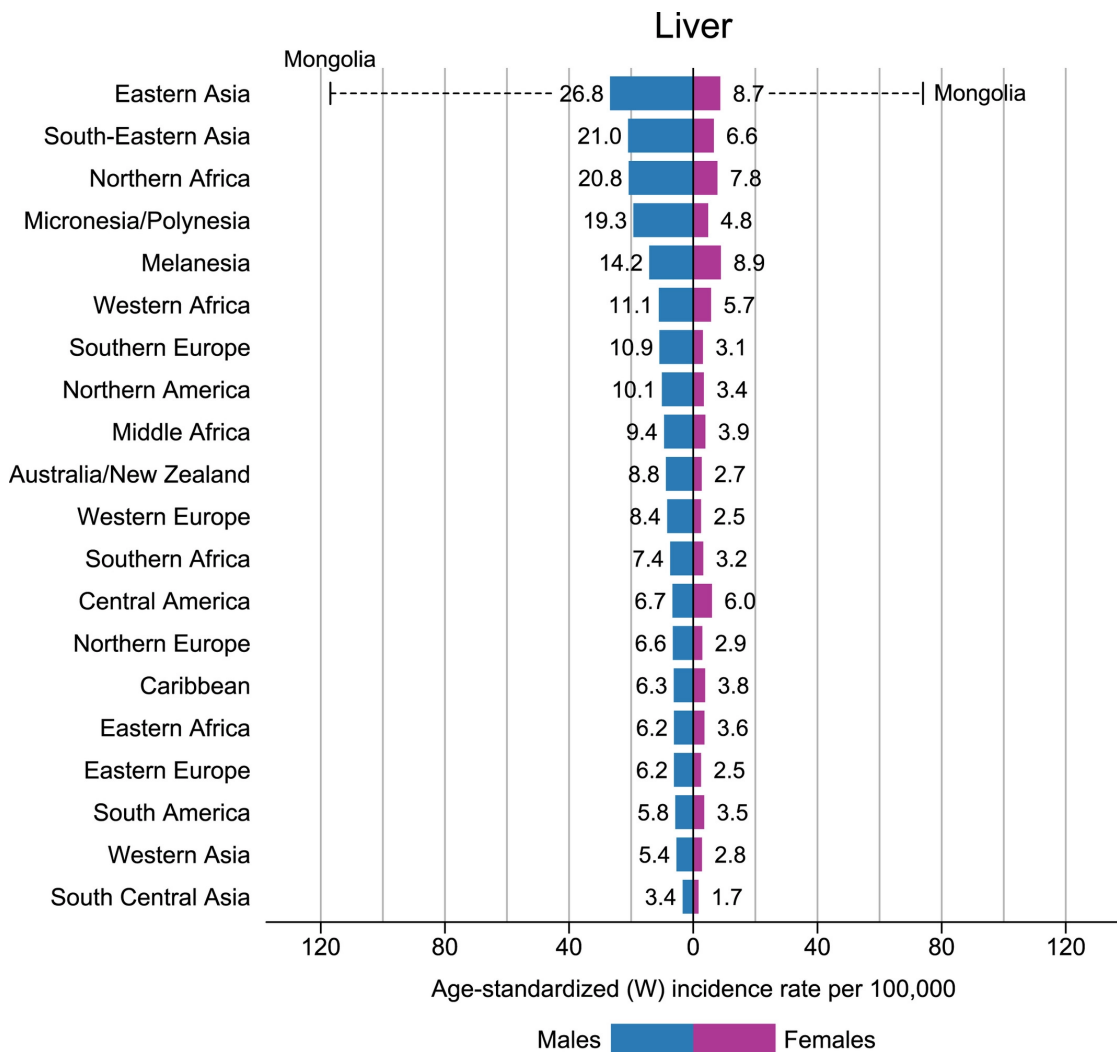


Figure 1.3: "Bar Chart of Region-Specific Incidence Age-Standardized Rates by Sex for Cancers of the Liver in 2018." GLOBOCAN 2018. [4]

in a shrinkage of the ablated area.

The aim of this thesis is to predict with a model what happens in the liver at different power values starting from experimental measures. Consequently the parameters of the treatment such as optical power and duration time can be adjusted depending on the expected effects. However the measurements made are affected by errors and some simplifications have been done, as it will be explained in the next chapters.

Chapter 2

Minimally invasive thermal ablation treatments

Minimally invasive treatments are increasingly emerging alongside intervention techniques during the last decades, indeed the benefits of traditional surgery do not outweigh the resulting risks for many cancer patients [5]. Among the disadvantages of surgery it is possible to mention the risks related to general anesthesia, the long recovery time usually required, the higher cost and morbidity and the limitations related to patients who cannot be surgical candidates [5, 6].

By minimally-invasive techniques it is common to refer to intervention methods aimed to minimize the trauma associated with traditional surgery. Specific applicators are inserted in the involved district supported by imaging techniques in order to guarantee a precise control of the positioning of the applicators through a guiding needle insertion. Some of the most used image techniques include Magnetic Resonance (MR), Computed Tomography (CT), Ultrasounds (US).

Thermal ablation is a minimally invasive treatment referred to the necrosis of tissue by extremely high tissue temperatures (hyperthermia) or extremely low tissue temperatures (hypothermia). The tissue is not removed but it is absorbed in situ.

Despite the fact that surgery still represents the first choice among the medical interventions, there are some cases in which thermal ablation is the only solution to clinical challenges. For example, about 80% of liver tumor patients are not good candidates for surgery because of lack of liver function reserve, risk of out of control bleeding or insufficiency of baseline health [7]. In addition to that, radiation therapy and chemotherapy are not recommendable for liver cancers and most of the times liver represents a challenging position to surgically intervene; these are the main reasons that lead the liver to be the most common site for thermal ablation [8]. The choice of the ablation technique usually depends on the physicians' preference

and experience. Among the most used there are:

- Cryoablation [3, 5, 8]
- Radiofrequency Ablation [5, 6, 9]
- Microwave Ablation [5, 10]
- Laser Ablation [5, 6, 11, 12]

2.1 Cryoablation

Cryoablation is a thermal therapy in which very low temperatures are achieved in order to cool the tumor; the death of the tumor cells is not directly related to the low temperatures but rather to the ice crystal formation during rapid freezing. Indeed needle-like applicators and cryoprobes are used to introduce low temperature gas or liquid into the tissue (Fig. 2.1). This leads to the denaturation of proteins and to the destruction of cellular membrane: usually cycles of freezing are alternated to cycles of thawing to induce higher mechanical stress and so to accelerate cell death [3, 5].

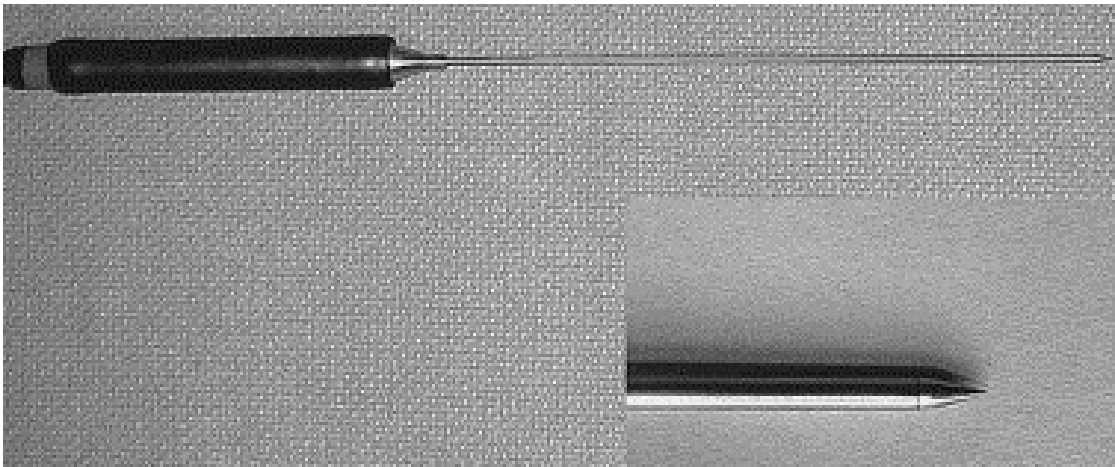


Figure 2.1: An MR imaging-compatible cryoprobe for percutaneous use [5].

2.2 Radiofrequency Ablation

Radiofrequency Ablation (RFA) is the most documented and used thermo-ablation technique so far.

The necrosis of the tissue is due to high temperatures reached during the process because of an alternating electric current in the radiofrequency range (460 kHz to 500 kHz) injected directly into the tumor mass. The frictional energy loss associated to this ionic current causes the heating of the tissue [9]. Using imaging techniques electrode needles are inserted into the tumor and a RF generator provides power to the tissue. The patient becomes part of a closed-loop circuit where the current flows between an active electrode and a dispersive electrode. The dispersive electrode is usually a large electrode positioned on the skin in an area of good electrical and thermal conductivity.

There are different kinds of active electrodes (Fig. 2.2) :

1. single electrode, where only one sharp electrode is located into the tumor so it is most used for very small tumor volumes (monopolar mode);
2. multielectrode, where more than one electrode is positioned into the tumor so higher volumes of ablated zones can be reached (multipolar mode).

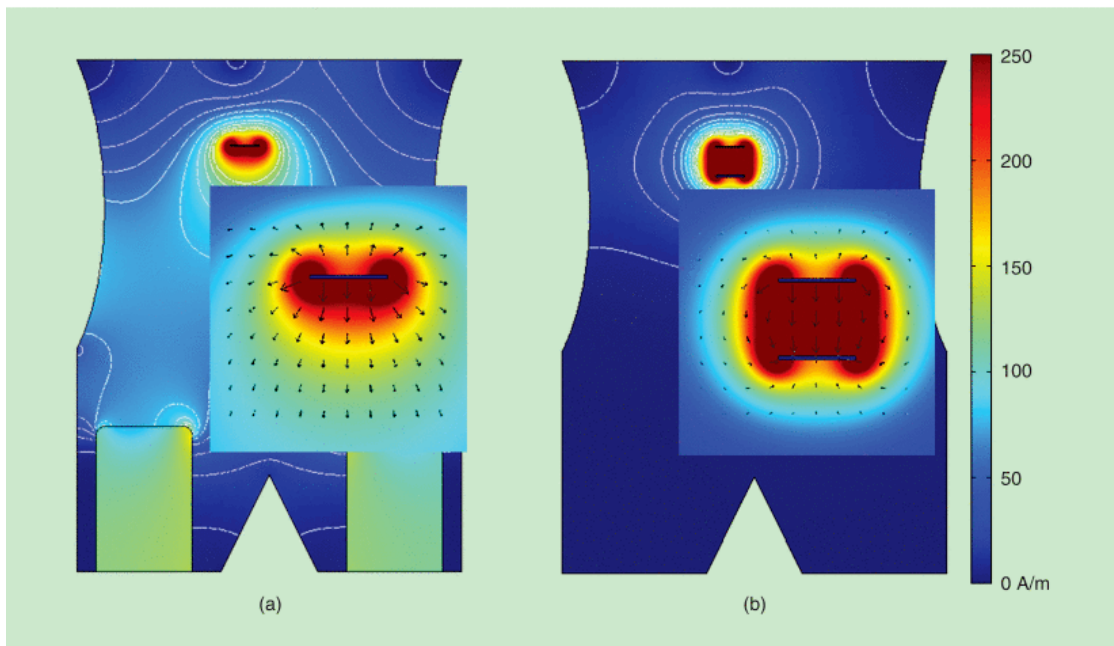


Figure 2.2: (a) Unipolar and (b) bipolar examples of RFA [6].

The greatest disadvantage of RFA is the fact that when the tissue is heated, its impedance increases in the area closer to the electrode and this leads to a difficulty in the propagation of the current in the surrounding tissue. This is one of the reasons for which in certain circumstances other techniques are preferred over RFA.

2.3 Microwave Ablation

Microwave ablation (MWA) induces an agitation of water molecules that leads to an increase in temperature and a consequent coagulation necrosis of cells. The molecules vibration is due to an alternating electric field induced by microwaves (frequencies from 900 MHz to 2,450 MHz [10]) emitted by a bipolar needle-like antenna.

The main issue related to antenna designs is to guarantee a radiation that responds to a compromise between efficiency and ablation geometry optimization [5].

MWA is nowadays less used than RFA but it has some advantages over RFA: microwave energy propagates also through the dehydrated tissue consequent to thermoablation so there is not a limitation related to the desiccated tissue in district such as lungs on bones.

2.4 Laser Ablation

Laser Therapy Ablation (LTA) is the thermal ablation technique studied most recently; the principle on which it is based is the absorption of light by the tissue, resulting in an increasing of temperature.

A low-intensity coherent laser beam is guided to transfer high-energy light to the tumor across optical fibres [5]. The heating of the tissue is a consequence of the interaction between light and matter: some particles are absorbed by the chromophores and some others are scattered. The greater is the absorption level, the higher is the increasing of temperature in a localised area, while if the absorption level is low the light propagates for higher distances, resulting in a larger area of heated tissue.

The fact that some particles are scattered is responsible for the deviation direction of the incident light, causing a greater heated area.

Usually for this kind of biomedical application wavelengths of around 1 μm are used to guarantee the desired absorption phenomenon.

LTA is nowadays used in applications such as ophthalmology or dermatology more than in tumors treatment but its effectiveness in this field has been demonstrated and it has also been shown to have several advantages over other methods [11]:

- feasibility, because very small needles are required to guide the fibres into the tumor, making LTA secure also for high-risk positioning;
- adaptability, as it is possible to include up to four fibers to obtain a larger ablated zone for tumors of maximum 4 cm to 5 cm in diameter;
- affordability, as it is the cheapest treatment when up to three fibres are needed.

Over the years, the study and deepening of different physical principles and the development of new applications of these principles has led, as described, to the emerging of different innovative methods for solid tumors treatment. All of them are non-invasive, highly tolerated and efficient: the choice of the best technique should take into account the nature, number, dimension and location of the nodules; in Fig. 2.3 it is reported an algorithm of ablation choice in case only a single nodule needs to be treated.

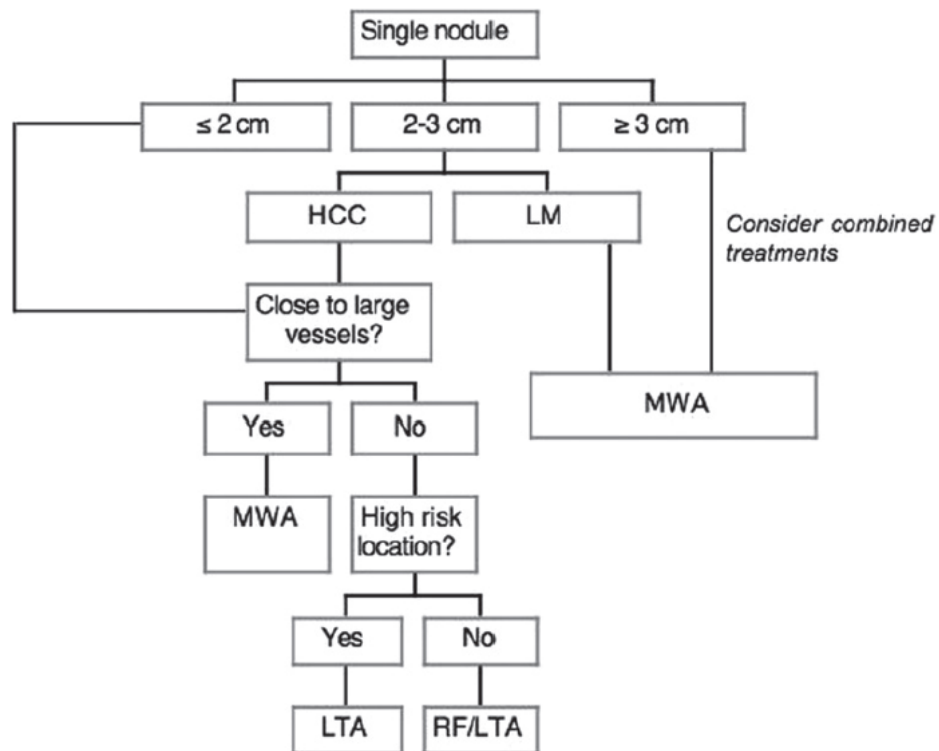


Figure 2.3: Algorithm of choice for thermo-ablation of a single nodule [12].

The laser ablation technique is the method that will be analysed in this work of thesis.

Chapter 3

Laser for Biomedical Applications and Optical Fibres

3.1 Introduction to Lasers

A laser is an optoelectronic device that emits a coherent beam of light, where the term “coherent” means that there is a fixed phase relationship between the electric field values at different locations or at different times and therefore the beam is capable of exhibiting interference effects; for the scopes of this thesis, it refers to a practically monochromatic beam. The word “Laser” is the acronym of Light Amplification by Stimulated Emission of Radiation, which evidences that the amplification of light is due to the stimulated photon emission, a phenomenon that occurs only when specific conditions are met as detailed in the following.

3.1.1 General Laser Principles

Physically, a laser device consists of three main parts, as sketched in Fig. 3.1:

- gain medium;
- pump source;
- resonator.

The gain medium is where the amplification through the stimulated emission takes place. For laser action it must be positioned inside an optical cavity – the resonator – formed by two mirrors, one totally reflective and the other partially reflective so

that a beam can be emitted from the resonator. The pump source is the mechanism that provides the energy for the amplification through the excitation of the gain medium atoms or molecules. Normally light is emitted because of the spontaneous

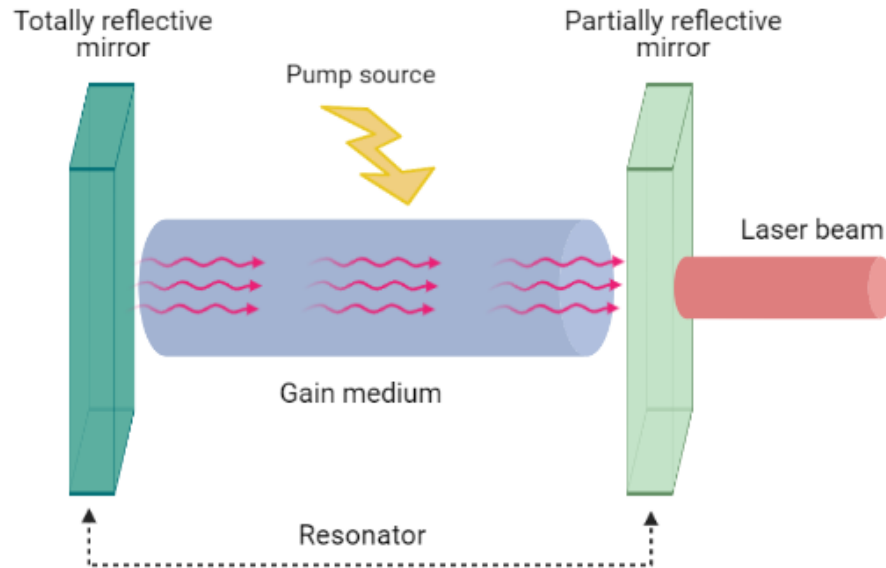


Figure 3.1: Laser constituent parts.

emission, a photon generation due to random decays of atoms or molecules from an excited state reached thanks to the pump action (it can be the absorption of pump photons or the injection of carriers) to the ground energy state. However, when a pump value known as the laser threshold is exceeded, the photon generation becomes predominantly due to the stimulated emission, in which a incident photon stimulates the decay of the atom or molecule with the consequent generation of another photon having the same characteristics as the incident one. This is an avalanche mechanism that is responsible for the generation of “identical” photons and therefore the emission of a coherent light beam.

3.1.2 Diode Lasers

A laser diode is an electrically pumped laser in which the gain is generated by an electrical current flowing through a junction made with differently doped semiconductor materials.

In general, a diode is a two terminals component formed by the junction of two

semiconductor regions, one of them doped with a material that causes an excess of negative charges (n-doped), while the other doped with a material that causes an excess of positive charges (p-doped). When the diode is connected to power in “reverse bias” (p-terminal connected to negative voltage V- and n-terminal connected to positive voltage V+), the charges in each region are attracted to the terminals and there is no interaction at the interface (depletion zone), so no current flows into the diode. Conversely, when connected in “forward bias” (n-terminal connected to negative voltage V- and p-terminal connected to positive voltage V+), the charges are repulsed from the terminals and there is interaction at the interface between the two materials so a current flows from p-region to n-region.

In a laser diode an extra compound layer called “intrinsic layer” in which the recombination takes place is positioned between the p-doped semiconductor and the n-doped semiconductor. The facets of the semiconductor are used as the cavity mirrors, although specific materials are deposited on their surfaces to increase the reflectivity on one side and reduce it at the opposite side to form the totally and partially reflective mirrors (Fig. 3.2) [13].

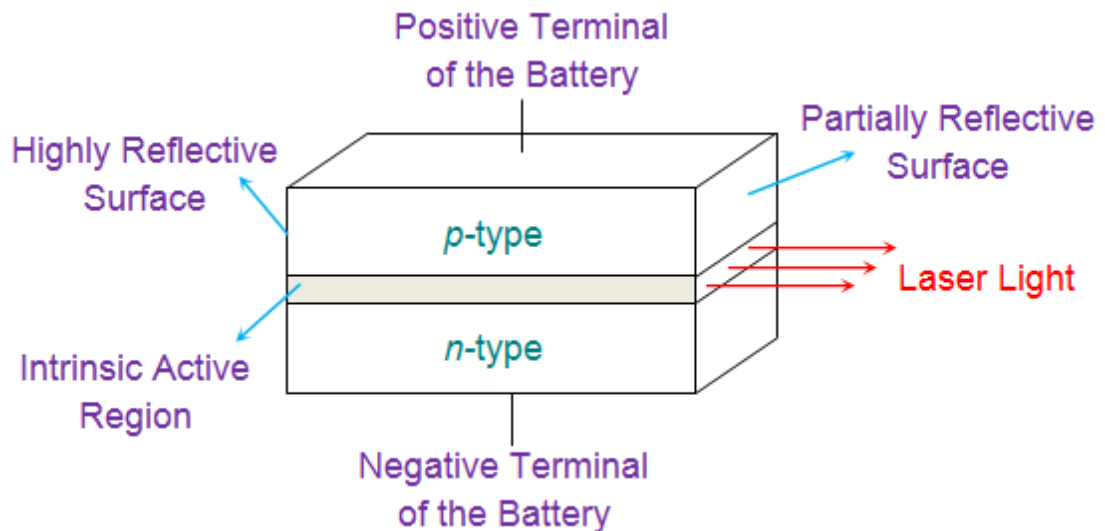


Figure 3.2: Illustration of the simplified structure of a laser diode [14].

Continuous wave (CW) and pulsed wave (PW)

A laser can operate in *continuous wave mode* (CW) or in *pulsed wave mode* (PW); in the first case the wave is emitted continuously, while in the latter case the laser is alternatively switched on and off with the possibility to change the pulse duration and the duty-cycle depending on the exploited pulse generation approach. In the tissue ablation applications with laser diodes, the pulsed operation is simply

obtained by pulsing the pump current, achieving pulses with sub-second duration and arbitrary duty-cycle.

A CW treatment guarantees higher ablated regions while a PW treatment is usually preferred for precise and limited ablated areas; this is because in CW high temperatures are rapidly reached and the vaporization of the water occurs, resulting in a large region ablation; in PW instead the heating is not fast and the heat is absorbed by the tissue during the OFF-time, resulting in smaller ablated regions. This thesis project focuses on the CW ablation, considering the variability of the reached temperatures when the emission conditions are varied.

3.2 Introduction to Optical Fibres

Optical fibres allow guiding the laser light beam to the ablation region. Their application range goes from telecommunications to medicine, to illuminating engineering. Among the advantages of optical fibres it is possible to highlight their immunity to electromagnetic interference, the extremely low propagation losses, and the reduced invasive impact thanks to a minimum footprint.

An optical fibre consists of a concentric structure in silica glass and/or plastic polymer (Fig. 3.3). The central region with a very small diameter is called the *core* and it is where the light confinement takes place; it is surrounded by the *cladding*. A buffer and a jacket are positioned around the core and cladding in a concentric configuration to guarantee support and resistance to mechanical stress and to prevent contact between the fiber and the external environment.

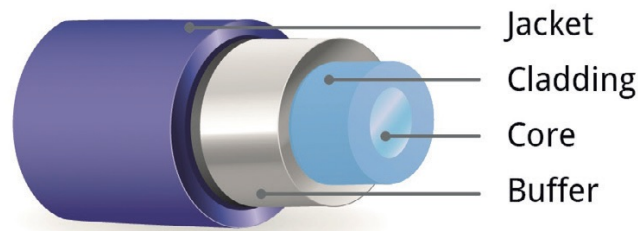


Figure 3.3: Illustration of the structure of an optical fibre [15].

The confinement in the core is obtained exploiting the total internal reflection at the core-cladding boundary and this requires that the core has a slightly larger refractive index than the cladding. In silica fibres this is obtained by doping the core with materials like Germanium that increase the refractive index.

It is possible to explain the guiding property of optical fibres with a ray picture in which guided rays propagate into the core in a series of zig-zag bounces, although this represents a good approximation only for large core fibres, the so-called

multimode fibres. According to the Snell's law, when a light beam meets a medium different from the one in which it was propagating, depending on the incident angle and on the refractive index of the two media, the ray splits in two ways:

- **refracted ray**, which is transmitted into the second medium although with a different direction;
- **reflected ray**, which does not transmit into the second medium but it is reflected back into the first medium with an angle equal to the incidence one.

If the refractive index of the incident medium is larger than that of second medium, for certain incident angles it is possible that the beam is totally reflected, the total internal reflection condition. In the case of an optical fibre, this occurs when the light radiation goes into the fibre with an incident angle θ_i smaller than the maximum *acceptance angle* (or critical angle) θ_c defined by a fibre parameter called the *Numerical Aperture* (NA), which indicates how much the acceptance angle is large and how much it is easy to couple a light source and a fibre. When instead θ_i is greater than θ_c , the ray is partially transmitted across the cladding and it is lost in the long run (Fig.3.4). Different bouncing angles correspond to different

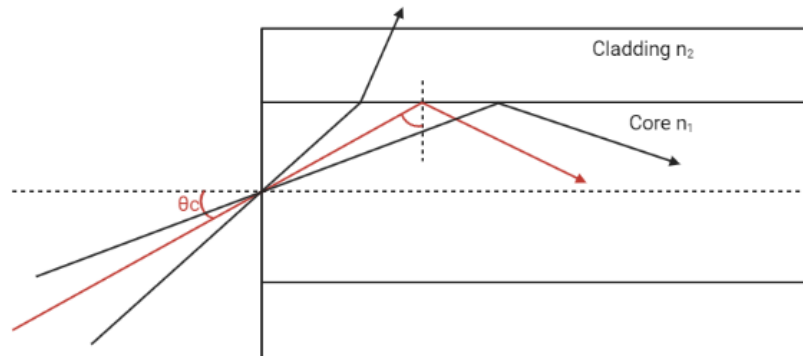


Figure 3.4: Schematic representation of light propagation in optical fibres using a ray picture. When the incident ray angle is smaller than θ_c the ray is reflected back into the core, otherwise it is transmitted into the cladding and it becomes practically negligible after some reflections.

field configurations inside the fibre called *modes*; in turn, their number depends on the core-cladding refractive index difference (which is, however, almost constant for all the practical fibres) and on the core diameter. It is therefore possible to distinguish between (Fig. 3.5):

- **single mode fiber**, characterized by smaller core diameters (usually smaller than $10\ \mu\text{m}$) and a single propagating field configuration or mode, which has a gaussian profile;
- **multimode fiber**, characterized by larger core diameters (usually larger than $50\ \mu\text{m}$, up to $1\ \text{mm}$) and many propagating field configurations or modes, which interfere giving an almost rectangular field distribution.

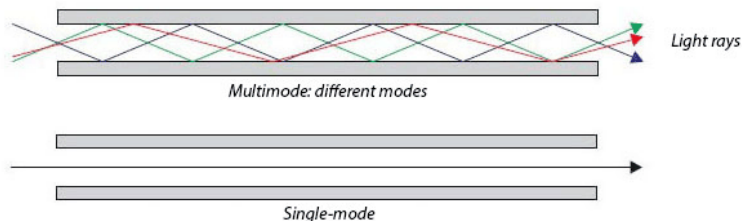


Figure 3.5: Sketch of multimode fiber and single mode fibre [16].

Both single mode and multimode fibres are used in this work of thesis in the experimental part, as it will be described in Chapter 5.

Even if it has been mentioned a “total internal reflection” during the propagation of the light beam, in fact there are some losses due to the interaction of light with the medium itself (intrinsic losses) that are related to the phenomena of absorption and scattering that will be described in detail in the next section speaking of the interaction between light and matter.

3.2.1 Bragg Grating Sensors

Fiber Bragg Gratings (FBGs) are periodic structures inscribed in the core of optical fibres made by a periodic variation of the refractive index permanently induced in a short segment of the fibre [17]. This structure results in a band pass filter behaviour because when an electromagnetic wave goes across an FBG, one specific wavelength is in phase with the period of the grating and will be reflected back, while all the other wavelengths are transmitted through the fibre (Fig. 3.6).

The reflected wavelength is called the *Bragg wavelength* and it is given by

$$\lambda_B = 2n_{\text{eff}} \Lambda \quad (3.1)$$

where n_{eff} is the effective refractive index of the core and Λ is the grating period. In practice, the spectrum reflected by the FBG presents a peak around the Bragg wavelength. This is exploited for sensing because λ_B shifts with temperature and strains applied to the fibre because they both modify the period of the grating and

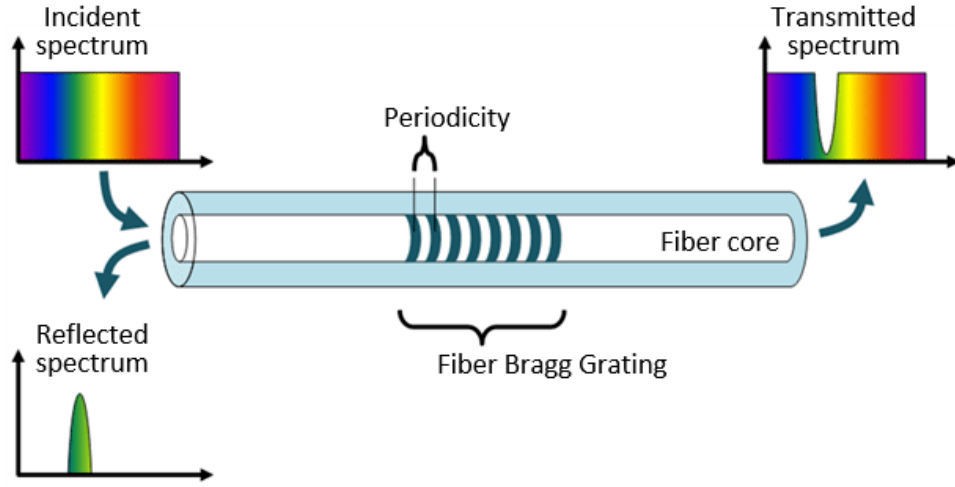


Figure 3.6: Representation of the working principle of an FBG. Incident, transmitted and reflected spectra [18].

the refractive index (Fig. 3.7).

It is demonstrated that the relation

$$\Delta\lambda_B = K_\varepsilon \cdot \varepsilon + K_T \cdot T \quad (3.2)$$

is the general expression to indicate the macroscopic dependence of Bragg wavelength variation from temperature and strain, where K_ε is the *strain sensitivity* (typically 1 pm/ μm for silica fibres) and K_T is the *temperature sensitivity* (typically 10 pm/ $^\circ\text{C}$ for silica fibres).

Grating structure

The structure of the FBGs is dependent on the different grating period chosen in the fabrication process. It is possible to distinguish between (Fig. 3.8):

- *Uniform*: the grating period is constant along the fibre; this is one of the structures used for the fibres involved in this work of thesis;
- *Chirped*: the grating period increases linearly along the fibre;

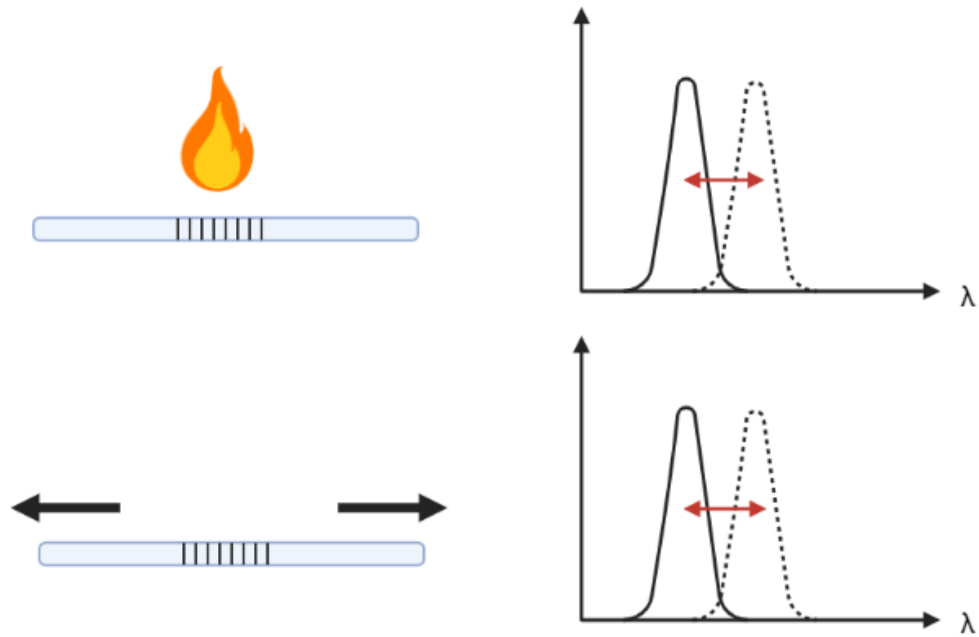


Figure 3.7: Representation of the shift of the Bragg wavelength due to thermal (upper figure) or mechanical (lower figure) stresses.

- *Tilted:* the section of the core to change refractive index is not a perpendicular section but an angled one but the grating period is constant;
- *Etched:* the section of the fiber containing the FBG undergoes a chemical reaction with chemical agents resulting in an etched portion;
- *Array:* an array of FBGs appears in the fibre core resulting in a series of Bragg wavelengths to measure physical quantities in different positions.

Fabrication methods

The characteristics of FBGs are strongly influenced also by the techniques used to create the refractive index variation in the core. The traditional fabrication method exploits the photosensitivity of the doped core to the ultraviolet light for which permanent changes in the refractive index are obtained by exposing it to an intense UV laser beam. More recently, alternative fabrication methods based on the exposure to extremely short pulses generated by a femto-second laser have been introduced. Different manufacturing methods are reported in the literature:

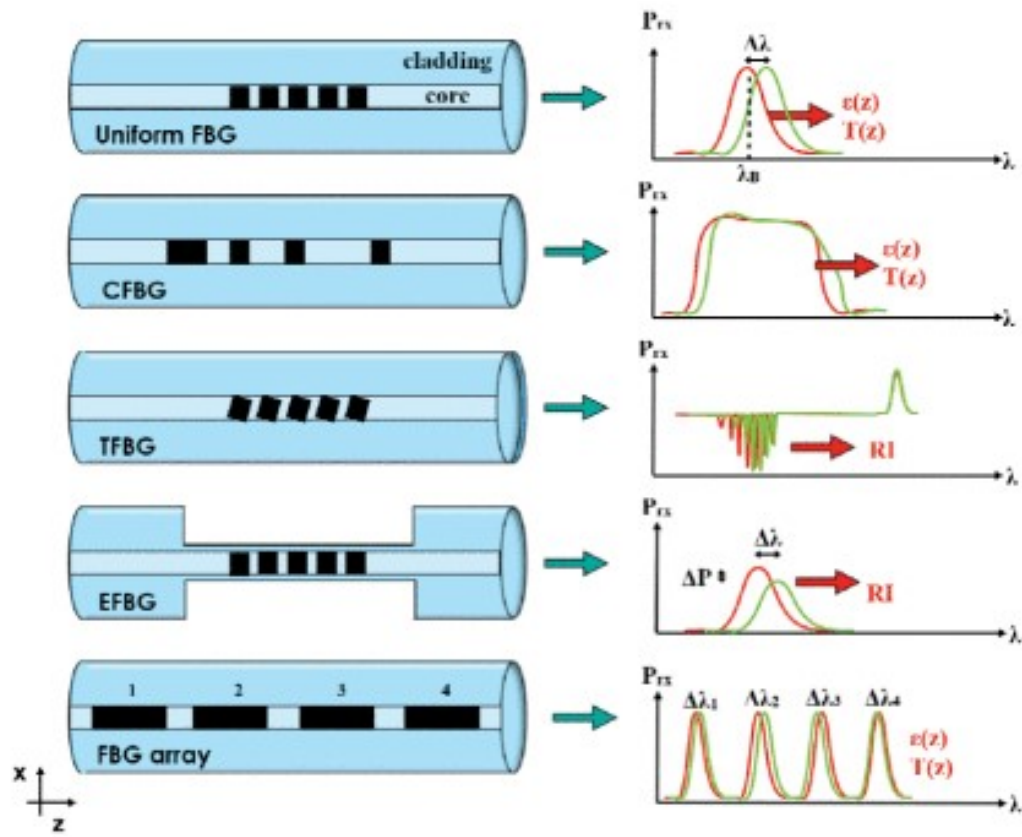


Figure 3.8: FBG structures and corresponding measured parameters and spectral responses [17].

- *Interference:* the writing laser beam is split into two beams that are made to interfere with each other generating a sinusoidal light pattern that, in turn, produces the periodic modulation of the core refractive index; this approach, which is typically implemented with CW UV lasers, is flexible because different λ_B can be obtained by changing the angle at which the beams interfere, but it requires a very good mechanical stability over the entire process duration.
- *Phase mask:* a phase mask characterized by the desired grating pattern is positioned between the light source and the fiber to generate the required periodic structure; this approach is less flexible because different λ_B require different phase masks, but it is less demanding from the mechanical setup point of view.
- *Point-by-point:* as the name implies, a focused laser beam is used to locally

modify the core refractive index “writing” directly the grating point by point; this approach is typically used with femto-second lasers and is the most flexible since it allows obtaining any λ_B by simply changing the period of the modification Λ .

The FBG sensors used for the experimental activity of this thesis have been fabricated using the point-by-point femto-second laser writing technique.

Advantages of FBGs temperature sensors

In this project of thesis the FBGs sensors are mainly used to detect temperature variations. The choice to use this kind of sensors instead of other electronic temperature sensors is due to the many advantages of these optical fiber sensors with respect to other techniques [19]:

- immunity to electromagnetic interference and absence of artifacts due to absorption of the laser light;
- impossibility to cause electrocution since no electrical power supply is required;
- reduced perturbation of the temperature measurement because of the low thermal conductivity of the silica/polymers and the reduced size;
- minimal invasive impact due to the small size of the fibre and the possibility to remote the interrogation exploiting the guidance properties of the fibres;
- resistance to corrosion;
- possibility to measure temperature profiles implementing a quasi-distributed sensing system by using FBG arrays.

3.2.2 Optical Interrogators

An optical interrogator is an acquisition system used to detect the Bragg wavelength in a single FBG or in arrays of FBGs. Different approaches have been proposed over the year, the most common being based on broadband light source and an optical spectrum analyser. More in detail, at least two types of interrogators can be described:

- **Broadband light source interrogator:** in this case the light from a broadband source (for example a super-luminescent LED, SLED) is routed to the FBG through an optical circulator that directs the reflected light to an optical spectrum analyser (or a tunable filter) to isolate the contribution of the different wavelengths in the spectrum;

- **Tunable laser source interrogator:** this interrogator differs from the previous one because there isn't any tunable filter at the receiver but instead a tunable narrowband source is used to explore the spectrum (Fig.3.9); this method guarantees a higher signal-noise ratio (SNR).

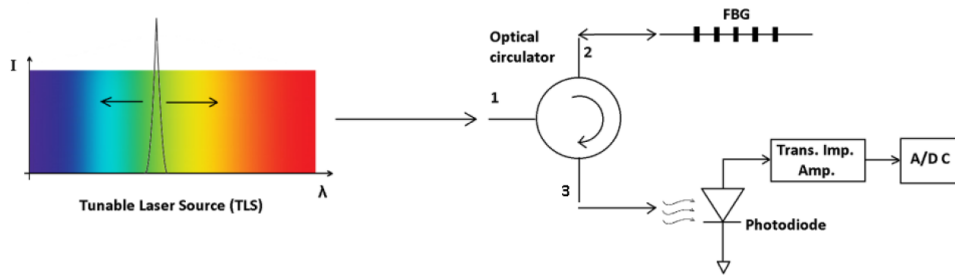


Figure 3.9: Tunable laser source interrogator: working principle [20].

Micron Optics HYPERION si155

Micron Optics HYPERION si155 by Luna Technologies is the interrogator used in this thesis for the peaks tracking and it belongs to the second class of interrogators described above.

Its technical specifications are:

- wavelength range: 1,500 nm to 1,600 nm;
- resolution: 10 pm;
- 4 parallel channels;
- maximum acquisition rate: 1 kHz.

The instrument (20.6 cm x 27 cm x 7.9 cm) can be remotely controlled through an Ethernet connection using the ENLIGHT Sensing Analysis Software, which is a graphical user interface that allows easily interacting with the instrument. The peaks of the spectrum can be shown simultaneously on the 4 parallel channels and for each channel any wavelength shift can be detected in real time.

It is possible to modify the settings of the instrument from the user interface with drop-down menus, where saving options, acquisition frequency, peaks registering rules can be modified. For example for each channel a different *rule* for the spectral peak identification can be selected.



Figure 3.10: Micron Optics HYPERION si155 [21].

Peak detection method

Peaks are detected in real time using a *zero-crossing* technique (Fig. 3.11).

This method guarantees an adaptable calibration of the instrument as it includes a threshold set that can be modified by the user depending on the need. First the signal is filtered to remove any errors due to the noise; then, from the original signal, the differential signal is obtained and the zero-crossing technique consists in the search of the zero in the signal derivative.

The differential signal could assume the zero value not only in correspondence of a peak in the original signal, but also when the latter is constant; for this reason a threshold is set to determine the λ value from which an acceptance window is considered: it means that the first zero after the threshold is reached, is the desired value.

3.3 Interaction with tissue

When a laser beam meets a tissue, the interaction with the medium is influenced by many factors, for example the wavelength and waveform of the laser beam, the output power, the optical and thermal features of the tissue.

The choice of the optimal therapy and eventually the selection of the proper laser systems is strongly connected to the knowledge of the interaction between the laser beam and the biological tissue.

During laser ablation it is extremely important to know how the light diffuses in the tissue and which are the parameters that allow a correct ablation of an entire tumor region instead of just the destruction of the cells close to the probe. Depending on the power delivered by the laser and on the exposure time, there can be different types of interaction light-tissue [23]:

1. **Photochemical interaction:** it is verified when the energy of the photons in the incident laser beam is higher than the one of the chemical bonds of

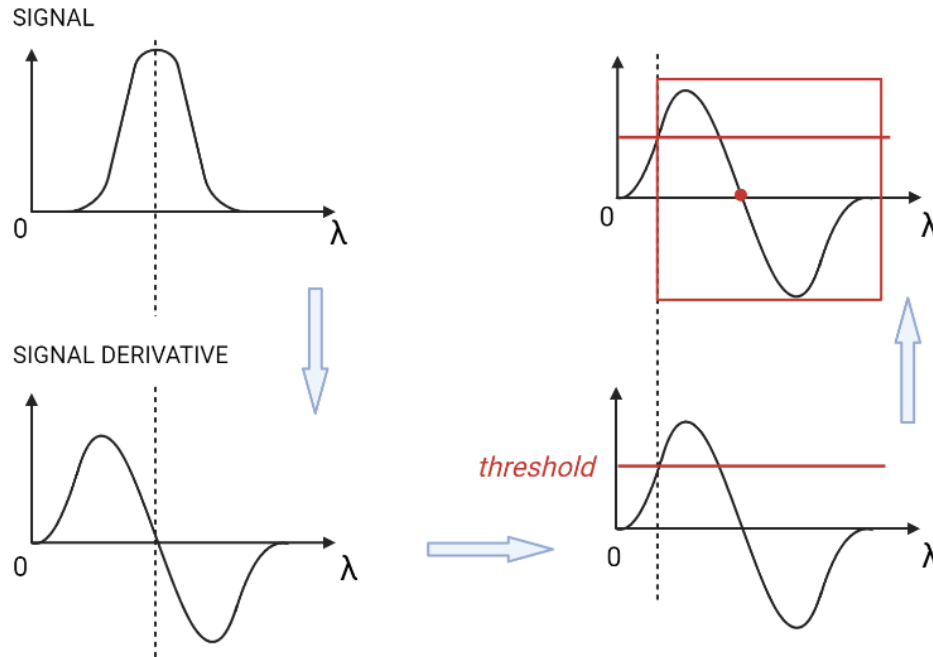
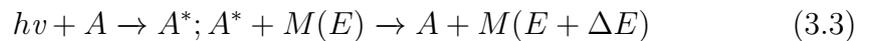


Figure 3.11: Peak detection method steps [22].

chromophores in the tissue; the energy is absorbed by the tissue and this can lead to the modification of the molecules structure or to the production of new molecules through chemical reactions activated by the laser beam.

2. **Photothermal interaction:** usually related to power densities higher than 100 W/cm^2 . The energy of the photon (usually IR wavelengths) in the laser beam is lower than the energy of the chemical bonds of the chromophores so there isn't any rupture of the peptide bonds in proteins. What happens is a two-steps reaction



where, because of the absorption of a photon, a chromophore molecule A is first excited and then it transfers its energy to a close molecule M, whose kinetic and thermal energy increases. The cell damages can vary depending on the temperatures reached and on the exposure time. Usually for temperatures lower than 50°C , if the exposure is limited no cellular death occurs; for temperatures between 50°C and 100°C the protein denaturation occurs; it means that the three-dimensional structure of the proteins is altered but the peptide bonds are not destroyed, resulting anyway in a loss of the functionality

of the protein; for temperatures higher than 100 °C the vaporization of the water in the tissue occurs and for high exposure time it results in carbonization and tissue decomposition.

3. **Photoablative interaction:** it is associated to very high power densities ($1 \times 10^7 \text{ W/cm}^2$ to $1 \times 10^8 \text{ W/cm}^2$), which are sufficient to break the molecular bonds; therefore the result is the production of repulsive molecules from a macromolecule dissociation.
4. **Electromechanical interaction:** in this case a mechanical stress is generated with the laser beam; in particular, electrical fields are generated from high power densities and they cause an optical breakdown of the material and a plasma generation; this leads to an increase of the radiation absorption and a shockwave resulting in a mechanical stress that destroys the tissue locally.

In the field of medicine, there are two main phenomena that can be studied about the interaction between the light and the matter: the absorption and the scattering.

3.3.1 Absorption

The absorption is the most important process for the clinical and diagnostic applications of lasers. Biological tissues are made by many molecules that contribute to the absorption of light and their effect depends on the wavelength of the laser. These molecules are the chromophores, which absorb some specific wavelengths giving a colour to substances.

The wavelengths used for biomedical applications of laser devices are infrared wavelengths, for which hemoglobin, lipids and water are the main chromophores. Water is absolutely the chromophore in major quantities in the human body and its absorption spectrum, together with other substances, is illustrated in Fig. 3.12.

The parameter to quantify the absorption is the **absorption coefficient** μ_a and its unit of measurement is m^{-1} .

When a light beam propagates in a biological tissue, its intensity decreases along the thickness of the medium; this dependence is expressed by the Lambert-Beer's law:

$$I(x) = I_0 \cdot e^{-\mu_a x} \quad (3.4)$$

where I_0 is the incident beam intensity (W cm^{-2}) and x is the depth at which the intensity is evaluated (m). Also transmittance (T) and absorbance (A), two dimensionless parameters, are used to describe how much light is attenuated while

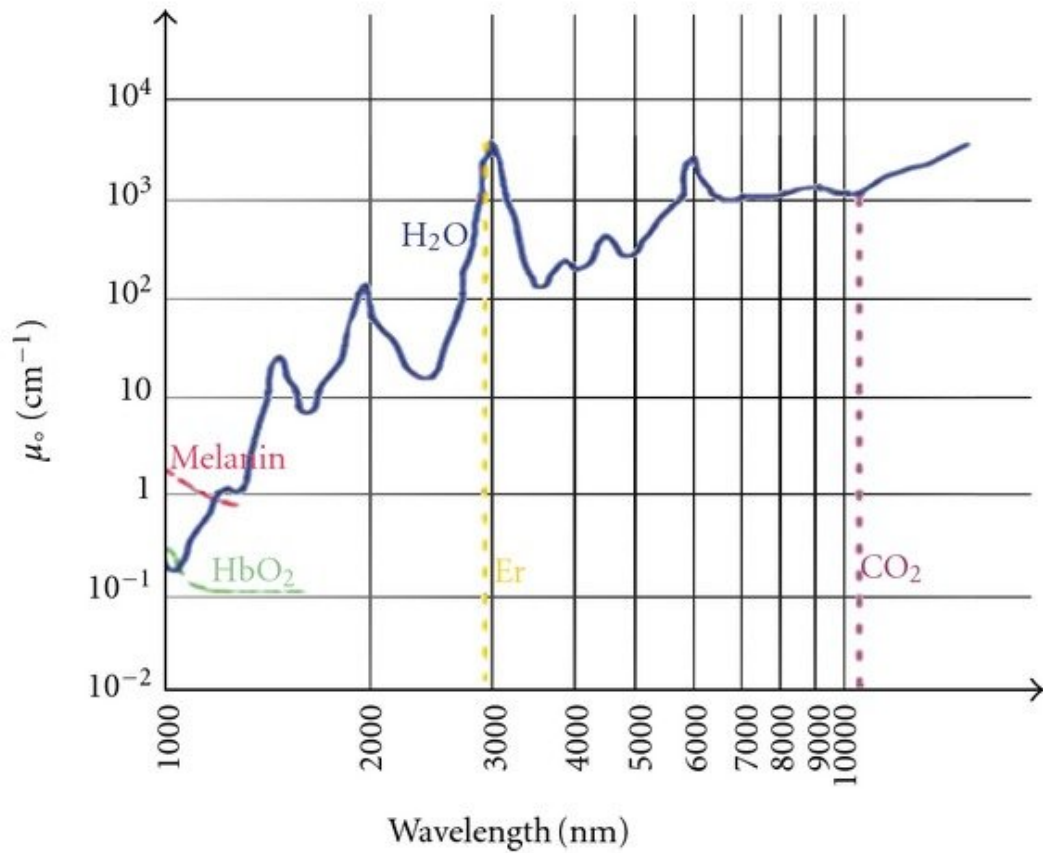


Figure 3.12: Absorption spectrum of water and other substances of interest at different wavelengths [24].

interacting with a medium:

$$T = \frac{I}{I_0} = e^{-A} \quad (3.5)$$

$$A = -\log(T) = \log \frac{I_0}{I} \quad (3.6)$$

3.3.2 Scattering

As it happens with reflection and transmission, also with scattering it is common to refer to a change of direction in the trajectory of the incident beam but in this case the deflection is random; when the photons meet the particles in the medium, part of their energy is transmitted to the electrons that start to oscillate and emit new light beams in different directions. Depending on the conservation of energy during

the interaction, there are two types of scattering: the elastic and the inelastic scattering, where the energy is preserved or not, respectively. Furthermore, this phenomenon is strongly dependent on the dimensions of the scattered particles and on the wavelength of the incident beam. Given the radius of the particle R_p and the wavelength λ , the parameter α

$$\alpha = \frac{2\pi R_p}{\lambda} \quad (3.7)$$

can be used to distinguish between:

- Rayleigh scattering, where $\alpha \ll 1$ and the particle radius is very smaller than the wavelength, the intensity of the scattered light is symmetric back and forward along the incident beam direction and it does not depend on the shape of the particle;
- Mie scattering, where $\alpha \approx 1$ and the intensity of the scattered light is asymmetric along the incident direction;
- Geometric scattering, where $\alpha \gg 1$ and the particle radius is greater than the wavelength, in this case the scatter depends strongly on the shape and orientation of the particle.

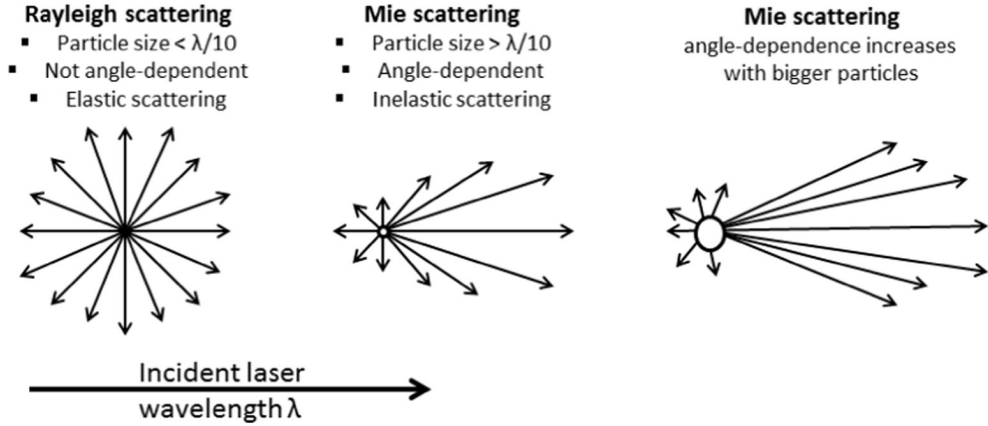


Figure 3.13: Schematic representation of the differences between Rayleigh and Mie scattering [25].

The scattering, as the absorption, leads to an attenuation of the laser beam intensity as the scattered particles diffuse a quantity of energy that is smaller or equal to the incident one. To evaluate the effect of both absorption and scattering attenuation, the *effective absorption coefficient* μ_{eff} should replace the *absorption coefficient* α in the Lambert-Beer's law in (3.4),

$$\mu_{\text{eff}} = \sqrt{3\alpha(\alpha + \alpha_s(1 - g))} \quad (3.8)$$

where α is the *absorption coefficient*, α_s is the *scattering coefficient* and g is the *anisotropy factor*. The anisotropy factor is a dimensionless quantity that expresses a measure of the amount of forward direction retained after a single scattering event (Fig. 3.14):

$$g = \langle \cos \theta \rangle \quad (3.9)$$

Three main cases can be verified:

1. $g = -1$, reversed propagation direction;
2. $g = 0$, anisotropic scattering, there are no preferential directions;
3. $g = +1$, unaltered propagation direction, no deflection occurs.

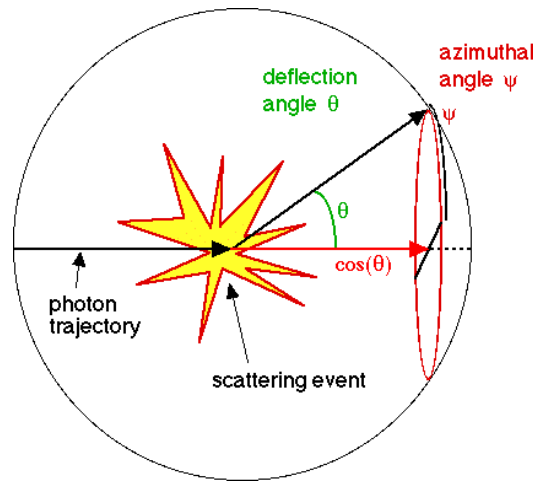


Figure 3.14: Graphical view of the deflection angle θ and of the forward direction retained after a single scattering event $\langle \cos \theta \rangle$ [26].

Chapter 4

Thermal model

During a laser ablation treatment, the response of the tissue is strongly dependent on the rising of the measured temperatures (Tab. 4.1); this means that in order to obtain a desired effect on the tissue it is necessary to maintain the temperatures in a specific range.

Temperature (°C)	Effect on tissue
$T < 45$	Change in cellular conformation (reversible)
$45 \leq T < 50$	Reduction of enzyme activity
$50 \leq T < 60$	Coagulation & proteins denaturation
$60 \leq T < 80$	Collagen destruction
$80 \leq T < 100$	Extracellular vacuoles formation
$T > 100$	Vaporization of water & destruction of vacuoles
$T > 300$	Carbonization

Table 4.1: Effects of temperature on biological tissues [27].

A thermal model is a mathematical method to obtain the predicted temperatures corresponding to specific conditions. In this way the parameters of the laser ablation (for example the power value, duration of the ablation, or duty-cycle in case of PW mode) can be set depending on the desired temperatures.

Liver laser ablation is modelled in this thesis using a Matlab® thermal model based on the *Finite Element Method (FEM)*; its description and an explanation of how it works is provided in this chapter.

4.1 Principles of Finite Element Method

The FEM is the method used to solve differential equations for the model developed in this thesis; it is widely used for partial differential equations when the domain is particularly complex or variable and allows the numerical solution of complicated problems.

Its applications are stress analysis (typically elastic deformations), the diffusion of heat inside a material body, electrostatic and magnetostatic analysis.

The problem domain is divided into subdomains called *finite elements* that are part of a discretized grid called *mesh*.

The finite elements can be triangles and quadrangles for 2D-domains or tetrahedra and hexahedron for 3D-domains; for each of them the FEM involves a problem solution expressed as a linear combination of functions called *shape functions*. The solutions are not necessary the exact values but those that give the minor error over the general solution. The method belongs to the Galerkin class method, based on the approximation of the solution to the problem expressed in its "weak form", using a linear combination of the shape functions. The coefficients of this linear combination are the unknowns of the problem after discretization.

4.1.1 FEM in Heat Conduction Problem

The equation for the heat conduction problem in solids [28] is

$$c\rho\frac{\partial T}{\partial t} = \frac{\partial}{\partial x}\left(k_x\frac{\partial T}{\partial x}\right) + \frac{\partial}{\partial y}\left(k_y\frac{\partial T}{\partial y}\right) + q_v, \quad (4.1)$$

where:

- c is the *specific heat capacity* ($\text{J kg}^{-1} \text{K}^{-1}$);
- ρ is the *mass density* (kg m^{-3});
- k_x and k_y are the *anisotropic thermal conductivity* in directions x and y ($\text{W m}^{-1} \text{K}^{-1}$);
- q_v is the *volumetric heat source* (W m^{-3}).

Initial conditions and boundary conditions are necessary to solve the problem; in particular the initial conditions are

$$T(x, y, t)|_{t=0} = T_0(x, y) \quad (4.2)$$

and three types of boundary conditions can be specified (Fig. 4.1):

1. **Dirichlet boundary condition**, where the temperature is fixed at the boundary;

$$T|_{\Gamma_T} = T_b \quad (4.3)$$

2. **Neumann boundary condition**, where it is the heat flux q_b to be fixed at the boundary;

$$\left(k_x \frac{\partial T}{\partial x} n_x + k_y \frac{\partial T}{\partial y} n_y \right) \Big|_{\Gamma_q} = q_{bn} \quad (4.4)$$

3. **mixed boundary condition**, where the convective heat flux q_h is given at boundary if the ambient temperature T_∞ and heat transfer coefficient h are known;

$$\left(k_x \frac{\partial T}{\partial x} n_x + k_y \frac{\partial T}{\partial y} n_y \right) \Big|_{\Gamma_h} = h (T_\infty - T|_{\Gamma_h}) \quad (4.5)$$

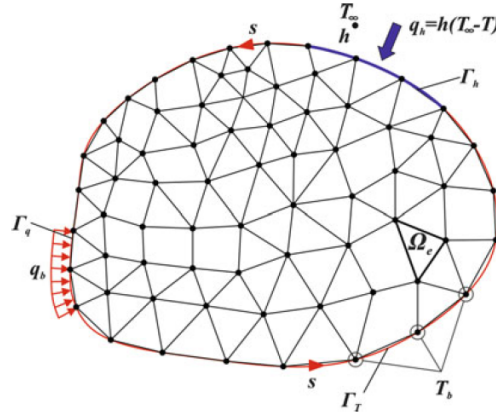


Figure 4.1: Boundary conditions representation in heat conduction problem [28].

As shown in Fig. 4.1, the finite element of the domain is called Ω_e and the temperature inside the element Ω_e is obtained from an approximation using the shape functions $\Phi_i^e(x_i, y_i)$ for the i^{th} node of the element; the shape function must satisfy

$$\sum_{i=1}^N \Phi_i^e = 1 \quad (4.6)$$

and

$$\Phi_i^e(x_i, y_i) = \delta_{ij} \quad (4.7)$$

where δ_{ij} is the Kronecker delta:

$$\delta_{ij} = \begin{cases} 1 & i = j \\ 0 & i \neq j \end{cases} \quad (4.8)$$

The temperature inside the element is

$$T^e = [\Phi^e] \{\mathbf{T}^e\} \quad (4.9)$$

where $\{\mathbf{T}^e\}$ is the vector of nodal temperatures and $[\Phi^e]$ is the shape function matrix.

The Galerkin transient heat transfer equation for a single element is

$$[\mathbf{M}^e] \{\dot{\mathbf{T}}^e\} + [\mathbf{K}^e] \{\mathbf{T}^e\} = \{\mathbf{f}^e\} \quad (4.10)$$

where $[\mathbf{M}^e]$ is the *capacitance matrix*, $[\mathbf{K}^e]$ is the *stiffness matrix* and $\{\mathbf{f}^e\}$ is the *element load vector*. A general formulation of this equation is provided for all the elements through an assembly procedure, becoming

$$[\mathbf{M}] \{\dot{\mathbf{T}}\} + [\mathbf{K}] \{\mathbf{T}\} = \{\mathbf{f}\} \quad (4.11)$$

where $[\mathbf{M}]$ is the *global capacitance matrix*, $[\mathbf{K}]$ is the *global stiffness matrix* and $\{\mathbf{f}\}$ is the *nodal load vector*.

4.2 Partial Differential Equation Toolbox

In this thesis a thermal model for laser ablation has been developed on Matlab® and in particular the Partial Differential Equation Toolbox™ has been used. A description of this toolbox is provided in this section.

Both static and dynamic analysis can be performed through a direct time integration solver; heat fluxes, temperature distributions and gradients can be calculated in a conduction heat transfer problem. 2D and 3D geometries can be directly generated or imported from mesh data or STL.

In this case, PDE thermal model needs to be created first, specifying if it is a steady-state or transient model, then the geometry must be generated or imported and the material properties must be assigned to the geometry. In particular, in case of steady-state analysis, it is sufficient to assign *thermal conductivity*, while in case of transient analysis, also *mass density* and *specific heat* must be assigned. Every internal heat source must be specified and boundary conditions and initial conditions are required. Finally the `solve` function finds the solution for the thermal problem and data can be post-processed to obtain, for example, the temperatures in the desired positions.

4.2.1 Heat Distribution in Circular Cylindrical Rod

A 3D parabolic PDE problem, necessary for the model of this project, can be reduced to a 2D problem through a coordinate transformation. This is useful to shorten the computational required time and complexity, keeping a high spatial resolution.

In this specific case it is possible to consider a cylindrical 3D geometry for which the generic equation

$$\rho c \frac{\partial T}{\partial t} - \nabla \cdot (k \nabla T) = q \quad (4.12)$$

becomes, in a cylindrical coordinate system

$$\rho c \frac{\partial T}{\partial t} - \frac{1}{r} \frac{\partial}{\partial r} \left(kr \frac{\partial T}{\partial r} \right) - \frac{1}{r^2} \frac{\partial}{\partial \theta} \left(k \frac{\partial T}{\partial \theta} \right) - \frac{\partial}{\partial z} \left(k \frac{\partial T}{\partial z} \right) = q. \quad (4.13)$$

As the cylindrical geometry is given by the rotation around the z axis of its 2D section, the problem is axisymmetric and so $\partial T / \partial \theta = 0$; the Eq. 4.13 becomes:

$$\rho c \frac{\partial T}{\partial t} - \frac{1}{r} \frac{\partial}{\partial r} \left(kr \frac{\partial T}{\partial r} \right) - \frac{\partial}{\partial z} \left(k \frac{\partial T}{\partial z} \right) = q; \quad (4.14)$$

When the PDE Toolbox is used, it is necessary to have the equations expressed in Cartesian coordinates; multiplying both sides of the Eq. 4.14 by r and defining r and z as x :

$$\rho y c \frac{\partial T}{\partial t} - \nabla \cdot (ky \nabla T) = qy. \quad (4.15)$$

The change of coordinates, therefore, requires to multiply by y the values of the *internal heat source*, the *thermal conductivity* and the *heat capacitance*.

4.3 Thermal Model for Laser Ablation

In this section the model developed in the thesis is described in detail. It is generated using the `createpde` function, specifying it is a thermal and transient problem (Appendix A.1).

4.3.1 Geometry Description and Properties Definition

A 2D-geometry is defined as a section of a cylinder representing the portion of liver irradiated. The coordinates vary from 0 to 1 cm for the r -axis and from -0.5 cm to 1 cm for the z -axis (Fig. 4.2). The probe is supposed to be along the z -axis with the delivery end in the (0,0) coordinates point. The geometry is added to the model using the `geometryFromEdges` function.

The parameters applied to the model through the `thermalProperties` function are [22]:

- Specific heat $c = 3500 \text{ (J kg}^{-1} \text{ K}^{-1}\text{)}$
- Mass density $\rho = 1070 \text{ (kg m}^{-3}\text{)}$
- Thermal conductivity $k = 0.57 \text{ (W m}^{-1} \text{ K}^{-1}\text{)}$

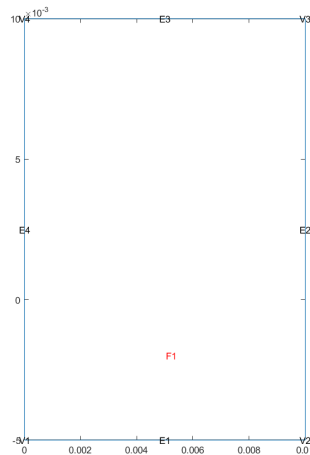


Figure 4.2: Illustration of the problem geometry obtained using a PDE Toolbox in Matlab.

A mesh grid is created (`generateMesh` function) keeping the maximum inter-nodes distance to $50 \mu\text{m}$ for a total of 271497 nodes in the geometry (Fig. 4.3).

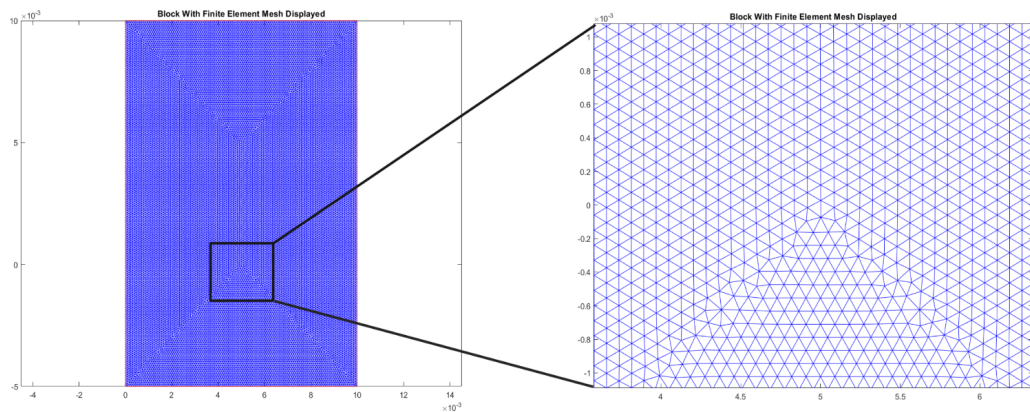


Figure 4.3: Representation of the mesh with its zoomed view, obtained using a PDE Toolbox in Matlab.

As initial condition (`thermalIC`) the ambient temperature (25 °C) is imposed for every element of the mesh, while boundary conditions (`thermalBC`) are imposed as:

- $T = 25\text{ °C}$ (ambient temperature) at the boundaries, except for the axis of rotation (Dirichlet condition);
- $\Phi = 0\text{ W m}^{-2}$ at the axis of rotation (Neumann condition);

The internal heat source (W m^{-3}) is defined in the model using the function `internalHeatSource` and, for a laser beam simulation, it derives from the modulation of an optical source intensity (W m^{-2}) through the absorption coefficient. In particular two different approaches have been explored for this thesis: a gaussian laser beam and a rectangular laser beam.

- **Gaussian laser beam** [29, 30]

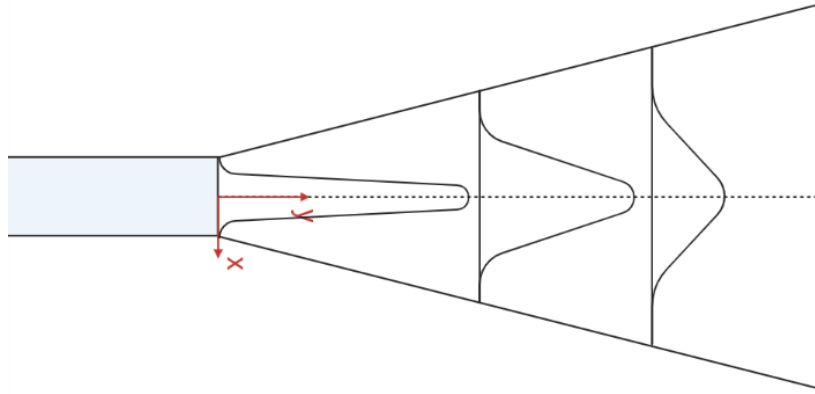


Figure 4.4: Representation of the gaussian laser beam on a 2D-surface

The internal heat source in r, z (x, y) directions is:

$$q(r, z) = \begin{cases} \mu_a \cdot \frac{2P}{\pi\sigma^2} \cdot e^{-\frac{2r^2}{\sigma^2}} \cdot e^{-\mu_{\text{eff}}z} & z \geq 0 \\ 0 & z < 0 \end{cases} \quad (4.16)$$

where:

- $\mu_a = 76\text{ m}^{-1}$ (linear absorption coefficient)
- $P = 0.5\text{ W}$ to 2 W (optical power)

- $\sigma = \sigma_0 \cdot \sqrt{\left[1 + \left(\frac{\lambda z}{n\pi\sigma_0^2}\right)^2\right]}$
- $\lambda = 915 \text{ nm}$ (emission wavelength)
- $\sigma_0 = 50 \text{ }\mu\text{m}$ (about half of the radius of the emitting probe)
- $n = 1.33$ (refractive index)
- $\mu_{\text{eff}} = \sqrt{3\mu_a \cdot (\mu_a + \mu_s \cdot (1 - g))}$
- $\mu_s = 10015 \text{ m}^{-1}$ (scattering coefficient)
- $g = 0.9$ (anisotropy coefficient)

- **Rectangular laser beam**

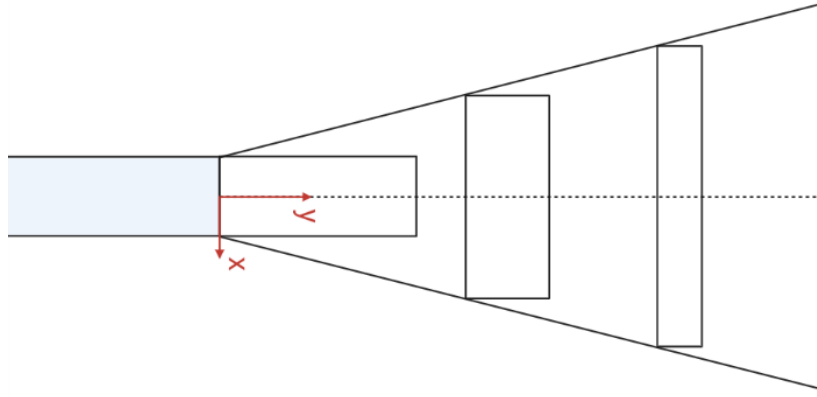


Figure 4.5: Representation of the rectangular laser beam on a 2D-surface

The internal heat source in r, z (x, y) directions is:

$$q(r, z) = \begin{cases} \mu_a \cdot \frac{P}{\pi\sigma^2} \cdot \text{rect}(r, z) \cdot e^{-\mu_{\text{eff}}z} & z \geq 0 \\ 0 & z < 0 \end{cases} \quad (4.17)$$

where:

- $\mu_a = 76 \text{ m}^{-1}$ (linear absorption coefficient)
- $P = 0.5 \text{ W}$ to 2 W (optical power)
- $\sigma = \sigma_0 + \tan(\alpha) \cdot z$
- $\sigma_0 = 50 \text{ }\mu\text{m}$ (about half of the radius of the emitting probe)
- $\alpha = \arcsin(NA/n)$

- $NA = 0.22$ (numerical aperture)
- $n = 1.33$ (refractive index)
- $\mu_{\text{eff}} = \sqrt{3\mu_a \cdot (\mu_a + \mu_s \cdot (1 - g))}$
- $\mu_s = 10015 \text{ m}^{-1}$ (scattering coefficient)
- $g = 0.9$ (anisotropy coefficient)
- $\text{rect}(r, z) = \begin{cases} 1 & |r| \leq \sigma \\ 0 & |r| > \sigma \end{cases}$

It can be noticed that the internal heat source in (0,0) in case of a gaussian beam is twice what the internal source in (0,0) in case of a rectangular beam is. This is because the intensity in case of rectangular beam must be the half to keep the same value of power, as proved in the comparison between Eq. 4.19 and Eq. 4.22.

The intensity of a Gaussian beam is:

$$I(r) = I_0 \cdot e^{-\frac{2r^2}{\sigma_0^2}} \quad (4.18)$$

$$\begin{aligned} P &= \frac{1}{2}Y \int_{\Sigma} I(r)d\Sigma = \frac{1}{2}Y I_0 \int_0^{2\pi} d\phi \int_0^{\infty} r \cdot e^{-\frac{2r^2}{\sigma_0^2}} dr \\ &= \frac{1}{2}Y I_0 2\pi \left[-\frac{\sigma_0^2}{4} e^{-\frac{2r^2}{\sigma_0^2}} \right]_0^{\infty} = \frac{\sigma_0^2}{4} Y I_0 \pi \end{aligned} \quad (4.19)$$

Therefore the intensity is:

$$I_0 = \frac{4P_0 Z_0}{n\pi\omega_0^2} \quad (4.20)$$

where:

- $Z_0 = \frac{n}{Y}$ is the impedance in the vacuum;
- Y is the admittance in the medium with refractive index n .

The intensity of a rectangular beam is:

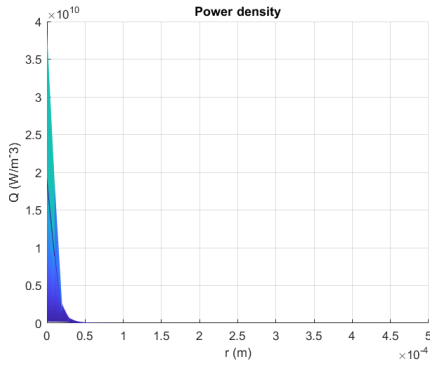
$$I(r) = I_0 \cdot \text{rect}(r) \quad (4.21)$$

$$\begin{aligned} P &= \frac{1}{2}Y \int_{\Sigma} I(r)d\Sigma = \frac{1}{2}Y I_0 \int_0^{2\pi} d\phi \int_0^{\sigma_0} r dr \\ &= \frac{\sigma_0^2}{2} Y I_0 \pi \end{aligned} \quad (4.22)$$

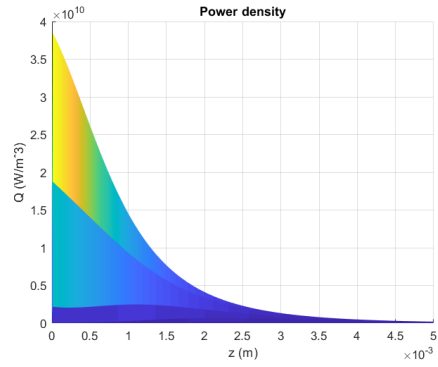
Therefore the intensity is:

$$I_0 = \frac{2P_0Z_0}{n\pi\sigma_0^2} \quad (4.23)$$

In Fig. 4.6, 4.7 it is possible to graphically see the factor "2" of dependence between the power density in case of a gaussian or rectangular beam. The figures show both the distributions along the r-axis and z-axis for a power value of 2 W.

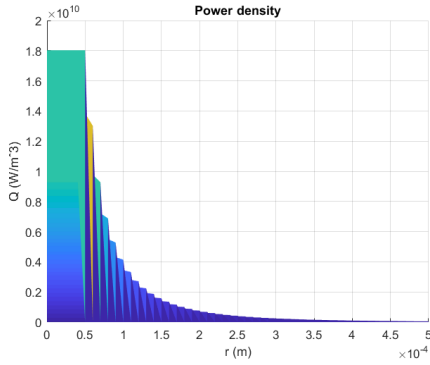


(a) Power density distribution in r-direction.

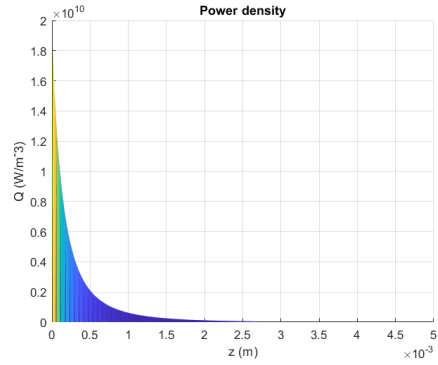


(b) Power density distribution in z-direction.

Figure 4.6: Power density distributions for the gaussian model. 2 W



(a) Power density distribution in r-direction.

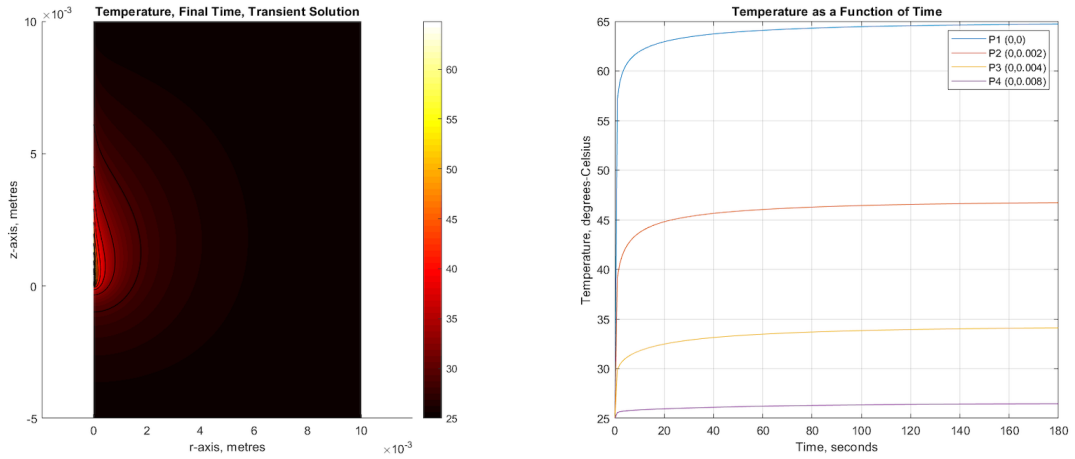


(b) Power density distribution in z-direction.

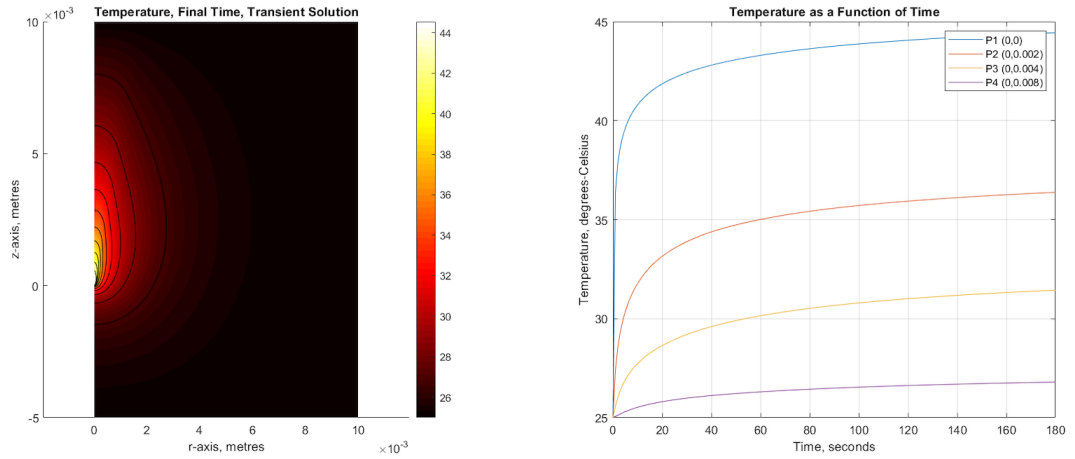
Figure 4.7: Power density distributions for the rectangular model. 2 W

4.3.2 Results and Conclusions

The solution of the problem is obtained using a `solve` function; a defined interval of time is analysed, in this case 3 minutes. Using a `PDEplot`, for both the gaussian and rectangular beam, a color map of the temperature distribution at the final time step is shown in Fig. 4.8, 4.9, 4.10, 4.11, where also the temperature graph in different positions by the time is represented.

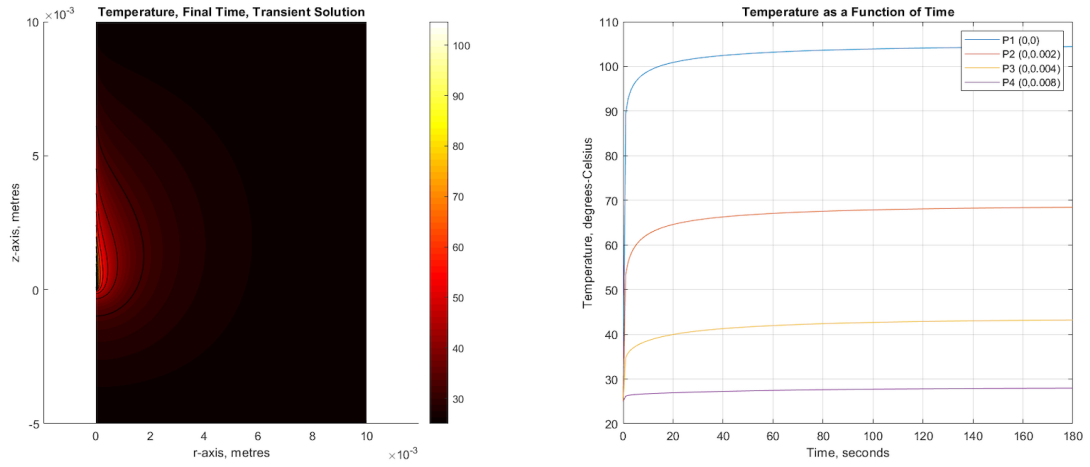


(a) Temperature distribution and trends in different positions of the geometry. Results for the gaussian model.

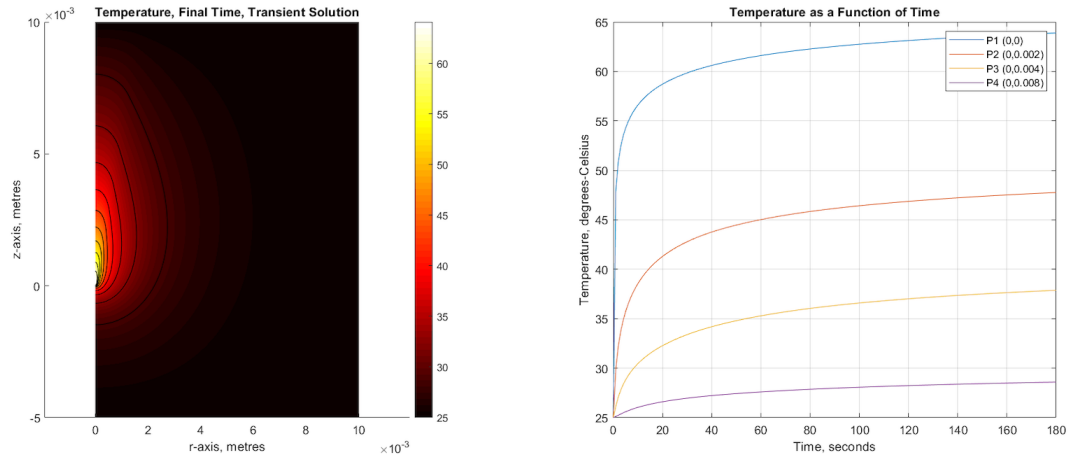


(b) Temperature distribution and trends in different positions of the geometry. Results for the gaussian model.

Figure 4.8: Comparison of the results for both gaussian and rectangular model at 0.5 W.



(a) Temperature distribution and trends in different positions of the geometry. Results for the gaussian model.

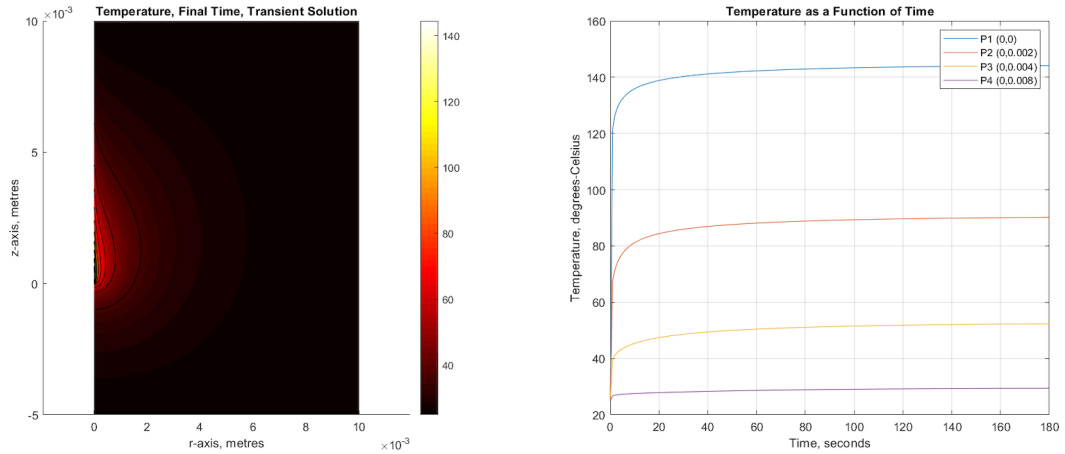


(b) Temperature distribution and trends in different positions of the geometry. Results for the gaussian model.

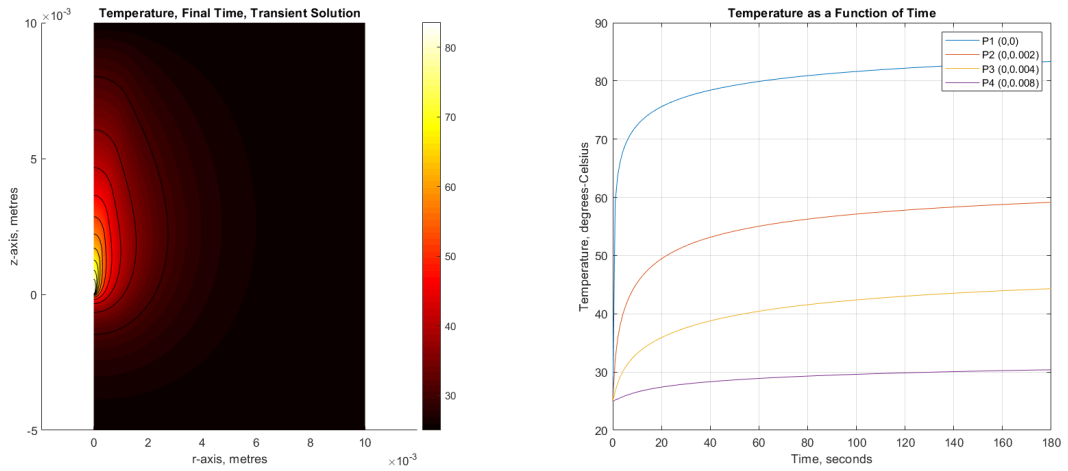
Figure 4.9: Comparison of the results for both gaussian and rectangular model at 1 W.

It is possible to notice that in general, the temperatures reached with the gaussian beam are higher than the ones reached with the rectangular beam. This is because the gaussian shape is "narrower" and the power densities are higher compared to the ones of the rectangular beam. A smaller portion of tissue absorbs very high power intensities in the first case while in the second case larger regions of the tissue are heated even if they reach lower temperatures.

The temperatures reached for both the models are included in the range of the



(a) Temperature distribution and trends in different positions of the geometry. Results for the gaussian model.

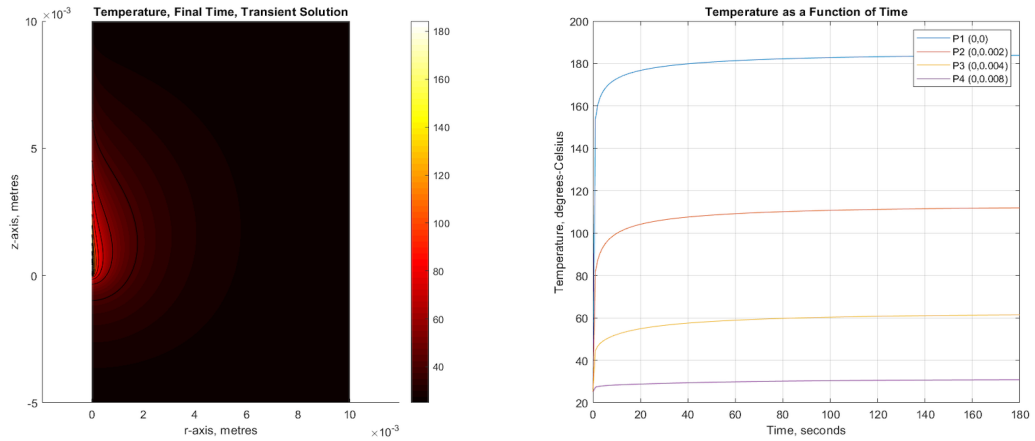


(b) Temperature distribution and trends in different positions of the geometry. Results for the gaussian model.

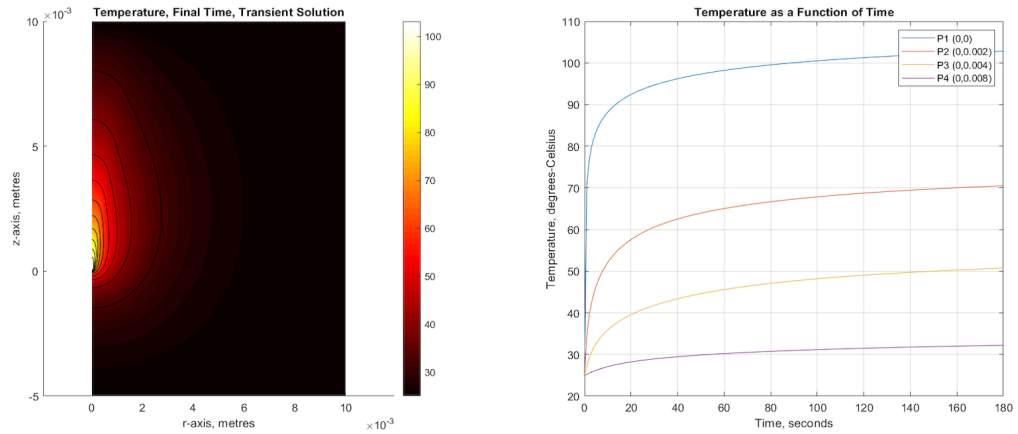
Figure 4.10: Comparison of the results for both gaussian and rectangular model at 1.5 W.

ablation temperatures (Tab. 4.1), and also the ablation region is well described from the models; in Chapter 6 a comparison between the measured and computed temperatures will be provided.

As noticed from the theory, the gaussian beam better represents a single mode emitting probe while the rectangular beam gives a representation closer to a multimode emitting probe.



(a) Temperature distribution and trends in different positions of the geometry. Results for the gaussian model.



(b) Temperature distribution and trends in different positions of the geometry. Results for the gaussian model.

Figure 4.11: Comparison of the results for both gaussian and rectangular model at 2 W.

The value of power in the described model can be modified depending on the desired results. Of course the ablation can be reached or not by varying the power set, according to the Tab. 4.1. The model is a simplified method to describe approximately the procedure of laser ablation. It is not exactly comparable with what happens during a in-vivo laser treatment because aspects as the blood perfusion or the metabolic heat, haven't been considered in the model. Future adjustments could include the evaluation of these aspects to make the model even closer to the reality.

Chapter 5

Experimental Activities

5.1 FBGs Characterization

A sensor usually exploits a mathematical relationship between an input physical quantity and an output measured one. The characterization of a sensor is the process to obtain the parameters of this relationship and it is fundamental for a proper use of the sensor. The linear equation for the Bragg wavelength considering the only effect of the temperature is

$$\lambda_B = \lambda_0 + k_T \cdot T \quad (5.1)$$

and in this case the temperature is the required quantity while the wavelength is the measured value.

For each FBG the characterization is aimed to obtain the values:

- λ_0 (nm), that is the Bragg wavelength when $T = 0^\circ\text{C}$;
- k_T ($\text{nm } ^\circ\text{C}^{-1}$), which is the sensitivity of the sensor and describes the extent of the of λ_B variation with the temperature.

In this section only the characterization of two 20-FBGs-arrays have been reported, but the same procedure has been adopted to characterize all the arrays used during the experimental part. Both the arrays have been fabricated using a femtosecond laser on single-mode fibres even though they have different features due to their dissimilar structure, illustrated in Fig. 5.1.

In one array the gratings are staggered into the core and it will be labelled HighDensity-FBGs-array to indicate that usually the distance between the centers of the gratings is lower, leading to a higher density of FBGs. The other array instead is characterized by a straight series of gratings and will be labelled Straight-FBGs-array. The tests carried out on the fibres in this phase need the usage of a reference temperature sensor, an optical interrogator, a heating plate and a computing environment to process the acquired data.

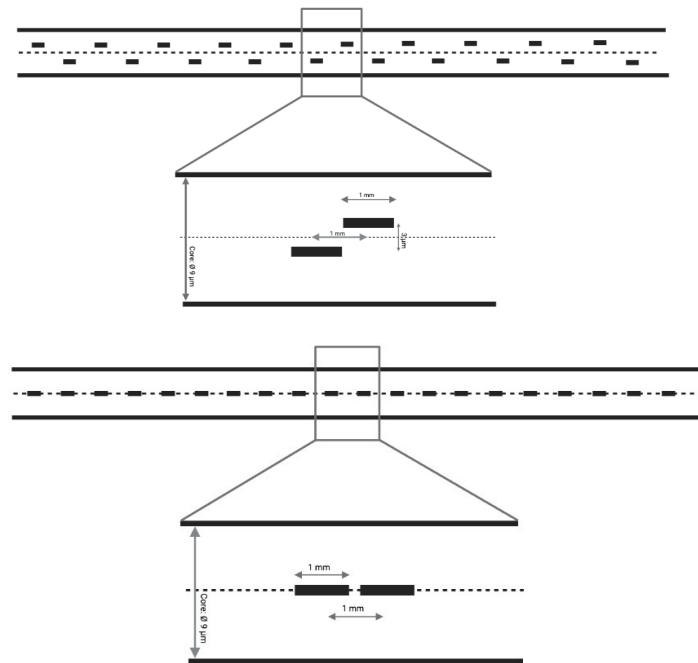


Figure 5.1: Structure of HighDensity-FBGs array and Straight-FBGs array.

5.1.1 Set-up and Instrumentation

A schematic of the two arrays characteristics is reported before the description of the procedure of characterization:

- Straight array, single mode fiber
 - *core* diameter 9 μm ;
 - *cladding* diameter 125 μm ;
 - 1 mm between FBGs centres;
 - 1 mm extension for each FBG;
 - FBGs on the same axis in the core;
- High-density array, single mode fiber
 - *core* diameter 9 μm ;
 - *cladding* diameter 125 μm ;
 - 1 mm between FBGs centres;
 - 1 mm extension for each FBG;

- FBGs alternated on 2 parallel axes in the core;

The required instrumentation is:

- Optical interrogator Micron Optics HYPERION si155 and related software Enlight to save the acquired data.
 - Four available channels;
 - Wavelength range: 1500 nm to 1600 nm;
 - Sampling rate: 1 kHz;
 - Text file data writing interval: 1 s.
- Thermocouple J-type from National Instruments (NI) with USB-TC01. The instant-DAQ technology is provided with an integrated software, whose interface is reported in Fig. 5.2 and shows the temperature in real-time. The acquired data are saved in a text-file containing both time of the registration and temperature for each instant of time. The thermocouple features are:
 - Resolution: 0.0625 °C;
 - Max temperature error: 1.5 °C;
 - Highest sample rate: 4 S/s;
 - Resolution of ADC: 20bits.

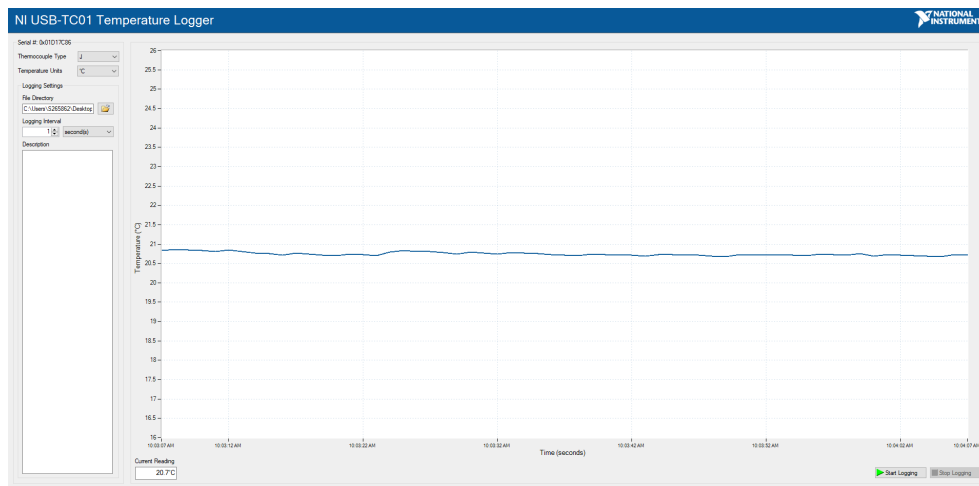


Figure 5.2: J-type thermocouple (NI) software interface.

- Electric heating plate (max 100°C reached in this case);
- Metal block.

The basic principle of the characterization is to heat the fibres and acquire the measured wavelengths with the Micron Optics (Fig. 5.3, 5.4) while the thermocouple acquires the reference temperatures. In particular the electric plate brings the fibres up to 100°C and then they are allowed to cool. The wavelength for each instant of time is related to the temperature measured at the same time according to the Eq. 5.1, to obtain the values λ_0 and k_T for each FBG. Subsequently a verification is performed by evaluating the error between the measured wavelengths and those obtained with the formula.

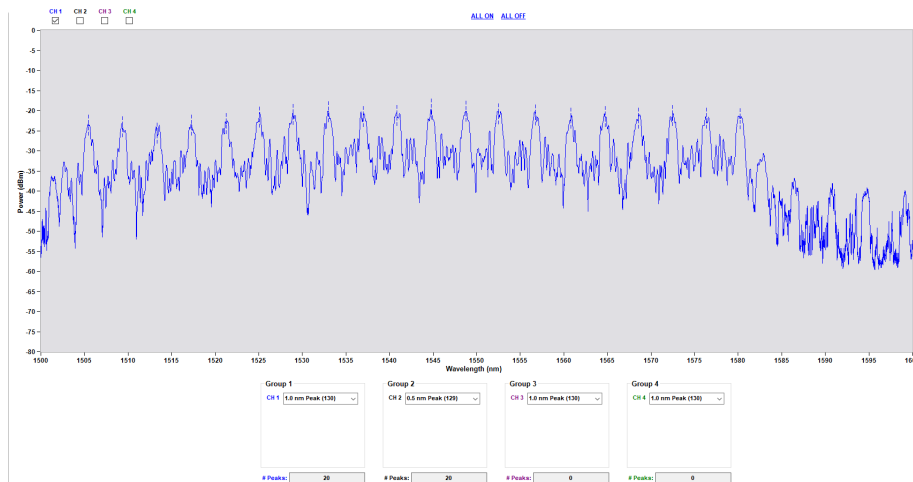


Figure 5.3: MicronOptics interface for the 20 reflection peaks of the FBGs. Straight.

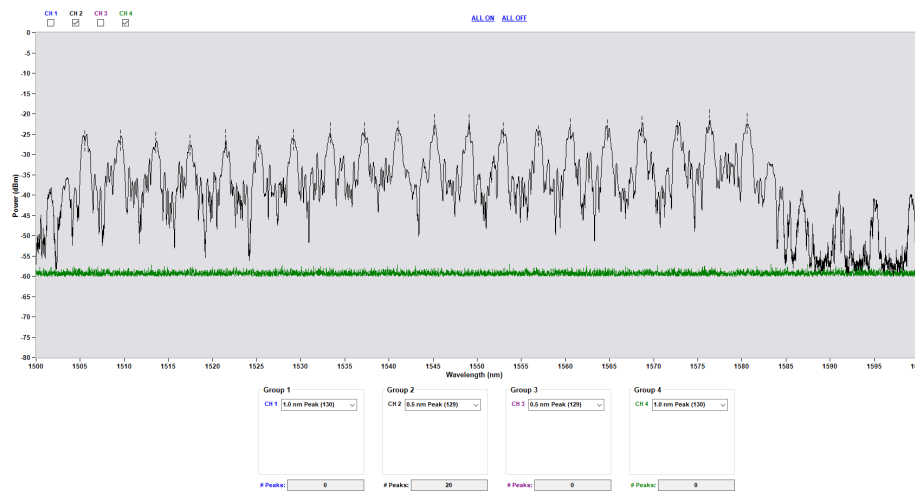


Figure 5.4: MicronOptics interface for the 20 reflection peaks of the FBGs. HD.

The setup (Fig. 5.5) includes two glass capillary tubes in which the arrays are inserted to reduce the effects of undesired mechanical stresses on the fibres. These capillary tubes are not directly positioned on the heating plate: a metal block is used to get higher thermal inertia and guarantee a slow increasing of temperatures. The entire system is covered by an insulating block to reduce heat losses in the external environment.

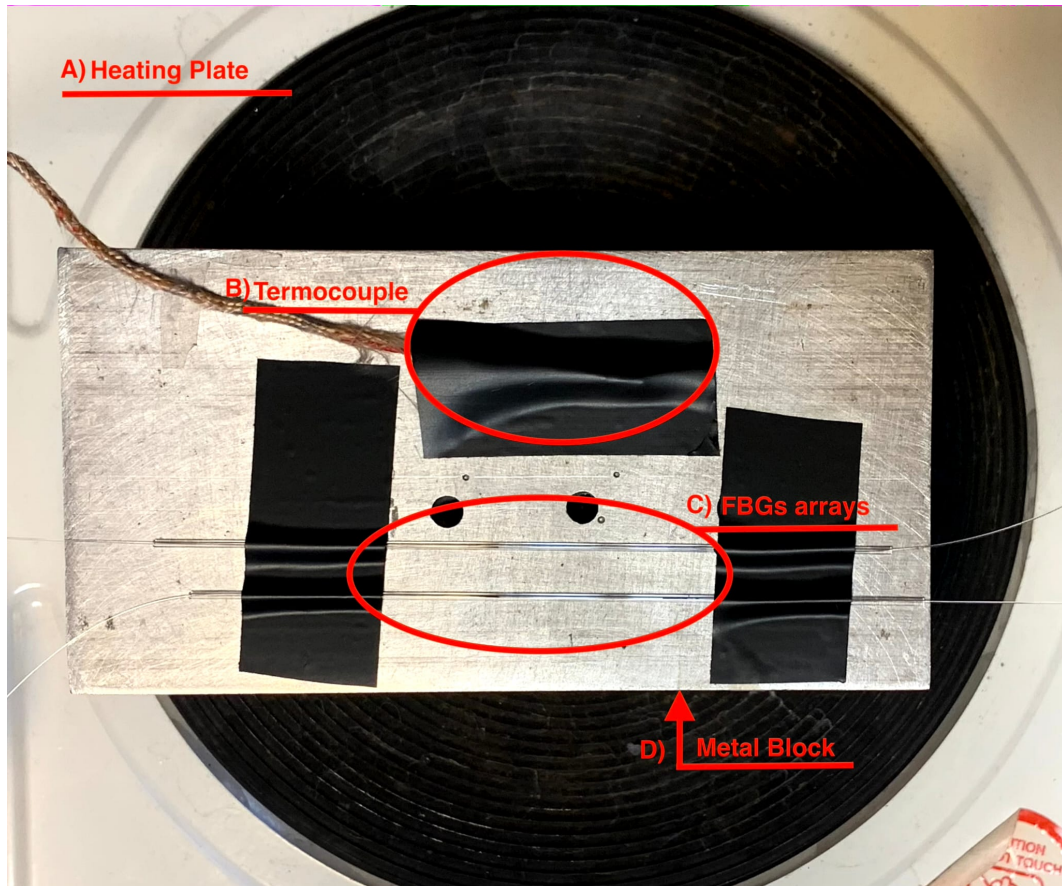


Figure 5.5: Setup for FBGs-arrays characterization.

During the procedure the arrays are connected to channels 1 and 2 of the Micron Optics: data are sent in a text file via Ethernet to a PC provided with Enlight software.

The text file contains all the saving instants of time and for each of them, the number of FBGs detected in the channels and the value of the recorded Bragg wavelengths for the FBGs. The thermocouple is positioned on the metal block together with the glass capillaries and powered by USB connection to the PC. Its

self launched software provides a text file containing the sampling instants and the value of temperature for each of them.

The acquired data from the Micron Optics and from the thermocouple have been post-processed through an implemented Matlab® code (Appendix A.2). Only the values in the descending section of the temperature curve were considered as the slope is smaller there compared to the one of the rising part. The signals have been filtered to reduce the noise contribution: a moving average filter was used, where the number of samples mediated has been chosen depending on the duration of the signals. After filtering, the Micron Optics and thermocouple data have been aligned considering the coincident instants of time and the Matlab® function *polyfit* has been used for the linear relationship between Bragg wavelengths and temperature to obtain the parameters λ_0 and k_T .

5.1.2 Results and Conclusions

In Tab 5.1, 5.2 the results for λ_0 and k_T are reported for each FBG of the two arrays. It can be noticed that the sensitivity is always close to the value $10 \text{ pm } ^\circ\text{C}^{-1}$ because it is a characteristic of the material used for the FBGs. The obtained values are in agreement with the data found in literature for type of FBGs used. The offset wavelengths λ_0 are similar for the FBGs of the two arrays as they have been fabricated with the same Bragg wavelength range.

	FBG1	FBG2	FBG3	FBG4	FBG5	FBG6	FBG7
λ_0 (nm)	1505.1	1509.1	1512.9	1516.9	1520.9	1524.6	1528.6
k_T (nm/ $^\circ\text{C}$)	0.0122	0.0123	0.0123	0.0123	0.0123	0.0123	0.0123
	FBG8	FBG9	FBG10	FBG11	FBG12	FBG13	FBG14
λ_0 (nm)	1532.6	1536.6	1540.5	1544.4	1548.4	1552.2	1556.4
k_T (nm/ $^\circ\text{C}$)	0.0124	0.0125	0.0125	0.0125	0.0126	0.0126	0.0126
	FBG15	FBG16	FBG17	FBG18	FBG19	FBG20	
λ_0 (nm)	1560.4	1564.3	1568.2	1572.1	1575.9	1579.8	
k_T (nm/ $^\circ\text{C}$)	0.0126	0.0127	0.0127	0.0128	0.0128	0.0128	

Table 5.1: λ_0 and k_T values for each FBG. Straight.

	FBG1	FBG2	FBG3	FBG4	FBG5	FBG6	FBG7
λ_0 (nm)	1505.3	1509.3	1513.3	1517.2	1521.2	1524.9	1528.9
k_T (nm/°C)	0.0108	0.0108	0.0108	0.0109	0.0109	0.0109	0.0110

	FBG8	FBG9	FBG10	FBG11	FBG12	FBG13	FBG14
λ_0 (nm)	1533.1	1536.9	1540.8	1544.9	1548.8	1552.7	1556.7
k_T (nm/°C)	0.0110	0.0111	0.0111	0.0111	0.0111	0.0112	0.0112

	FBG15	FBG16	FBG17	FBG18	FBG19	FBG20
λ_0 (nm)	1560.3	1564.5	1568.4	1572.4	1576.1	1580.3
k_T (nm/°C)	0.0112	0.0112	0.0113	0.0113	0.0113	0.0113

Table 5.2: λ_0 and k_T values for each FBG. HD

The calibration lines and the scatter plot of the characterization data have been plotted to graphically see the error between the measured wavelengths (magenta dots) and the interpolated wavelengths (blue line). For each of the arrays the interpolation line of the FBG 10 and a zoom of it are reported in Fig. 5.6, 5.7, 5.8, 5.9. It is possible to notice that a negligible error occurs between the measured and estimated values.

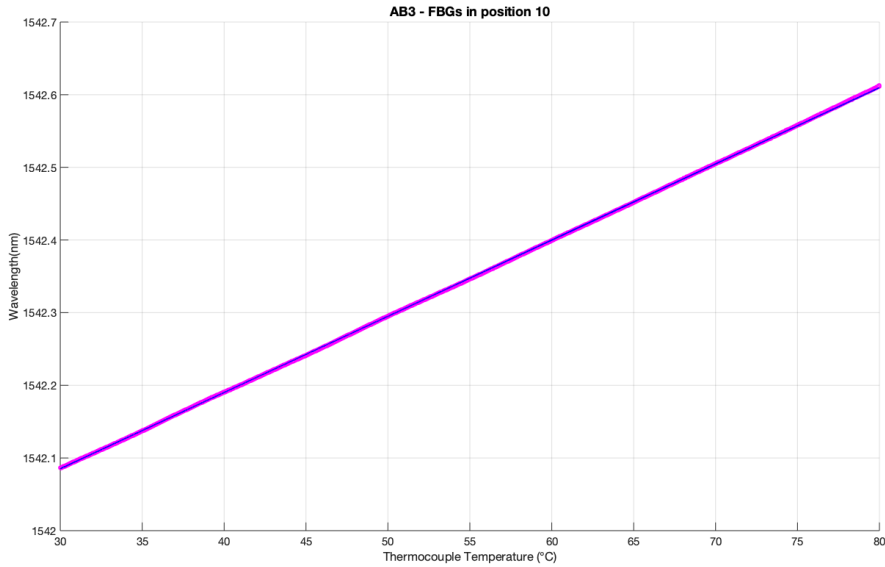


Figure 5.6: Calibration line: in blue the interpolating line is presented, in magenta the recorded data. Straight array.

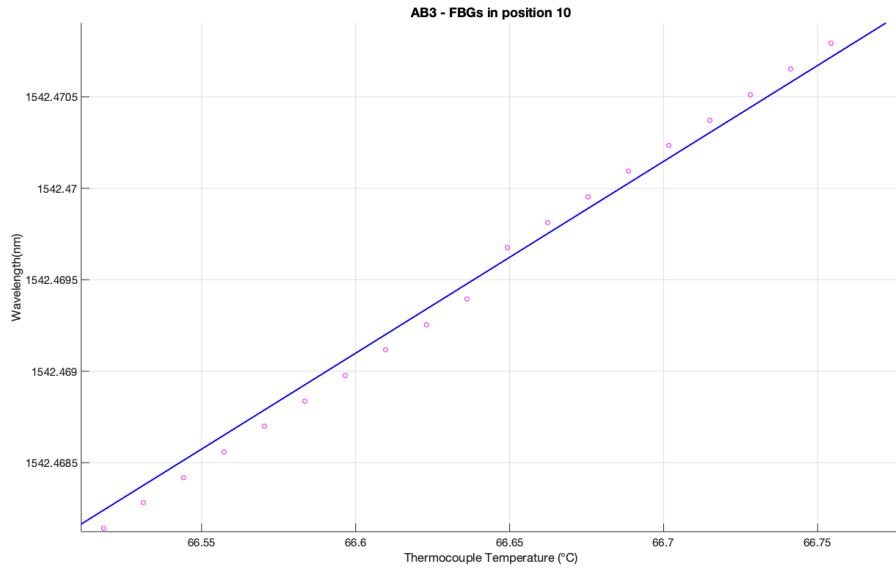


Figure 5.7: Zoom of the calibration line: the point recorded overpass the interpolating line. Straight array.

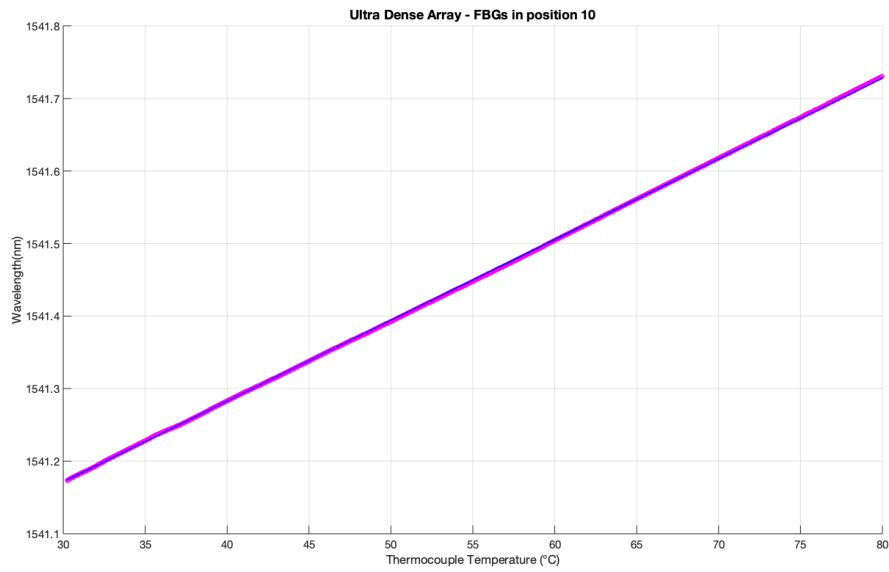


Figure 5.8: Calibration line: in blue the interpolating line is presented, in magenta the recorded data. Ultradense array.

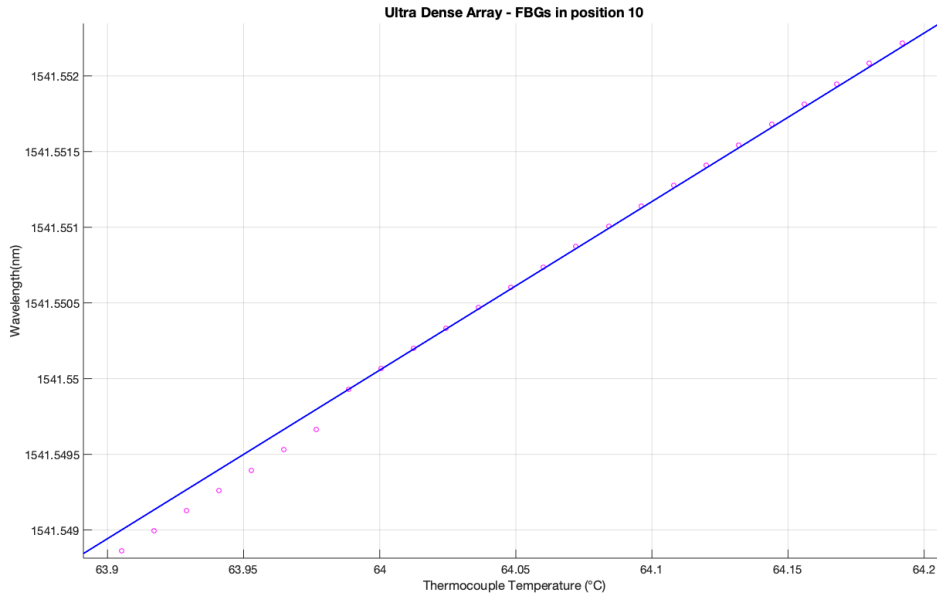


Figure 5.9: Zoom of the calibration line: the point recorded overpass the interpolating line. Ultradense array.

After the calculation of the λ_0 and k_T parameters, the temperatures have been reconstructed from the recorded wavelengths, using the Eq. 5.1. These, for each array, have been compared with the thermocouple temperatures. In Fig. 5.10, 5.11 the comparisons for the FBG 10 (the central FBG of the array) are reported. Graphically the results of the characterization are encouraging as the wavelength error, for each value of temperature, is comparable to the resolution of the MicronOptics (10 pm). The same happens for all the other FBGs that are not reported in figure.

An estimate of the success of the characterization is given by the evaluation of the maximum deviation and the error between the measured and estimated values. The maximum deviation have been calculated dividing the difference between the measured and the evaluated wavelengths by sensitivity k_T , its unit of measure is the degree Celsius ($^{\circ}C$); the error instead has been calculated dividing the difference between the measured and the evaluated wavelengths by the measured wavelengths: it is dimensionless. Both of them are reported for each of the FBGs of the arrays in Tab. 5.3, 5.4.

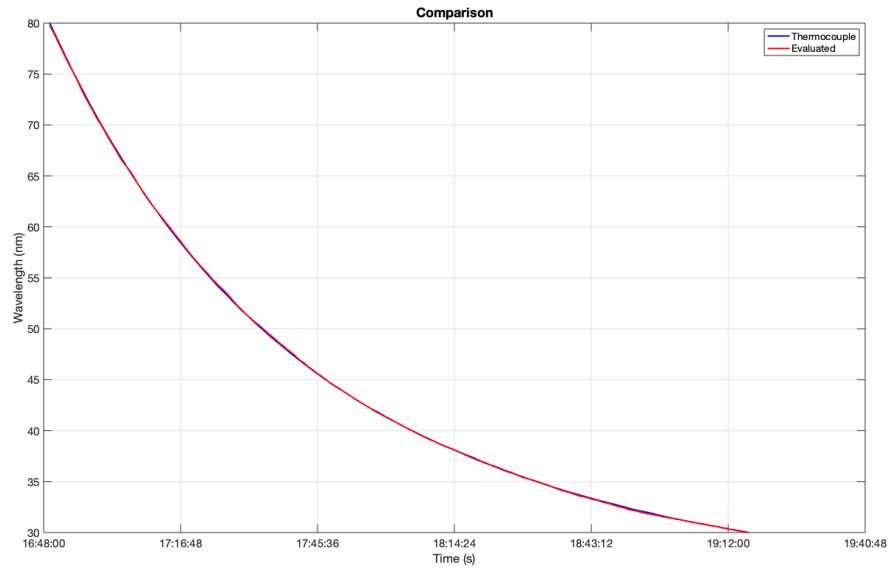


Figure 5.10: Comparison curve between the Straight-array and the thermocouple temperatures.

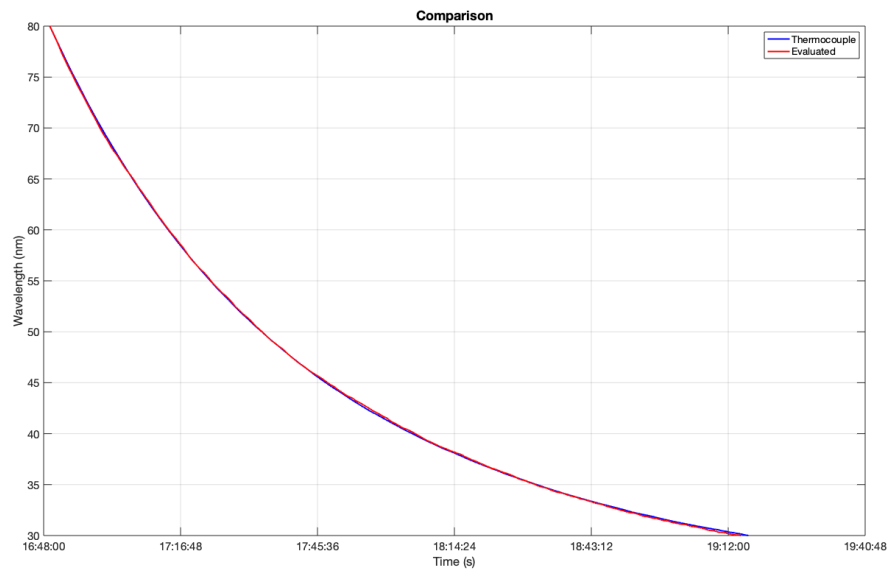


Figure 5.11: Comparison curve between the HighDensity-array and the thermocouple temperatures.

	FBG1	FBG2	FBG3	FBG4	FBG5	FBG6	FBG7
$\Delta T_{\max}(\text{°C})$	0.411	0.366	0.199	0.171	0.225	0.245	0.274
Error	0.0107	0.0057	0.0064	0.0042	0.0097	0.0063	0.0060

	FBG8	FBG9	FBG10	FBG11	FBG12	FBG13	FBG14
$\Delta T_{\max}(\text{°C})$	0.202	0.169	0.197	0.182	0.236	0.218	0.174
Error	0.0070	0.0063	0.0045	0.0039	0.0034	0.0044	0.0063

	FBG15	FBG16	FBG17	FBG18	FBG19	FBG20
$\Delta T_{\max}(\text{°C})$	0.207	0.157	0.175	0.142	0.134	0.149
Error	0.0035	0.0027	0.0031	0.0044	0.0053	0.0047

Table 5.3: Maximum temperature variation during the descending thermal gradient and maximum relative temperature error for each FBG. Straight

	FBG1	FBG2	FBG3	FBG4	FBG5	FBG6	FBG7
$\Delta T_{\max}(\text{°C})$	0.197	0.208	0.179	0.169	0.243	0.269	0.239
Error	0.0045	0.0052	0.0034	0.0052	0.0037	0.0061	0.0071

	FBG8	FBG9	FBG10	FBG11	FBG12	FBG13	FBG14
$\Delta T_{\max}(\text{°C})$	0.246	0.210	0.230	0.171	0.159	0.218	0.212
Error	0.0049	0.0063	0.0076	0.0047	0.0048	0.0047	0.0044

	FBG15	FBG16	FBG17	FBG18	FBG19	FBG20
$\Delta T_{\max}(\text{°C})$	0.164	0.217	0.188	0.229	0.175	0.157
Error	0.0047	0.0056	0.0057	0.0058	0.0048	0.0061

Table 5.4: Maximum temperature variation during the descending thermal gradient and maximum relative temperature error for each FBG. HD

It is clear that the maximum temperature deviation is negligible compared to the temperature values (2 orders of magnitudes smaller) and the relative error in the worst of the cases is less than 0.75%: this can confirm the success of the characterization.

5.2 Self-Heating Evaluation

The FBG sensors have been used during the ex-vivo liver ablation experiments. It is required that they measure the temperature reached by the tissue without being affected by a self-heating phenomenon. Several tests have been performed to evaluate the self-heating contribute when the FBGs are directly irradiated by the probe connected to the laser. The tests are also finalised to evaluate the stability of the sensor and for this reason different setups have been tested: in air and in water. For these tests only one array has been used, the straight one, whose characteristics are described in Section 5.1.

5.2.1 Set-up and Measurements

As stated before, these experiments have been performed both in air and in water. Different values of power have been delivered and also tests with no power delivered have been done. The organization of the tests is described in Tab. 5.5.

TEST	POWER	ENVIRONMENT
1	Laser off	air
2	0.5 W	air
3	1 W	air
4	1.5 W	air
5	Laser off	water
6	0.5 W	water
7	1 W	water
8	1.5 W	water

Table 5.5: Organization of the tests performed to evaluate the self-heating effect.

For tests 1 to 4 the setup (Fig. 5.12) includes a metal support on which the FBGs array is positioned and kept at a fixed distance from the delivery fibre. The ends of the array are inserted in two glass capillaries, fixed to the metal support through transparent tape, to avoid any mechanical stretching that could compromise the measures. The probe is instead inserted in a rubber tube fixed to another metal support to guarantee safety and stability to the system. The probe is perpendicular to the FBGs array in the plane and kept in contact with it during the whole duration of the experiments.

A similar setup was used for the tests 5 to 8 with the main difference of keeping the whole system completely submerged in water. Both the setups also include an

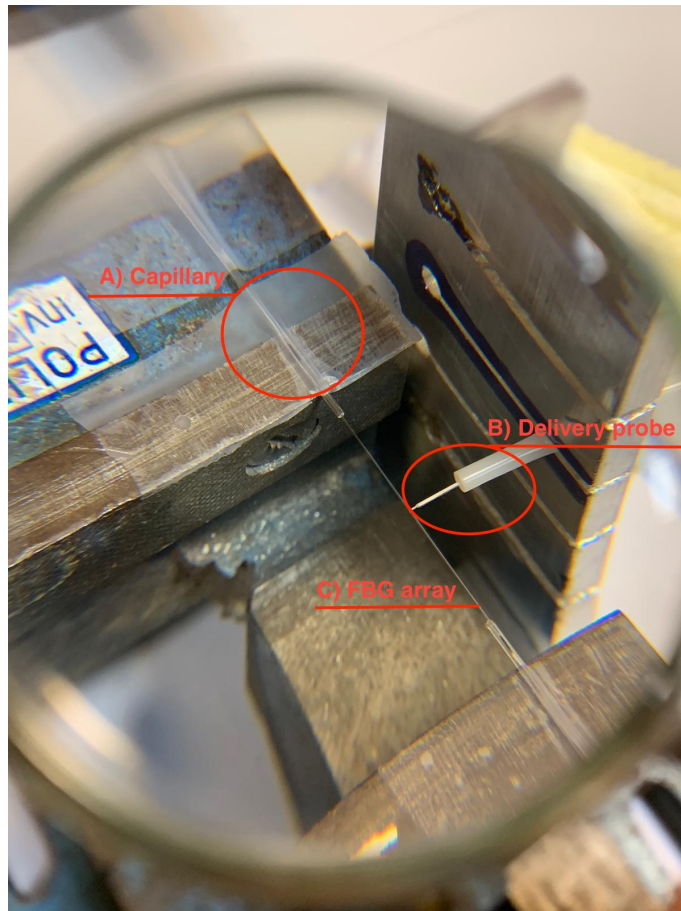


Figure 5.12: Setup for experimental self-heating evaluation in air.

insulating covering system when the laser is on for reasons of safety.

For the tests 2 to 4 and 6 to 8 (laser on) the duration of data acquisition was 1 minute during which the laser was activated for 10 seconds; the text file compiling rate was 5 Hz. For the tests 1 and 5 instead, as the laser was off, a longer recording of 5 minutes was performed and the text file compiling rate was 2 Hz. The laser device used for these experiments (Fig. 5.13) is the result of a previous project of thesis [27].

It includes a high-power laser diode (LuOcean Mini 8 by Lumics): two diodes are used to emit wavelengths in IR range, 915 nm and 1470 nm; for these experiments only the emission at 915 nm has been used. The laser is provided with a further diode to emit in the visible range (510 ± 10 nm) as a targeting beam. It can work both in Continuous Wave mode (CW) and Pulsed Wave mode (PM) but only CW

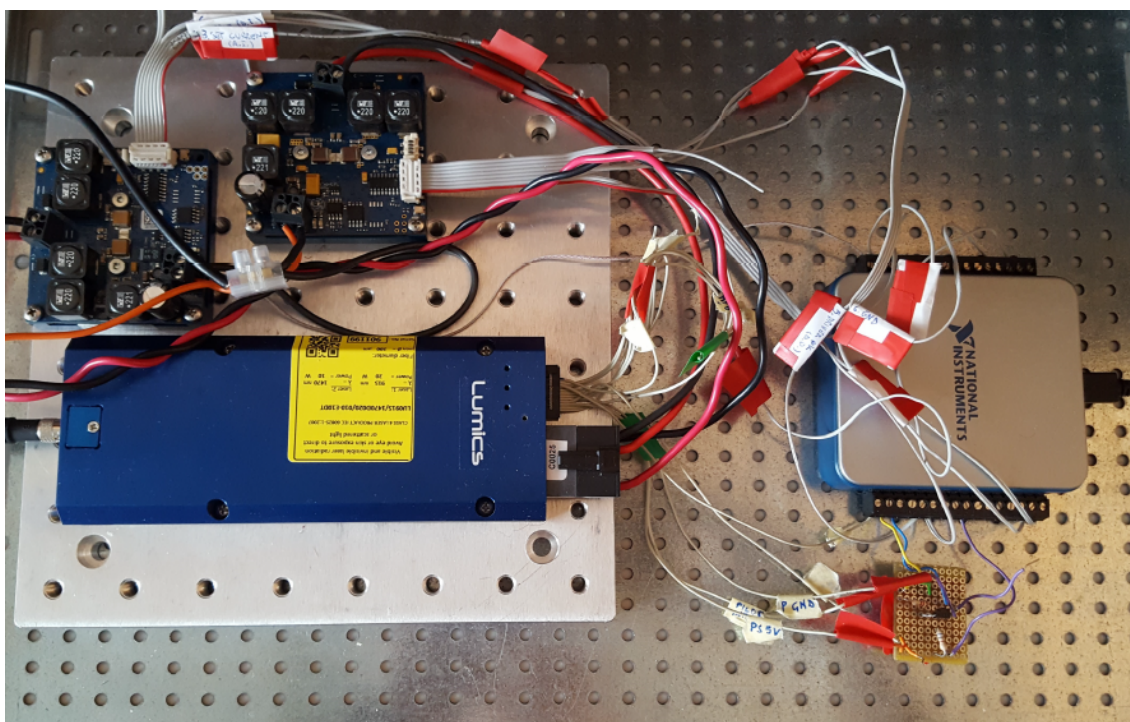


Figure 5.13: Illustration of laser device including Lumics laser diode [27]

mode has been used for the tests. Laser device's DAQ has been connected to a desktop computer via USB indeed, during the experiments, the laser has been triggered using a LABVIEW software interface on the computer, where it was asked to select the wavelength, laser mode, and the power to deliver.

A dual power supply has been used to the device; the delivery fibre produced by Thorlabs (core diameter 200 μm , cladding diameter 225 μm , numerical aperture 0.39) has been connected to the laser. The FBGs array was connected to Channel 1 of the Micron Optics to save data for the whole duration of the tests. Before the data saving, the laser has been checked with a PowerMeter to verify the correctness of the provided power values.

5.2.2 Results and Conclusions

Data acquired with the MicronOptics are post-processed with a Matlab® code in which the signals are filtered with a *moving average filter* and the Eq. 5.1 is used to derive temperature values from the Bragg wavelengths.

Temperature Deviation AIR				
FBG	Laser off	0.5W	1W	1.5W
1	0.28 °C	0.23 °C	0.35 °C	0.47 °C
2	0.29 °C	0.30 °C	0.55 °C	0.87 °C
3	0.28 °C	0.53 °C	1.05 °C	1.47 °C
4	0.29 °C	1.11 °C	1.83 °C	2.57 °C
5	0.33 °C	1.29 °C	2.29 °C	3.01 °C
6	0.27 °C	0.62 °C	1.26 °C	1.60 °C
7	0.31 °C	0.39 °C	0.76 °C	1.06 °C
8	0.27 °C	0.18 °C	0.39 °C	0.56 °C
9	0.30 °C	0.20 °C	0.29 °C	0.29 °C
10	0.25 °C	0.21 °C	0.22 °C	0.30 °C
11	0.34 °C	0.21 °C	0.21 °C	0.25 °C
12	0.33 °C	0.12 °C	0.26 °C	0.36 °C
13	0.25 °C	0.21 °C	0.13 °C	0.25 °C
14	0.25 °C	0.19 °C	0.15 °C	0.19 °C
15	0.20 °C	0.20 °C	0.17 °C	0.17 °C
16	0.18 °C	0.12 °C	0.14 °C	0.17 °C
17	0.22 °C	0.16 °C	0.14 °C	0.16 °C
18	0.16 °C	0.12 °C	0.10 °C	0.12 °C
19	0.16 °C	0.15 °C	0.11 °C	0.16 °C
20	0.26 °C	0.11 °C	0.20 °C	0.15 °C

Table 5.6: Maximum temperature deviation for the FBGs in air during self-heating evaluation.

The maximum temperature deviations reported in Tab. 5.6, 5.7 have been computed evaluating the difference between the maximum and the minimum temperature reached for each FBG during the tests. From the tables it can be noticed that the temperature deviations are smaller in air with a maximum of 0.34°C when the laser is off. This is probably due to a strain contribution that water could instead carry on the FBGs. In addition to that, it is clear from the tables which is the portion of FBGs array irradiated: for the test in air, the highest increase of temperature is on FBG 5, with a maximum of 3.01°C deviation with 1.5 W; for the test in water instead, FBG 2 is the irradiated one with a maximum of 2.94°C deviation with 1.5 W;

There isn't a big difference between the temperature deviation in air or in water when the laser is on but it is obvious that the stability in air is greater than in water when the laser is off.

Temperature Deviation WATER				
FBG	Laser off	0.5W	1W	1.5W
1	1.24 °C	1.19 °C	1.82 °C	2.50 °C
2	1.69 °C	1.42 °C	2.14 °C	2.94 °C
3	1.79 °C	1.30 °C	1.84 °C	2.46 °C
4	1.50 °C	1.27 °C	1.84 °C	2.59 °C
5	1.17 °C	1.10 °C	1.73 °C	2.51 °C
6	0.99 °C	0.96 °C	1.56 °C	2.04 °C
7	0.76 °C	0.92 °C	1.27 °C	1.95 °C
8	0.70 °C	0.78 °C	1.13 °C	1.73 °C
9	0.53 °C	0.67 °C	1.08 °C	1.54 °C
10	0.44 °C	0.66 °C	1.04 °C	1.54 °C
11	0.36 °C	0.58 °C	0.91 °C	1.38 °C
12	0.33 °C	0.54 °C	0.88 °C	1.25 °C
13	0.28 °C	0.49 °C	0.77 °C	1.11 °C
14	0.25 °C	0.45 °C	0.70 °C	1.03 °C
15	0.20 °C	0.32 °C	0.65 °C	0.94 °C
16	0.18 °C	0.25 °C	0.58 °C	0.80 °C
17	0.22 °C	0.24 °C	0.47 °C	0.54 °C
18	0.14 °C	0.26 °C	0.44 °C	0.32 °C
19	0.18 °C	0.21 °C	0.28 °C	0.34 °C
20	0.25 °C	0.18 °C	0.30 °C	0.28 °C

Table 5.7: Maximum temperature deviation for the FBGs in water during self-heating evaluation

5.3 Ex-vivo experiments on bovine liver

The measurement of the temperatures during the liver laser ablation is fundamental to trigger and adjust the procedure; the aim is to obtain a complete ablation of the tumor to avoid any recurrences and, at the same time, keep the heating controlled and reduce the destruction of non-cancerous tissues.

In this thesis some *ex-vivo* bovine liver ablation experiments have been performed with a laser device; the procedure and the results are described in this section. The results are affected from errors due to the measurement setup errors, the instruments uncertainty and to the simplifications and approximations introduced. Indeed, when the measure of the temperature is obtained for a single FBG, that value is actually mediated over the length of the grating (usually 1 mm), so it is not a temperature punctual value. Furthermore when the measurements are performed

really close to the delivery probe, there is a risk of sensor damage, resulting in measure errors. The experimental tests described in this chapter have been used to optimize the thermal model described in Chapter 4, taking into account the variability of the measures and the approximations of the model itself.

5.3.1 Set-up and Measurements

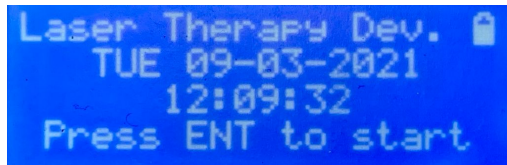
The laser device used for these experiments is the result of a previous project of thesis [31]. Its specifications are:

- Laser Diode 9W Power;
- 915 nm emission wavelength;
- Battery power supply;
- CW mode and PW mode availability;
- Emergency STOP button;

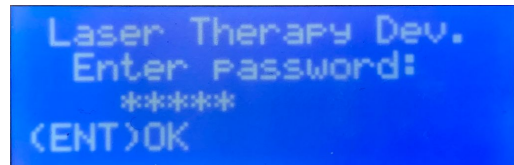


Figure 5.14: Illustration of laser device used for the experiments on the liver [31].

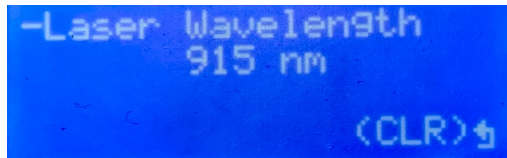
The device is supplied with a simple hardware interface where the screen is a helpful guide to set the device with the desired parameters (Fig. 5.15).



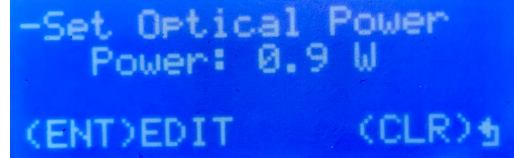
(a) Laser display when the device is switched on.



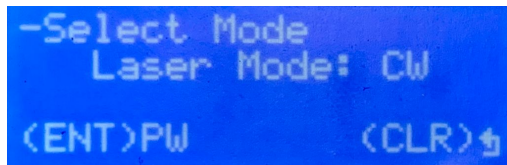
(b) Display showing a 5-digits password request.



(c) Display showing the laser wavelength set.



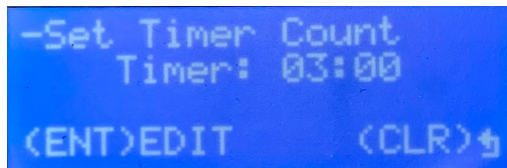
(d) Display showing the setting of the optical power.



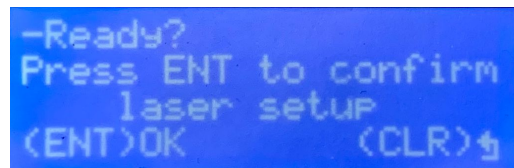
(e) Display showing the mode selection options.



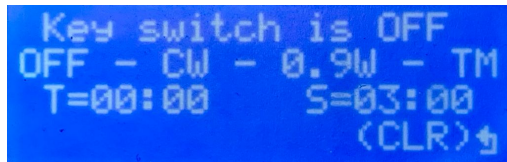
(f) Settings of frequency and duty-cycle in case of PW selection.



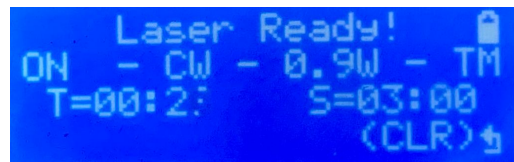
(g) Timer counter selection (mm:ss).



(h) Display at the end of the setting requests.



(i) Display asking for the security key switch on to activate.



(j) Final display before the activation of the laser using the laser button.

Figure 5.15: Illustration of the screen settings procedure steps to activate the laser used for the ex-vivo experiments on the bovine liver. The pictures in the figure are obtained from the device in Fig. 5.14.

When the device is switched on, a security password is required (Fig. 5.15b) to gain access to the parameters setting. The laser wavelength (Fig. 5.15c), optical

power (Fig. 5.15d) and operation mode (Fig. 5.15e) are then required and, in case of pulsed wave mode selection, also the frequency and duty-cycle (Fig. 5.15f) need to be inserted. Then a timer can be inserted (Fig. 5.15g) to stop the device automatically at the end of the set time and by switching the security key on, the laser is ready to emit the wave (Fig. 5.15j).

The laser diode is current-driven and for this reason a powermeter has been used to find the correspondence between the current and the power. For the experiments in this chapter four values of power have been used: 0.5 W, 1 W, 1.5 W, 2 W (Tab. 5.8).

CURRENT (A)	POWER (W)
0.9	0.5
1.2	1
1.9	1.5
2.6	2

Table 5.8: Correspondence between current and power for the laser diode used.

The delivery fibre with the 915 nm diode is a multimode fibre and its specifications are:

- Buffer diameter: 250 μm ;
- Cladding diameter: 125 μm ;
- Core diameter: 105 μm ;
- Numeric aperture (NA): 0.22;
- Fiber Length: 2 m.

Three sensing optical fibres have been used to detect the temperature:

- a HighDensity-19-FBGs-array;
- a HighDensity-20-FBGs-array (its characterization is reported in Paragraph 5.1);
- 1 Straight-20-FBGs-array (its characterization is reported in Paragraph 5.1).

Both are single-mode fibres with 9 μm *core* diameter and 125 μm *cladding* diameter.

The tests have been performed using:

1. MicronOptics HYPERION si155 interrogator (described in 5.1.1);
2. Laser device with delivery fibre;
3. Sensing fibres;
4. Precision caliper;
5. Two bovine liver slices.

The setup (Fig. 5.16) includes the Straight-20-FBGs-array positioned perpendicularly to the delivery probe, 2 mm apart from it (array 1), one HighDensity-20-FBGs-array positioned along the delivery probe (array 2) and the last HighDensity-20-FBGs-array positioned in parallel to the delivery fiber and 1 mm apart from it (array 3) (Fig. 5.16a). The fibres are placed on the bottom slice of liver (Fig. 5.16b, 5.16c) and they are covered with the upper slice for the whole duration of the experiments.

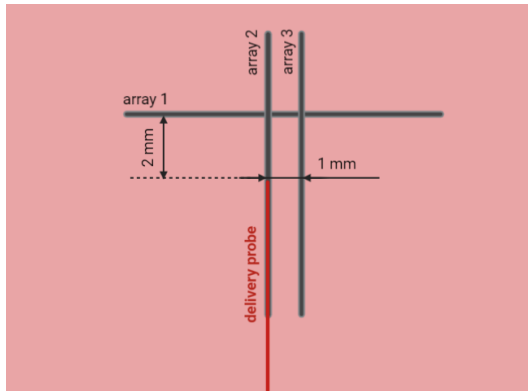
The array 1 has been connected to channel 1 of the Micron Optics, the array 2 to channel 2 and the array 3 to channel 3. The organization of the tests is shown in Table 5.9.

TEST	POWER (W)	DURATION (s)
1	0.5	180
2	1	180
3	1.5	180
4	2	180

Table 5.9: Organization of the ex-vivo liver ablation experiments performed.

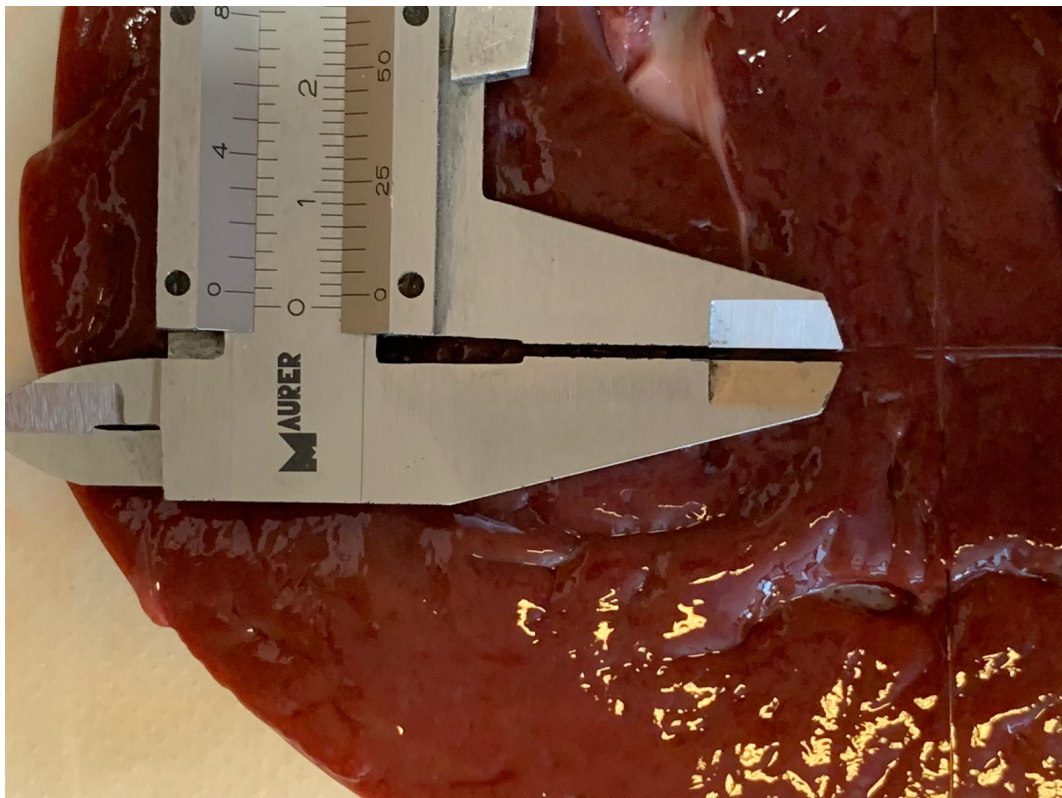
For each test the signal started to be acquired before the activation of the laser and it was stopped after the laser switching off. The liver in each test has been irradiated for 3 minutes; the Bragg peaks registered in the file created with the Micron Optics have been acquired with a 5 Hz frequency. After each test the fibres have been moved to another region of the liver slices before performing the new test. This is because the coagulation or even just the dehydration of the tissue resulting from one trial could affect the measures of the following trial.

The Matlab® code used to process the data acquired during the tests exploits the relationship between the Bragg wavelength and the temperatures expressed in Eq. 5.1. The signals have been filtered with a moving average filter, mediating on a number of samples that depends on the length of the signal itself.



(a) Graphical representation of the fibres positioning on the liver.

(b) Picture of the fibres positioning on the liver.



(c) Detail of the distance between array 2 and array 3 measured with a caliper.

Figure 5.16: Setup for the ex-vivo bovine liver experiments.

5.3.2 Results and Conclusions

In Fig. 5.17, 5.18, 5.19 the trend of the temperatures ($^{\circ}\text{C}$) of the FBGs is reported for each array by the time (s). It is possible to notice the moment in which the laser is activated and the moment when it is turned off. The total activation time of the device is 180 s.

The FBGs closer to the delivery probe register higher temperature values, while the FBGs further apart from the heat source have values closer to the ambient temperature. This is true for all the tests at different power and for all the arrays.

From Fig. 5.17 it can be observed that the array 1 reaches lower temperatures at 1.5 W than at 1 W; this can be due to an error in the positioning of the array 1 at 1.5 W, because also one millimeter of difference could lead to significant deviations in temperature measurements.

The number of FBGs to register high temperatures in array 1 is lower compared to the ones in array 2 and 3: this is because the ablated area is more extended in z-direction than in r-direction.

In general the array 2 is the one that measures the highest temperatures because it is positioned along the delivery probe and so it is closer to the emitted beam. In Tab. 5.10 the highest temperature reached during the tests are reported for each array. The results are coherent with the expected ones, except for the array 1 at 1.5 W, where a bad positioning of the array could have been occurred.

The tests data have also been analysed to define the trend of the temperatures as a function of the position both in r-direction and z-direction (depending on the considered array). The temperatures by the positions have been showed for different instants of time, to highlight the increasing of the values during the 3 minutes of ablation. In particular, the trend of temperatures is plotted during the ablation every 10 seconds, for a total of 18 trends in each graph (totally 180 seconds). The results are showed in Fig. 5.21, 5.22, 5.23. A symmetric increasing of temperatures can be observed around the 0 position for the arrays 1 and 3. For the array 2 instead, a zigzagged trend is shown and it could be due both to irregularities in the tissue leading to uncontrolled heat losses in some points and both to errors in the array fabrication.

Finally the effects of the ablation on the liver slices are showed. There are no visible effects on the liver for the test at 0.5 W, at the reached temperatures are not high enough to induce coagulation and necrosis of the tissue. It is possible to notice from Fig. 5.20 the signs on the liver are coherent with the values of power used: from 1 W to 1.5 W and 2 W the portion of liver burnt is always larger. For lower powers the ablated area is circular while for higher power values

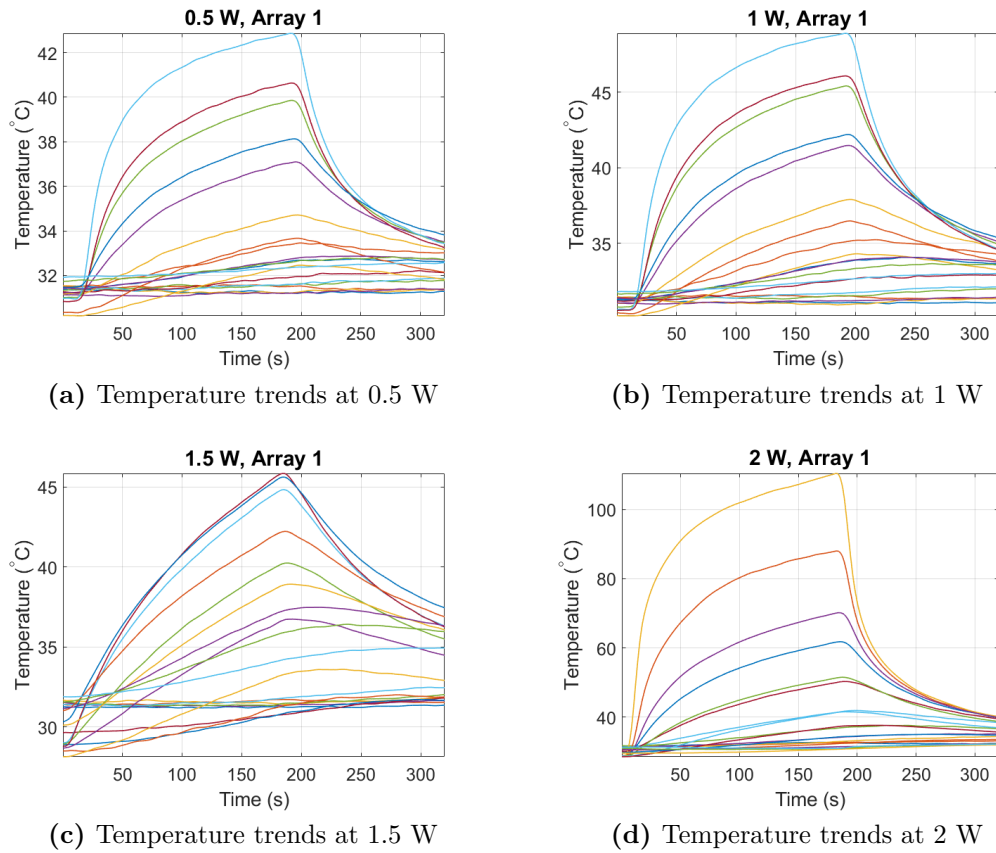


Figure 5.17: Temperatures reached during the experiments for the array 1.

it has an elongated shape. The temperatures are coherent with the values reported in literature and considered as cytotoxic for a biological tissue (Tab. 4.1). The measures are still affected by errors: when the upper slice of liver is positioned on the arrays, these could move, affecting the precision of their location. Also the increasing of temperature during the tests could cause the shift of the fibres, due to the dehydration of the tissue and its contraction. Finally, each FBG has an extended dimension (in this case 1 mm), so the value measured by the FBG is mediated over its extension and it is not a real punctual value.

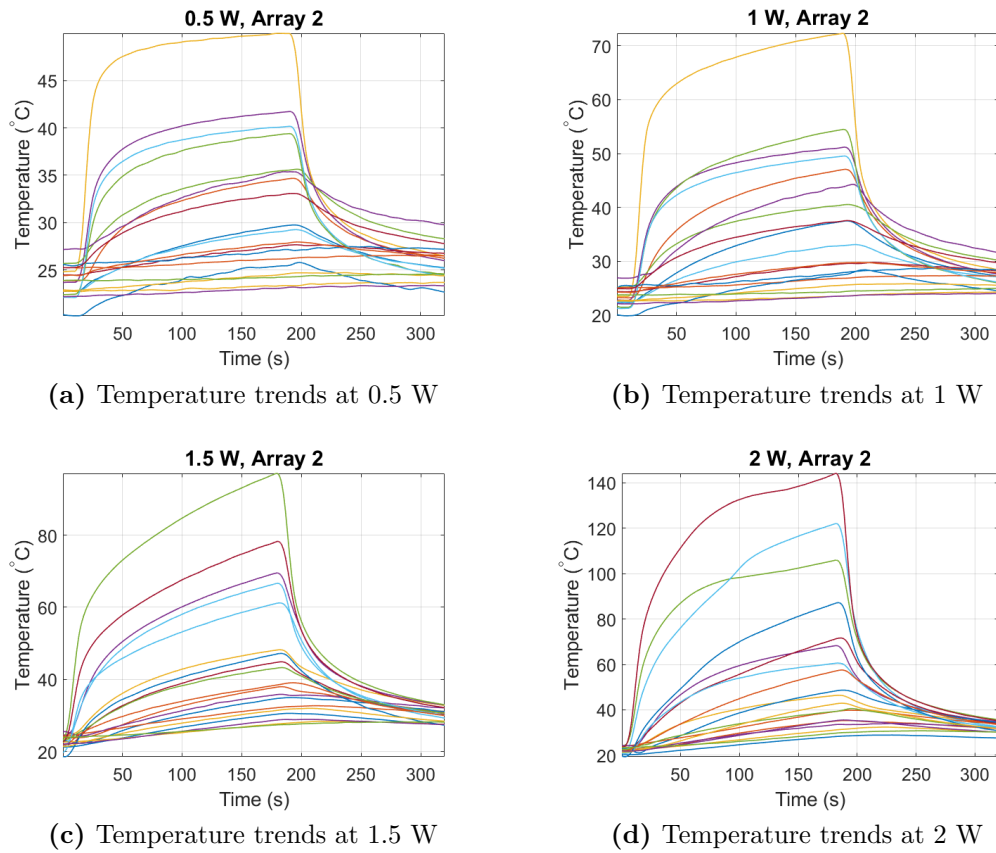
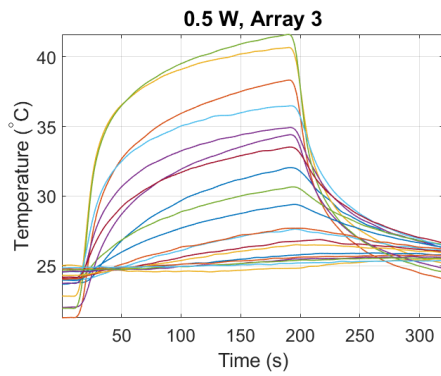


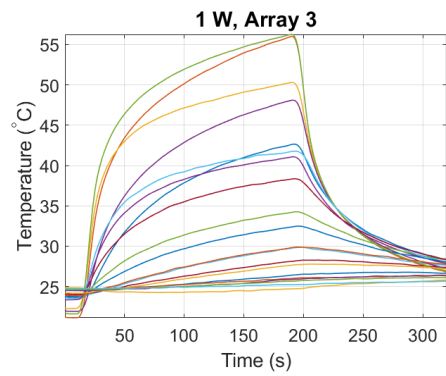
Figure 5.18: Temperatures reached during the experiments for the array 2.

Array	Maximum Temperature Measured			
	0.5 W	1 W	1.5 W	2 W
1	42.93 °C	49.01 °C	45.99 °C	111.02 °C
2	49.98 °C	72.31 °C	97.13 °C	144.13 °C
3	41.64 °C	56.46 °C	76.09 °C	92.98 °C

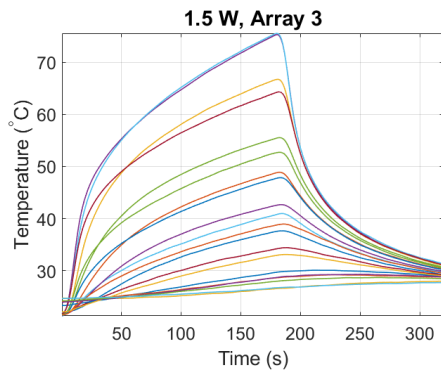
Table 5.10: Maximum temperature measured with the arrays during the tests at each power value.



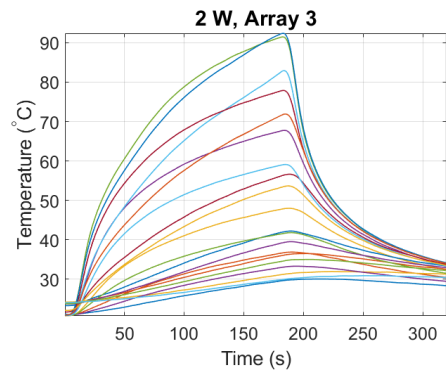
(a) Temperature trends at 0.5 W



(b) Temperature trends at 1 W



(c) Temperature trends at 1.5 W



(d) Temperature trends at 2 W

Figure 5.19: Temperatures reached during the experiments for the array 3.



(a) Effects on the liver after the irradiation at 1 W for 3 minutes.



(b) Effects on the liver after the irradiation at 1.5 W for 3 minutes.



(c) Effects on the liver after the irradiation at 2 W for 3 minutes.

Figure 5.20: Visible effects of the laser ablation on the bovine liver.

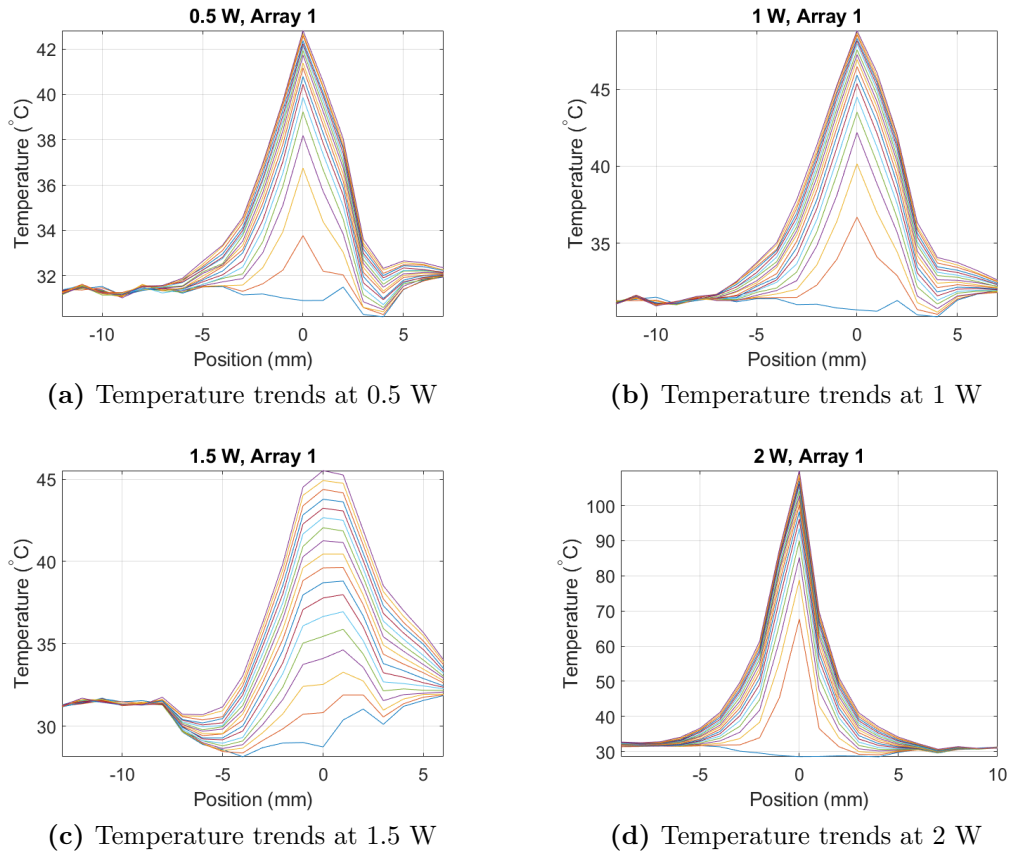
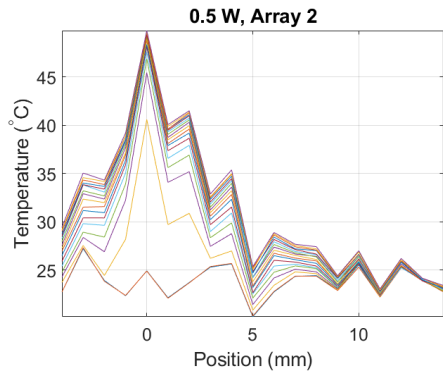
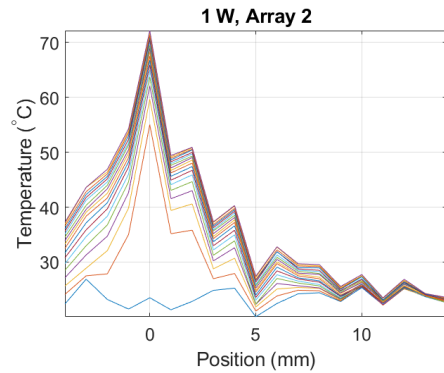


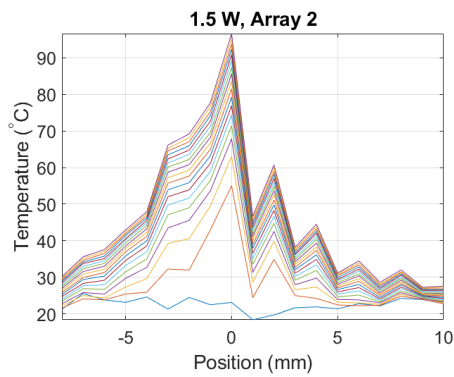
Figure 5.21: Graphics of the temperatures reached during the experiments in different instants of time by the positions of the FBGs. Array 1.



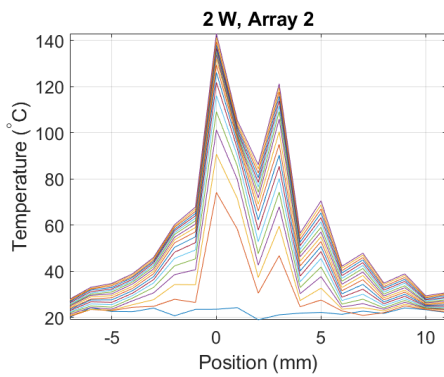
(a) Temperature trends at 0.5 W



(b) Temperature trends at 1 W



(c) Temperature trends at 1.5 W



(d) Temperature trends at 2 W

Figure 5.22: Graphics of the temperatures reached during the experiments in different instants of time by the positions of the FBGs. Array 2.

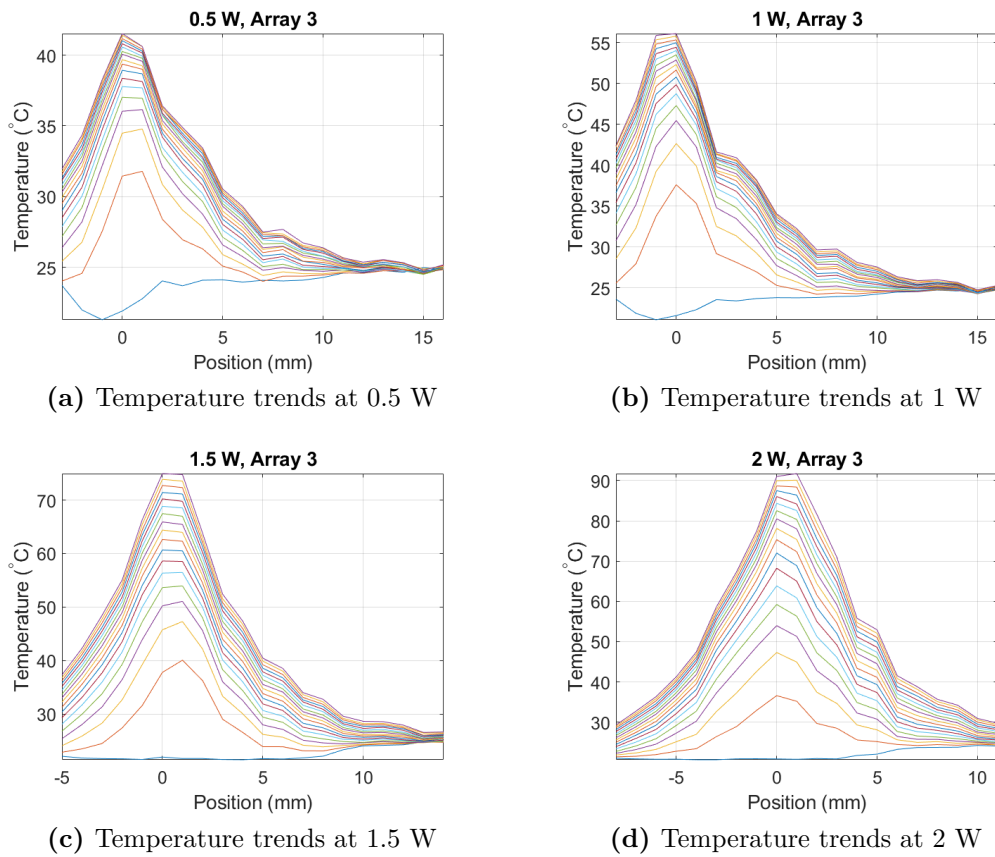


Figure 5.23: Graphics of the temperatures reached during the experiments in different instants of time by the positions of the FBGs. Array 3.

Chapter 6

Thermal Model Parameters Optimization

In this thesis, as described in Chapter 5, a thermal model has been developed, using parameters and equations found in literature to best approximate the behaviour of the liver during a laser ablation. The aim of the optimization is to find the values of such parameters that respond to the temperatures reached and measured experimentally. This could lead to the prediction of the temperatures in case of ablation on a liver “similar” to those used to optimize the model.

6.1 Methods and Implementation

The optimization of the model has been performed evaluating 10 points along the z-axis in the model. This choice is justified by the fact that the highest temperatures are distributed along the z-axis; in r-direction instead a drastic decrease in the measured temperatures occurs. For this reason, for the experimental data, only the array along the delivery probe was considered in the optimization.

A Matlab® code has been implemented to optimize the thermal model described in Chapter 4. First the measured temperatures from the experimental tests described in Chapter 5 have been isolated in 10 points; in particular, the FBG measuring the highest temperature in the array has been picked together with the 9 following FBGs, for a total of 10 FBGs. The code used to process the data of the tests is the same of the one used to evaluate the temperatures in Chapter 5: the acquired wavelengths have been filtered and converted into temperatures using the Eq. 5.1. Furthermore, a code similar to the one of the thermal model has been implemented, where the values of thermal conductivity, absorption coefficient and scattering coefficient are the unknowns of the problem and so the parameters to optimize. The

temperatures in the positions corresponding to the ones of the selected FBGs in the tests, have been extracted from the model; after that, it has been evaluated the module of the difference between the vector of the measured temperatures and the vector of the computed ones. Such difference is minimized with the `fminsearch` Matlab function, starting from an initial estimate of the parameters to search. The optimized values of thermal conductivity, absorption coefficient and scattering coefficient are finally returned.

6.2 Results and Conclusions

The resulting parameters from the minimization of the difference between measured and computed temperatures have been used in the code of the model (Appendix A.1) and the obtained temperatures are compared with the measured ones and showed in Fig. 6.1, 6.2, 6.3, 6.4. Such comparison in terms of temperature error is showed in Tab. 6.1, 6.2, 6.3, 6.4. The results are encouraging as the maximum temperature deviation among all the tests is 5.85 °C (at 1.5 W) and can be considered acceptable as they don't affect significantly the ablated area.

	FBG position (r,z), mm									
	(0,0)	(0,1)	(0,2)	(0,3)	(0,4)	(0,5)	(0,6)	(0,7)	(0,8)	(0,9)
$\Delta T(^{\circ}C)$	0.40	0.41	0.38	0.13	0.10	0.21	0.24	0.21	0.19	0.18

Table 6.1: Temperature deviations after the optimization at 0.5 W.

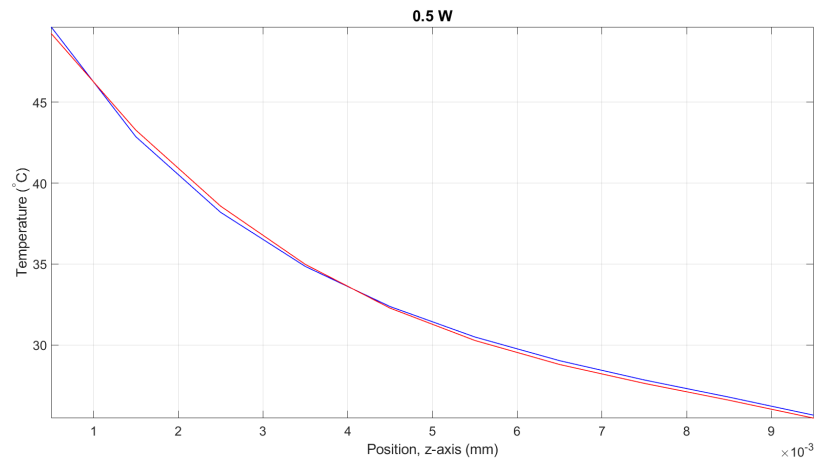


Figure 6.1: Graphical representation of the comparison between the measured temperatures and the temperatures evaluated with the optimized model. 0.5 W.

	FBG position (r,z), mm									
	(0,0)	(0,1)	(0,2)	(0,3)	(0,4)	(0,5)	(0,6)	(0,7)	(0,8)	(0,9)
$\Delta T(^{\circ}\text{C})$	1.29	1.06	1.02	1.65	0.27	1.07	2.17	2.66	2.10	0.22

Table 6.2: Temperature deviations after the optimization at 1 W.

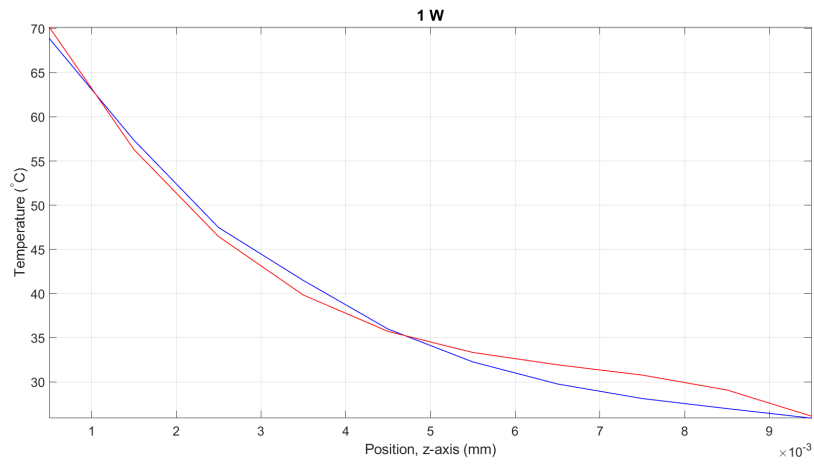


Figure 6.2: Graphical representation of the comparison between the measured temperatures and the temperatures evaluated with the optimized model. 1 W.

	FBG position (r,z), mm									
	(0,0)	(0,1)	(0,2)	(0,3)	(0,4)	(0,5)	(0,6)	(0,7)	(0,8)	(0,9)
$\Delta T(^{\circ}\text{C})$	1.89	1.80	2.16	2.87	0.60	2.02	4.46	5.85	5.11	1.24

Table 6.3: Temperature deviations after the optimization at 1.5 W. The optimization at 1.5 W is the one that corresponds to the highest temperature deviation: 5.85 °C.

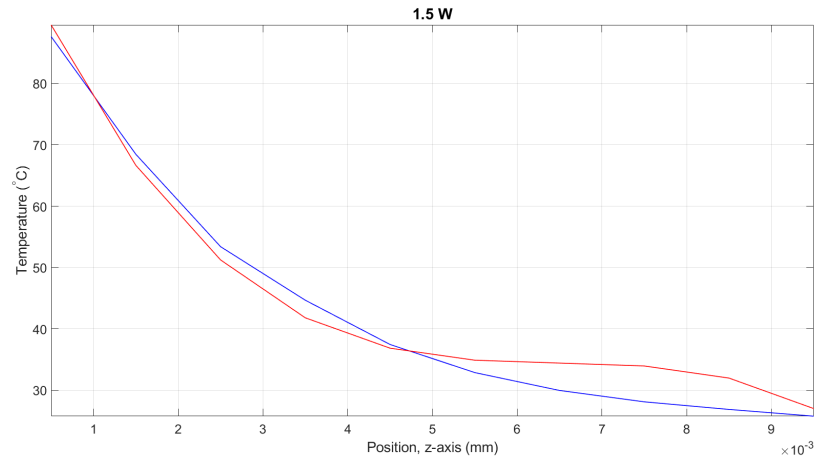


Figure 6.3: Graphical representation of the comparison between the measured temperatures and the temperatures evaluated with the optimized model. 1.5 W.

	FBG position (r,z), mm									
	(0,0)	(0,1)	(0,2)	(0,3)	(0,4)	(0,5)	(0,6)	(0,7)	(0,8)	(0,9)
$\Delta T(^{\circ}\text{C})$	0.26	0.73	1.69	1.78	0.22	0.65	0.14	0.84	1.27	3.01

Table 6.4: Temperature deviations after the optimization at 2 W.

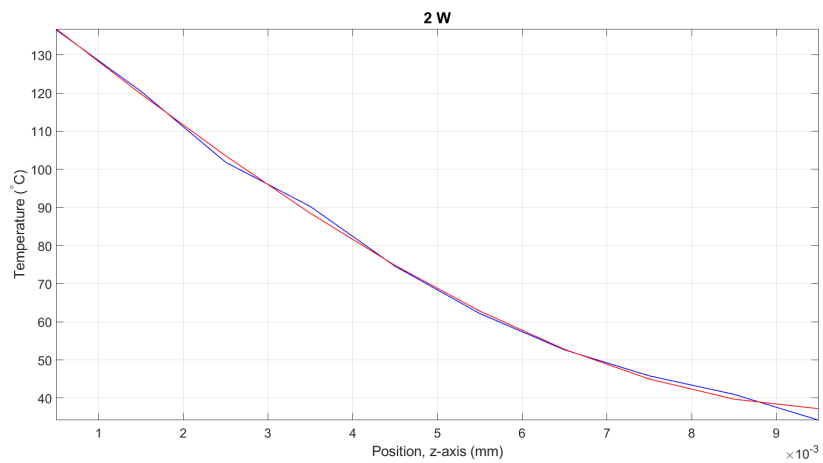


Figure 6.4: Graphical representation of the comparison between the measured temperatures and the temperatures evaluated with the optimized model. 2 W.

Obviously the parameters obtained (Tab. 6.5) do not correspond to the actual values of thermal conductivity, absorption coefficient and scattering coefficient, also because it is a simplification to consider them as constant values during the ablation: in reality the conductivity, absorption and scattering contributions are strongly dependent with the temperature; furthermore, the results cannot be considered universal because in the reality the parameters change also with the position analysed.

Despite all the approximations and assumptions made, this is still a method to predict, within an estimable error, the effects of the laser on the tissue.

	k ($\text{W m}^{-1} \text{K}^{-1}$)	μ_a (m^{-1})	μ_s (m^{-1})
0.5 W	0.200	23.375	7752.637
1 W	0.800	59.245	9122.201
1.5 W	0.799	59.140	12999.997
2 W	0.200	17.020	9868.310

Table 6.5: Values of the parameters optimized.

Chapter 7

Conclusions

This Master's thesis includes the study of laser ablation of the liver in the treatment of a tumour. This technique, similarly to other minimally-invasive treatments, exploits the direct heating of the biological tissue deriving from the absorption of an electromagnetic radiation and the indirect heating due to the heat conduction in the tissue. The advantages of laser ablation, such as its feasibility (small needles required), adaptability (up to four fibres simultaneously) and affordability (cheaper compared to other techniques) make this method an interesting subject for research. A laser (Light Amplification by Stimulated Emission of Radiation) is a coherent electromagnetic source generated from phenomena such as spontaneous emission, absorption and stimulated emission.

The emitted light interacts with the matter and undergoes attenuation and deviation because of two occurring phenomena: absorption and scattering. Depending on the absorption spectra of the irradiated matter, different effects will be experienced. An emitting source at 915 nm (infrared) has been used in this thesis to exploit the absorption spectra of the substances in the liver. The light, when absorbed, converts into thermal energy and the reaching of temperatures higher than 60 °C leads to the death of the cells. For an ex-vivo laser ablation, as described in this thesis, a general heat conduction problem can substitute the Pennes' BioHeat Transfer Equation, as the metabolic heat and the perfusion heat can be neglected. A laser diode has been used for the experimental part of this project, together with optical fiber emitting probes and optical fibres temperature sensors. Such fibres are "inscribed" with Fiber Grating Sensors, based on a shift in the reflected wavelength (Bragg wavelength) when a thermal or mechanical stress occurs. The FBGs have been characterized before their usage to find parameters of the relationship between Bragg wavelength and temperature. An optical interrogator (MicronOptics HYPERION si155) has been used to record sensor data during the tests. Experiments of ex-vivo laser ablation have been performed on bovine liver and the temperatures during the ablation have been post-processed to be

analysed. The measurements return acceptable values beside the errors due to the poor reproducibility of the tests: optical and thermal parameters indeed are strongly dependent on the different bovine liver and even on different areas of the same liver, because there could be points in which the heat is absorbed more than in other points for example.

A Matlab thermal model has been developed to simulate the ablation treatment experienced experimentally, a geometry representing the slice of liver has been created and the thermal and optical parameters of the laser source have been assigned to the model. Imposing boundary and initial conditions the solution of the temperature distribution is evaluated: the reached values are similar to the measured ones but the model needs to be optimized to minimize the error between the measured and evaluated temperatures. The optimization returns the parameters that better reproduce through the model, the measured temperatures. The temperature error has been evaluated along the axis on which the delivery probe is positioned during the ablation and the results are encouraging.

Obviously many future adjustments can be made both to the model and to the measurements organization. For example, parameters such as thermal conductivity, absorption coefficient and scattering coefficient can be inserted in the model not as constant values, but providing a dependence by the temperature, as it happens in reality. Furthermore, such parameters also change between a healthy and cancerous tissue, so a two-regions model could be implemented to distinguish between different areas of the liver. Finally, for the experiments, an emitting probe with inscribed FBGs could help to measure temperatures in fixed positions, avoiding the errors due to the positioning of the arrays.

Despite all the possible adjustments, the work of this thesis has led to temperature evaluations which do not differ significantly from the measured ones and for this reason the results can be considered satisfying.

Appendix A

Matlab codes

A.1 Thermal Model Code

```
1 %% RECTANGULAR BEAM MODEL
2 clearvars
3 clc
4 close all
5
6 %% Create a transient thermal model.
7 thermalmodelT = createpde('thermal','transient');
8
9 %% Include the geometry in the model.
10 r1 = [3 4 0 1e-2 1e-2 0 -0.5e-2 -0.5e-2 1e-2 1e-2];
11 gdm = [r1]';
12 %%geometry description matrix
13 ge = decsg(gdm,'R1',['R1']');
14 gm = geometryFromEdges(thermalmodelT,ge);
15
16 %% Show the model geometry
17 figure(1);
18 pdegplot(gm,'EdgeLabels','on','FaceLabels','on','VertexLabels','on')
19 axis equal
20 saveas(gcf,'geometry.png');
21
22 %% Assign thermal properties of the material to the model.
23 k = @(location,state) 0.57*location.x;
24 c = @(location,state) 3500*location.x;
25 rho = 1070;
26
27 thermalProperties(thermalmodelT,'ThermalConductivity',k,'MassDensity',
28     '...',
29     rho,'SpecificHeat',c);
```

```

29
30 %% Specify internal heat sources Q within the geometry.
31 p = 2; % Optical power (W).
32 r0=0.00005; % Fiber radius
33 u_a = 76; % Absorption coefficient (1/m)
34 u_s = 10015; % Scattering coefficient (1/m)
35 g = 0.9; % Degree of anisotropy of the scattering phase
    function (dimentionless)
36
37 sigma_0=r0;
38 u_eff=sqrt(3*u_a*(u_a+u_s*(1-g)));
39 n=1.33; % Refractive index
40 theta=asin(0.22/n);
41 sigma=@(location , state)(sigma_0+tan(theta).*location.y);
42
43 rect=@(location , state) ones(1,numel(location.x)).*(abs(location.x)<
    sigma(location , state));
44
45 q = @(location , state) u_a.*(p./((pi).*((sigma(location , state)).*(
    sigma(location , state))))).*rect(location , state).*exp(-u_eff.*((
    location.y)).*(location.x).*heaviside(location.y));
46
47 internalHeatSource(thermalmodelT , q);
48
49 %% Specify temperatures on the boundaries or heat fluxes through the
    boundaries
50 thermalBC(thermalmodelT , 'Edge' , [1 , 2 , 3] , 'Temperature' , 25);
51 thermalBC(thermalmodelT , 'Edge' , [4] , 'HeatFlux' , 0);
52
53 %% Set an initial temperature
54 T0 = 25;
55 thermalIC(thermalmodelT , T0);
56
57 %% Mesh the geometry to the model
58 msh=generateMesh(thermalmodelT , 'Hmax' , 0.00005);
59
60 %% Show the mesh
61 figure(2);
62 pdeplot(thermalmodelT);
63 axis equal
64 title 'Block With Finite Element Mesh Displayed'
65 saveas(gcf , "mesh.png");
66
67 %% Solve
68 tlist = 0:1:180;
69 R = solve(thermalmodelT , tlist);
70 T = R.Temperature;
71
72 %% Plot results

```

```

73 getClosestNode = @(p,x,y) min((p(1,:) - x).^2 + (p(2,:) - y).^2);
74 [~,nid1] = getClosestNode(msh.Nodes, 0, 0.0002);
75 [~,nid2] = getClosestNode(msh.Nodes, 0, 0.002);
76 [~,nid3] = getClosestNode(msh.Nodes, 0, 0.004);
77 [~,nid4] = getClosestNode(msh.Nodes, 0, 0.008);
78
79 h = figure;
80 h.Position = [1 1 2 1].*h.Position;
81
82 subplot(1,2,1);
83 pdeplot(thermalmodelT, 'XYData', T(:,end), 'Contour', 'on', 'ColorMap', '
    hot');
84 axis equal
85 axis equal
86 title 'Temperature, Final Time, Transient Solution'
87
88 subplot(1,2,2);
89 axis equal
90 plot(tlist(1:size(T,2)), T(nid1,:));
91 hold on
92 plot(tlist(1:size(T,2)), T(nid2,:));
93 hold on
94 plot(tlist(1:size(T,2)), T(nid3,:));
95 hold on
96 plot(tlist(1:size(T,2)), T(nid4,:));
97 grid on
98 title 'Temperature as a Function of Time';
99 xlabel 'Time, seconds'
100 ylabel 'Temperature, degrees-Celsius'
101
102 saveas(gcf, "results.png");

```

A.2 FBGs Characterization Code

```

1 clear all
2 close all
3 clc
4
5 %The ultradense array is connected to channel 1, the straight array
   to channel 2.
6
7 %% Loading of the .txt file from MicronOptics
8 %to open the peaks file including the path
9 [file_p, path_p] = uigetfile('*.txt', 'Load');
10 filename_p = sprintf('%s%s', path_p, file_p);

```

```

11 %reads the data from the peaks file into a table
12 t_p = readtable(filename_p , 'Delimiter', '\t');
13 time_p=t_p(:,1);
14 time_array_p= table2array(time_p);
15 time_array_p = datestr(time_array_p);
16 time_p = time_array_p(:,12:end);
17 datn_p = datenum(time_p, 'HH:MM:SS'); %convert time to string
18
19 channel = t_p(1:end-1,2:5); %number of peaks detected for
    channels
20 ch_array=table2array(channel);
21
22 peaks=t_p(1:end,6:end);
23 peaks=table2array(peaks);
24 peaks = strrep(peaks, ',', '.');
25 peaks_array = str2double(peaks(:, :));
26
27 row=length(ch_array);
28 col_1 = max(ch_array(:,1)); %maximum number of detected peaks for
    channel 1
29 col_2 = max(ch_array(:,2)); %maximum number of detected peaks for
    channel 2
30
31 %CHANNEL 1
32 channel1 = peaks_array(:,1:20);
33 %CHANNEL 2
34 channel2 = peaks_array(:,21:40);
35
36 %% Plotting the signals before filtering to see the proper number of
    samples to use for averaging.
37
38 j =0;
39 if col_1~=0
40     for i=1:col_1
41         j=j+1;
42         figure (j)
43         plot(channel1(:,j), 'c', 'LineWidth',2);
44         hold on
45         grid on
46         ax = gca; % c u r r e n t a x e s
47         ax.FontSize = 15;
48         xlabel ('Samples')
49         ylabel ('Wavelength (nm)')
50         title ( [ 'Channel 1 // Pre-filtered Wavelength, pair of FBGs
    number ' num2str(j) ] , 'fontsize',18)
51     end
52 end
53
54

```

```

55 j =0;
56 if col_2~=0
57     for i=1:col_2
58         j=j+1;
59         figure (j)
60         plot(channel2(:,j),'c','LineWidth',2);
61         hold on
62         grid on
63         ax = gca; % c u r r e n t a x e s
64         ax.FontSize = 15;
65         xlabel ('Samples')
66         ylabel ('Wavelength (nm)')
67         title ( [ 'Channel 2 // Pre-filtered Wavelength, pair of FBGs
number ' num2str(j) ] , 'fontsize',18)
68     end
69 end
70
71 %% Filtering
72 nt = 100; %the number of samples have to be the same for the
MicronOptics' file and for the therocouple. It is the maximum
number of samples that keeps the trend.
73
74 %filter coefficient
75 a = 1;
76 b = ones(1,nt)/nt;
77 peaks_array_f = filtfilt(b,a,peaks_array);
78 peaks_array_Nf = peaks_array (50:end-50,:);
79 datn_p2 = datn_p(50:end-50,:); %new temporal axis that match the
filtered signal
80
81
82 % Plot of filtered and un-filtered signal overlapped.
83 j=0;
84 for i=1:col_1
85     j=j+1;
86     figure (j)
87     plot(peaks_array_Nf(:,i),'c','LineWidth',1);
88     hold on
89     plot(peaks_array_f(:,i),'m','LineWidth',2);
90     grid on
91     ax = gca; % c u r r e n t a x e s
92     ax.FontSize = 15;
93     legend('Unfiltered', 'Filtered')
94     xlabel ('Samples')
95     ylabel ('Wavelength (nm)')
96     title ( [ 'Channel 1 // Effect of filtering, FBG num ' , num2str(
j) ] , 'fontsize',18)
97     hold off
98 end

```

```

99
100 j=0;
101 for i=1:col_2
102     j=j+1;
103     figure (j)
104     plot(peaks_array_Nf(:,i+20),'c','LineWidth',1);
105     hold on
106     plot(peaks_array_f(:,i+20),'m','LineWidth',2);
107     grid on
108     ax = gca; % current axes
109     ax.FontSize = 15;
110     legend('Unfiltered','Filtered')
111     xlabel('Samples')
112     ylabel('Wavelength (nm)')
113     title(['Channel 2 // Effect of filtering, FBG num ', num2str(
114         j) ], 'fontsize',18)
114     hold off
115 end
116 %% THERMOCOUPLE FILE
117
118 [file_t,path_t] = uigetfile('*.log','Load');
119 filename_t = sprintf('%s%s',path_t,file_t);
120 t_t = readtable(filename_t,'FileType','text');
121 time_t = t_t(8:end,1);
122 time_array_t = table2array(time_t);
123 time_array_t = datestr(time_array_t);
124 time_array_t = time_array_t(:,12:end);
125 datn_t = datenum(time_array_t,'HH:MM:SS');
126
127 temperature = t_t(8:end,2);
128 temperature = table2array(temperature);
129 temperature = str2double(temperature);
130
131 %% Filtering thermocouple file using the same parameters used for the
132     peaks.
133
133 temperature_f = filter(b,a,temperature);
134 temperature_f = temperature_f(50:end-50,:);
135 datn_t2 = datn_t(50:end-50,:);
136
137 %% Creation of a common temporal axis for thermocouple and peaks.
138 % The aim is to associate each measure of the thermocouple to the
139 % peak detected at the same instant of time.
140
141 l_max = max(length(datn_p2),length(datn_t2));
142 col = (size(peaks_array_f,2)+2);
143 data = zeros(l_max, col);
144 k = 1;
145 t=datn_t2';

```

```

146 % The matrix data has in the first column time (expressed as an array
    ), in the second the temperature at that time and the remaining
    columns are occupied by the corresponding peaks detected.
147
148 for i = t
149     if ismember(i, datn_p2')
150         loc_t = find(datan_t2==i);
151         data(k,1) = i;
152         data(k,2) = temperature_f(loc_t);
153         loc_p = find(datan_p2==i);
154         data(k,3:end) = peaks_array_f(loc_p, :);
155         k = k + 1;
156     end
157 end
158
159 %% Isolating the descending temperature trend.
160 i = 1;
161 while data(i,2) ~= max(data(:,2))
162     data(i,:) = [];
163 end
164
165 i = 1;
166 while data(i,2) > 80.0
167     data(i,:) = [];
168 end
169
170 i = length(data);
171 while data(i,2) < 27.0
172     data(i,:) = [];
173     i = length(data);
174 end
175
176 %% Coefficients are found interpolating the data.
177 % k (the slope of the straight line) is in the first column, lambda_0
    (intercept)
178
179 matr_coeff = zeros(size(data,2)-2,2);
180
181 for i = 3:size(data,2)
182     matr_coeff(i-2,:) = polyfit(data(:,2), data(:,i), 1);
183 end
184
185 matr_HD = matr_coeff(1:20,:);
186 matr_straight = matr_coeff(21:end,:);
187
188 figure()
189 plot(data(:,1), data(:,2), 'LineWidth', 1);
190 hold on
191 datetick('x', 'HH:MM:SS', 'kepticks');

```

```

192 grid on
193 ax = gca; % c u r r e n t axes
194 ax.FontSize = 12;
195 xlabel ( 'Absolute time')
196 ylabel ( 'Temperature  $^{\circ}$ C')
197 title ( [ 'Termocouple' ] , 'fontsize',18)
198
199
200 %% Evaluation of temperature with the coefficients
201 %the inverse formula of Bragg Wavelength is used.
202
203 col = size(peaks_array_f,2);
204
205 Temp = zeros(size(data,1),size(peaks_array_f),col);
206
207 for j = 1:col
208     Temp(:,j) = (data(:,j+2) - matr_coeff_filter(j,2))/
209         matr_coeff_filter(j,1);
210
211 end
212
213 k=1;
214 for i = 1:20:80
215     figure(k);
216     plot(data(:,1), Temp(:,i:i+19), 'LineWidth',1);
217     hold on
218     datetick( 'x' , 'HH:MM:SS' , 'keepticks');
219     grid on
220     ax = gca; % c u r r e n t axes
221     ax.FontSize = 12;
222     xlabel ( 'Absolute time')
223     ylabel ( 'Temperature ( $^{\circ}$ C)')
224     k = k+1;
225 end
226
227 %% Evaluation of the quality of fitting
228
229 row = size(data,1);
230 col = size(peaks_array_f,2);
231
232 lambda_s = zeros(row, col); %experimental lambdas
233 lambda_m = data(:,3:end);
234 temperature_m = data(:,2); %measured temperature
235
236 for i = 1:col
237     lambda_s_straight(:,i) = matr_coeff(i,2) + matr_coeff(i,1)*
238         temperature_m;
239 end
240
241 %%Absolute error in the evaluation of temperature:

```

```

239
240 delta_t = zeros(row,col_1);
241 for i = 1:col_1
242     delta_t(:,i) = (lambda_m(:,i)-lambda_s(:,i))./matr_coeff(i,1);
243 end
244
245
246 temperature_s = zeros(row,col); %temperature "sensed" by the FBGs
247
248 for i=1:col
249     temperature_s(:,i) = (lambda_m(:,i) - matr_coeff(i,2))./
250     matr_coeff(i,1);
251 end
252 % Relative error:
253
254 error = zeros(row,col_);
255 for i = 1:col
256     error(:,i) = (temperature_m - temperature_straight(:,i))./
257     temperature_m;
258 end
259 %% Plotting temperature sensed by thermocouple and the one evaluated
260     using FBGs.
261 figure ()
262 plot(data(:,1),temperature_m,'LineWidth',2);
263 hold on
264 plot(data(:,1),temperature_s(:,1:col_1),'LineWidth',2); %HD
265 grid on
266 datetick('x','HH:MM:SS','kepticks');
267 ax = gca; %current axes
268 ax.FontSize = 15;
269 ylim([30 80])
270 xlabel('Time (s)')
271 ylabel('Wavelength (nm)')
272 title(['Comparison'], 'fontsize',18)
273 hold off
274
275 figure ()
276 plot(data(:,1),temperature_m,'b','LineWidth',2);
277 hold on
278 plot(data(:,1),temperature_s(:,col_1+1:end),'r','LineWidth',2);
279 grid on
280 ylim([30 80])
281 datetick('x','HH:MM:SS','kepticks');
282 ax = gca; %current axes
283 ax.FontSize = 15;
284 legend('Thermocouple','Evaluated')

```

```
285 xlabel ( 'Time (s)')
286 ylabel ( 'Wavelength (nm)')
287 title ( [ 'Comparison' ] , 'fontsize',18)
288 hold off
```

Bibliography

- [1] URL: <https://ourworldindata.org/cancer> (cit. on pp. 1, 2).
- [2] Siegel RL. «Cancer Statistics, 2021». In: *CA: a cancer journal for clinicians* (2021). URL: <https://pubmed.ncbi.nlm.nih.gov/33433946/> (cit. on p. 1).
- [3] A.Scott Pearson, Francesco Izzo, R.Y.Declan Fleming, Lee M Ellis, Paolo Delrio, Mark S Roh, Jennifer Granchi, and Steven A Curley. «Intraoperative radiofrequency ablation or cryoablation for hepatic malignancies». In: *The American Journal of Surgery* 178.6 (1999), pp. 592–598. ISSN: 0002-9610. DOI: [https://doi.org/10.1016/S0002-9610\(99\)00234-2](https://doi.org/10.1016/S0002-9610(99)00234-2). URL: <https://www.sciencedirect.com/science/article/pii/S0002961099002342> (cit. on pp. 2, 5).
- [4] E Goodarzi, F Ghorat, A Mosavi Jarrahi, HA Adineh, M Sohrabivafa, and Z Khazaei. «Global incidence and mortality of liver cancers and its relationship with the human development index (HDI): an ecology study in 2018». In: *World Cancer Research Journal* 6 (2019), p. 12 (cit. on p. 3).
- [5] Hayden W. Head and Gerald D. Dodd. «Thermal ablation for hepatocellular carcinoma». In: *Gastroenterology* 127.5, Supplement 1 (2004), S167–S178. ISSN: 0016-5085. DOI: <https://doi.org/10.1053/j.gastro.2004.09.031>. URL: <https://www.sciencedirect.com/science/article/pii/S0016508504016105> (cit. on pp. 4, 5, 7).
- [6] C. Brace. «Thermal Tumor Ablation in Clinical Use». In: *IEEE Pulse* 2.5 (2011), pp. 28–38. DOI: 10.1109/MPUL.2011.942603 (cit. on pp. 4–6).
- [7] Josep M. Llovet and Jordi Bruix. «Systematic review of randomized trials for unresectable hepatocellular carcinoma: Chemoembolization improves survival». In: *Hepatology* 37.2 (), pp. 429–442. DOI: <https://doi.org/10.1053/jhep.2003.50047>. eprint: <https://aasldpubs.onlinelibrary.wiley.com/doi/pdf/10.1053/jhep.2003.50047>. URL: <https://aasldpubs.onlinelibrary.wiley.com/doi/abs/10.1053/jhep.2003.50047> (cit. on p. 4).

- [8] J. Louis Hinshaw and Fred T. Lee. «Cryoablation for Liver Cancer». In: *Techniques in Vascular and Interventional Radiology* 10.1 (2007). Interventional Oncology - Part 1: Hepatic Interventions, pp. 47–57. ISSN: 1089-2516. DOI: <https://doi.org/10.1053/j.tvir.2007.08.005>. URL: <https://www.sciencedirect.com/science/article/pii/S108925160700073X> (cit. on pp. 4, 5).
- [9] S.Nahum Goldberg. «Radiofrequency tumor ablation: principles and techniques». In: *European Journal of Ultrasound* 13.2 (2001), pp. 129–147. ISSN: 0929-8266. DOI: [https://doi.org/10.1016/S0929-8266\(01\)00126-4](https://doi.org/10.1016/S0929-8266(01)00126-4). URL: <https://www.sciencedirect.com/science/article/pii/S0929826601001264> (cit. on pp. 5, 6).
- [10] «Microwave tumors ablation: Principles, clinical applications and review of preliminary experiences». In: *International Journal of Surgery* 6 (2008), S65–S69. ISSN: 1743-9191. DOI: <https://doi.org/10.1016/j.ijso.2008.12.028>. URL: <https://www.sciencedirect.com/science/article/pii/S1743919108002033> (cit. on pp. 5, 7).
- [11] Sergio Sartori, Francesca Di Vece, Francesca Ermili, and Paola Tombesi. «Laser ablation of liver tumors: An ancillary technique, or an alternative to radiofrequency and microwave?» In: *World journal of radiology* 9.3 (2017), p. 91 (cit. on pp. 5, 7).
- [12] Paola Tombesi, Francesca Di Vece, and Sergio Sartori. «Radiofrequency, microwave, and laser ablation of liver tumors: time to move toward a tailored ablation technique?» In: *Hepatoma Research* 1 (2015), pp. 52–57 (cit. on pp. 5, 8).
- [13] URL: <https://www.electronicshub.org/laser-diode-working-structure-types-uses/> (cit. on p. 11).
- [14] URL: <https://www.electrical4u.com/laser-diode/> (cit. on p. 11).
- [15] URL: https://www.snewsonline.com/notizie/tecnologie_e_servizi/fibra_optica_la_rivoluzione_della_luce-6277 (cit. on p. 12).
- [16] URL: <https://www.blackbox.it/it-it/page/28537/Informazioni/Risorse-Tecnologiche/Spiegazioni-Black-Box/fibre-optic-cable/Confronto-tra-cavo-in-fibra-ottica-multimodale-e-monomodale> (cit. on p. 14).
- [17] D. Lo Presti et al. «Fiber Bragg Gratings for Medical Applications and Future Challenges: A Review». In: *IEEE Access* 8 (2020), pp. 156863–156888. DOI: 10.1109/ACCESS.2020.3019138 (cit. on pp. 14, 17).
- [18] URL: <https://hittech.com/de/portfolio-posts/noria-the-fiber-bragg-grating-manufacturing-solution/> (cit. on p. 15).

- [19] URL: <https://fbgs.com/solutions/temperature-sensing/> (cit. on p. 18).
- [20] Aurora Bellone. *Optical fibre sensors for distributed temperature monitoring during mini-invasive tumour treatments with laser ablation*. Master's degree thesis. 2020 (cit. on p. 19).
- [21] URL: <https://lunainc.com/product/si155-optical-sensing-instrument> (cit. on p. 20).
- [22] Alessandra Beccaria. *Studio teorico e sperimentale del comportamento termo-ottico di tessuti biologici per il trattamento di tumori mediante ablazione laser*. Master's degree thesis. 2019 (cit. on pp. 21, 30).
- [23] Lorenzo Torrisi et al. «Applicazioni di fasci laser al settore biomedico». In: July 2011 (cit. on p. 20).
- [24] Piero Campolmi, Paolo Bonan, Giovanni Cannarozzo, Andrea Bassi, Nicola Bruscano, Meena Arunachalam, Michela Troiano, Torello Lotti, and Silvia Moretti. «Highlights of thirty-year experience of CO₂ laser use at the Florence (Italy) department of dermatology». In: *The Scientific World Journal* 2012 (2012) (cit. on p. 23).
- [25] Sourav Bhattacharjee. «DLS and zeta potential – What they are and what they are not?» In: *Journal of Controlled Release* 235 (2016), pp. 337–351. ISSN: 0168-3659. DOI: <https://doi.org/10.1016/j.jconrel.2016.06.017>. URL: <https://www.sciencedirect.com/science/article/pii/S0168365916303832> (cit. on p. 24).
- [26] URL: <https://omlc.org/classroom/ece532/class3/gdefinition.html> (cit. on p. 25).
- [27] Edoardo Puleo. *Sviluppo di un sistema per Ablazione Laser in ambiente oncologico*. Master's degree thesis. 2020 (cit. on pp. 26, 52, 53).
- [28] Jan Taler and Paweł Ocioń. «Finite Element Method in Steady-State and Transient Heat Conduction». In: Dec. 2013, pp. 1604–1633. ISBN: 978-94-007-2738-0. DOI: [10.1007/978-94-007-2739-7_897](https://doi.org/10.1007/978-94-007-2739-7_897) (cit. on pp. 27, 28).
- [29] P. Saccomandi, E. Schena, M. A. Caponero, F. M. Di Matteo, M. Martino, M. Pandolfi, and S. Silvestri. «Theoretical Analysis and Experimental Evaluation of Laser-Induced Interstitial Thermotherapy in Ex Vivo Porcine Pancreas». In: *IEEE Transactions on Biomedical Engineering* 59.10 (2012), pp. 2958–2964. DOI: [10.1109/TBME.2012.2210895](https://doi.org/10.1109/TBME.2012.2210895) (cit. on p. 32).

- [30] Mohit Ganguly, Ryan O’Flaherty, Amir Sajjadi, and Kunal Mitra. «Chapter 2 - Tissue Response to Short Pulse Laser Irradiation». In: *Heat Transfer and Fluid Flow in Biological Processes*. Ed. by Sid M. Becker and Andrey V. Kuznetsov. Boston: Academic Press, 2015, pp. 43–58. ISBN: 978-0-12-408077-5. DOI: <https://doi.org/10.1016/B978-0-12-408077-5.00002-X>. URL: <https://www.sciencedirect.com/science/article/pii/B978012408077500002X> (cit. on p. 32).
- [31] Giuseppe Poma. *Laser medicali per ablazione di tumori*. Master’s degree thesis. 2020 (cit. on p. 56).